공학박사학위논문

Effect of surface modification on the structure and electrochemical properties of electrocatalysts for polymer electrolyte membrane fuel cells

연료전지용 촉매의 구조 및 전기화학적 특성에 대한 표면개질의 영향

2013년 2월

서울대학교 대학원

화학생물공학부

박 희 영

Effect of surface modification on the structure and electrochemical properties of electrocatalysts for polymer electrolyte membrane fuel cells

연료전지용 촉매의 구조 및 전기화학적 특성에 대한 표면개질의 영향

지도교수 성 영 은

이 논문을 공학박사학위논문으로 제출함

2010년 12월

서울대학교 대학원
화학생물공학부
박 희 영

박희영의 박사학위논문을 인준함

2010년 12월

위 원 장 _____ (인)

부 위 원 장 _____ (인)

위 원 _____ (인)

위 원 _____ (인)

위 원 _____ (인)

Abstract

Due to strong dependence of electrocatalytic reactions on the surface structure of the catalysts, surface-modified nanoparticles have been studied widely to achieve highly efficient and economical electrocatalysts. There have been various strategies to achieve the surface-modified nanoparticles.

The effect of surface-modification on the hydrogen oxidation reaction (HOR) and oxygen reduction reaction (ORR) activity was investigated using carbon supported nanoparticle catalysts which were subjected to various surface modification methods and discussed based on the effect of heterogeneous atoms in the catalyst surfaces. The surface modifications were conducted three different ways: 1) deposition of Pt-sub-monolayer-shell on Pd-core nanoparticles, 2) thermal treatment of Pt-Au alloy nanoparticles under CO or Ar gas which led to different surface Pt-Au compositions but identical bulk compositions, and 3) selective adsorption of phosphoric acid on Se in $RuSe_y$/C catalyst.

Tht HOR activity of Pd nanoparticles modified by sub-monolayer of Pt was investigated at a Pt surface concentration of 0 ~ 5.7 %. The combination of electrochemical measurements and high resolution-X-ray photoelectron spectroscopy revealed a significant decrease in oxidized Pd atoms (23.4 %) with a Pt surface concentration of 1.7% compared with that of Pd/C. X-ray absorption

spectroscopy of the Pt $_{LIII}$ suggested preferred Pt deposition, which led to more oxidized Pt atoms during Pt shell growth. The exchange current density of the hydrogen oxidation reaction on the electrocatalyst with a Pt surface concentration of 4.9 % was 3.5 times higher than that on Pd/C and was comparable with that on Pt surfaces. The changes in hydrogen oxidation reaction apparent enthalpy due to Pt shell growth suggested a rate determining step (RDS) change (Volmer reaction → Tafel reaction) at a Pt surface concentration of 1.7 %.

In order to investigate the effect of CO induced surface segregation on the ORR activity of PtAu nanoparticles, the catalysts were subject to heat treatment at 423 K under a CO or Ar atmosphere. The surface composition was analyzed by XPS and the composition was shown to increase from 66 ± 2 % (PtAu-AP) to 74 ± 2 % (PtAu-CO) after heat treatment under a CO atmosphere, which was confirmed by electrochemical techniques, while the bulk composition was invariant at 55 %. For the oxygen reduction reaction (ORR), the mass activity of PtAu-CO increased by 75.6 % (33.2 A/g_{Pt}) when compared to that of PtAu-AP (18.9 A/g_{Pt}). Since the increase in EAS was only 15.8 %, it was concluded that the specific activity was enhanced by 52.6 % due to surface Pt segregation after heat treatment under a CO atmosphere. The enhanced specific activity was attributed to the reduced OH adsorption energy which was characterized by measuring the potential of total zero

charge. The weaker OH adsorption was resulted from the higher Pt/Au ratio at the surface layers.

The effect of phosphate adsorption on the ORR activity of Se-modified-Ru catalysts ($RuSe_y/C$) was examined. The ORR activity of unmodified Ru/C catalyst decreased by 26.8% as the active site was blocked by electrochemical adsorption of phosphoric acid. However, for $RuSe_y/C$, the ORR activity was enhanced with phosphoric acid ($RuSe_{1.56}/C$: 63.8%), which indicates that the kinetics at each site increased to compensate for the site blocking effect. The XAS results demonstrated that, for $RuSe_y/C$, phosphoric acid molecules or phosphate anions primarily interacted with Se atoms, and the oxidation state of Ru atoms decreased. Therefore, it was concluded that the enhanced ORR kinetics originated from the decreased oxygen binding energy with larger electrostatic repulsion.

Keywords: Polymer electrolyte membrane fuel cells, electrocatalyst, surface modification, hydrogen oxidation reaction, oxygen reduction reaction

Student number: 2008-30260

Contents

List of Figures

List of tables

Chapter I

Introduction

1.1 Energy and environment

Global warming has been one of the most critical issues in last few decades. CO_2 emissions form the combustion of fossil fuels is blamed for causing the greenhouse effect to increase. Emissions of CO_2 from the combustion of fossil fuels increased at an average yearly rate of 1.3% from 1990 to 2007. According to the Kyoto protocol, the members of the United Nations Framework Convention on Climate Change (UNFCCC) should reduce the emission of greenhouse gases by 5.2% compared to that in 1990.

According to International Energy Agency, 86% of the current global energy production comes from the combustion of fossil fuels. With the ever increasing world population, it is uncertain how long our available fossil fuel reserves will be able to meet our energy demand. Moreover, the environmental impact of fossil fuel combustion underlines the necessity of finding clean energy sources that will allow us to live and prosper without destroying the global climate.

Renewable energies, such as solar, wind, and geothermal energy have been suggested zero emission energy sources which does not generate greenhouse gases. Though the solar, wind or geothermal energies could be converted directly to electrical energy, hydrogen production from the renewable energies is preferred as the electricity form the renewable energy often had unstable current or voltage profiles and could not match the electricity demand. Adopting the hydrogen as an energy carrier can solve these problems. The hydrogen from the renewable energies can be converted to electrical energy with stable power profiles at the very time of power demanded.

In this viewpoint, fuel cell is one of the most promising counterparts of hydrogen production from renewable energies in the “hydrogen economy” as the fuel cells convert directly the chemical energy of hydrogen to electrical energy. The energy conversion efficiency of fuel cells is as high as ~50 %, whereas that of thermal power generation is ~40%. Moreover, the power capacity of fuel cells can be easily expended by increasing the number of fuel cell stacks. Although the advantages of fuel cells for a renewable energy source, there still exists several technical barriers impeding the commercialization of fuel cells including high cost of fuel cell materials and relatively untested reliability.

1.2 Fuel cell basics

There are several types of fuel cells [1] can be categorized by the electrolyte used as summarized in Table 1.1. Among them, polymer electrolyte membrane fuel cells (PEMFCs) are considered attractive for automotive power sources, stationary generation, and residential power supplies due to their low temperature operation, quick start-up, and excellent environmental acceptability. Molten carbonate fuel cel and solid oxide fuel cell are being used for stationary applications as, in combined heat and power generation, the conversion efficiency of the molten carbonate fuel cell (MCFC) and solid oxide fuel cell (SOFC) can be over 85%. Alkaline fuel cell (AFC) is one of the oldest commercialized fuel cells which became known because of Apollo spacecraft. As the AFC requires pure hydrogen as a fuel, AFCs have mostly used in spacecraft or underwater vehicles.

Table 1.1 Comparison of different type of fuel cells.

	Electrolyte	Conducting ions	Catalyst	Operating Temp.	Cell reaction
PEMFC	Proton conducting polymer	H^+	Pt	80 - 200 °C	$H_2 + ½O_2 \rightarrow H_2O$
AFC	KOH in matrix	OH^-	Pt	150 -200 °C	$H_2 + ½O_2 \rightarrow H_2O$
PAFC	H_3PO_4 in SiC matrix	H^+	Pt	150 -250 °C	$H_2 + ½O_2 \rightarrow H_2O$
MCFC	Molten carbonate in $LiAlO_2$	CO_3^{2-}	Ni and Ni oxide	650 °C	$H_2 + ½O_2 + CO_2 \rightarrow H_2O + CO_2$
SOFC	Perovskite	O^{2-}	Perovskite	600 -1000 °C	$H_2 + ½O_2 \rightarrow H_2O$

1.3 Polymer electrolyte membrane fuel cells (PEMFCs)

1.3.1 Structure of the PEMFC

PEMFC systems are consisted of fuel cell stack which generates electricity and balance of plant maintaining the fuel cell stack operation with gas feeding and temperature control. A unit cell in the fuel cell stack is composed of membrane electrode assembly (MEA), porous gas diffusion layer, and current collector which commonly combine fluid channels for fuel and oxidant. The MEA is principal component governing the energy conversion efficiency of PEMFC as the electrochemical reactions (HOR/ORR) occur in the electrode layer in the MEA. Proton conducting electrolyte membrane between the anode and cathode catalyst layer make a MEA.

1.3.2 Thermodynamics in PEMFC

Maximum net work can be obtained from electrochemical reactions is described by:

$$-\Delta G = nFE_{rxn}$$

As the overall reactions in PEMFC is,

$$H_2 + 1/2O_2 = H_2O$$

ideal cell voltage of PEMFC (E) under standard condition is

$$E = E^0 + \frac{RT}{nF}\ln\left(P_{H_2}^2 P_{O_2}\right)$$

where, E^0 is standard electrode potential differences between anode and cathode reaction, R is gas constant, T is temperature, n is number of electrons, F is Faraday's constant, P_{H2} is hydrogen pressure, and P_{O2} is oxygen pressure. If the P_{H2} = P_{O2} = 1 atm and water is liquid state, the ideal cell voltage is 1.229 V

1.4 Electrode reactions in PEMFC

1.4.1 Anode reaction

The anode reaction in the fuel cell is electrochemical oxidation of hydrogen which produces 2 protons and 2 electrons form a hydrogen molecule. The hydrogen oxidation reaction (HOR) is one of the intensively studied electrochemical systems, which is counterpart of hydrogen evolution reaction (HER), and have brought renewed interest due to increased concerns on the fuel cells. The extensive studies on the HOR provided well described reaction mechanism which consisted of three elementary reactions: Tafel reaction (dissociative adsorption of hydrogen molecule without electron transfer), Heyrovsky reaction (dissociative adsorption of hydrogen molecule with electron transfer), and Volmer reaction (desorption of hydrogen atom with charge transfer)

Tafel reaction: 2S (surface active site) + H_2 ⇄ 2S-H

Heyrovsky reaction: 2S + H_2 ⇄ 2S-H + H^+ + e^-

Volmer reaction: S-H ⇄ S + H^+ e^-

In low overpotential reaction on Pt electrode, Volmer reaction followed by Tafel reaction (Tafel-Volmer pathway) was suggested to be principal reaction and the Tafel reaction is rate determining step (RDS) [2]. The Tafel-Volmer pathway is electrochemically reversible reaction and, thus, the kinetics of the HOR could be described as follows:

$$E = E^0 - \frac{RT}{nF} \ln \frac{i_L - i}{i_L}$$

where, E is applied potential, E^0 is equilibrium potential, iL is limiting current dentiy, i is measured current density.

The E^0 can be deduced form the activity coefficient of hydrogen (γ_R) and hydronium ion (γ_O), and formal potential ($E^{0'}$).

$$E^0 = E^{0\prime} - \frac{RT}{nF} ln \frac{\gamma_O}{\gamma_R}$$

The reaction rate of Tafel reaction had been studied on the various transition metals by Conway and Bockris using the HER in acidic electrolyte [3]. They showed linear relationship between $logi_o$ and percent of d-character of metal electrode. The d-character of metals had positive relations with work function level.

Recent remarkable progress in the computational simulations allowed detailed

investigation of reaction pathways of HOR/HER on various model electrode surfaces. Santos and Schmickler tried to match the theoretical prediction and experimental data using an electrochemical bond-breaking model which includes the effect of electrode potential, solvation of hydronium ion on the energy state of reaction species, and the effect of coupling constant.[4] The calculation suggested that high density of d-band stats near the Fermi level decrease the activation energy of HOR. Greeley et al. showed that the increase of hydrogen adsorption energy on Pt/M (M is transition metals) surface alloys lowers transition state energy or activation energy of HOR [5].

1.4.2 Cathode reaction

The cathode reaction in PEMFC is electrochemical reduction of oxygen which produces water. In acidic condition, contrary to the anode reaction, HOR, the oxygen reduction reaction (ORR) is highly irreversible reaction with low exchange current density (typically in the range of 10^{-10}-10^{-11} A cm_{Pt}^{-2}). The overall equation of ORR in acidic aqueous solution is

$$O_2 + 4H^+ + 4e^- \rightarrow 2H_2O,\ E^0 = 1.229\ V\ vs.\ NHE$$

The ORR is a muli-electron reaction that may include numbers of elementary reactions involving chemical and electrochemical processes. Of the carious reaction pathways suggested, the simplified scheme given by Wroblowa et al. is

one of the most effective one to explain the ORR on metal surfaces (Figure 1.1). The reaction pathway 1) is direct reduction pathway.

For reaction pathway 1), so called four electron pathway, the reaction rate of ORR could be described as follows [2]:

$$i_{ORR} = nAFk^0 C_{O_2}(1-\theta_{ad})\exp\left(-\frac{\gamma r\theta_{ad}}{RT}\right)\exp\left(-\frac{\alpha F\eta}{RT}\right)$$

Where, n is number of electron involved in RDS, A is area, k0 is rate constant, CO2 is oxygen concentration, θ_{ad} is total coverage of adsorbing anions and γ and β is transfer coefficient (assumed to be 0.5), r is interaction parameter describing the rate of change of standard Gibbs free energy of adsorption with the surface coverage of adsorbing ions, and η is overpotential.

In the stated equation, the symmetry factor, α, is the transfer coefficient which describes the symmetry of energy barrier on the reaction coordinate (figure 1.2). As shown in figure 1.2, in the narrow region of reaction coordinate, the curves are locally linear. Then, the angles θ and Φ are define by,

$$\tan\theta = \alpha FE/x$$

$$\tan\phi = (1-\alpha)FE/x$$

Hence,

$$\alpha = \frac{\tan\theta}{\tan\phi + tan\,\theta}$$

If the intersection is symmetrical, $\theta = \phi$, and α = 0.5. In most systems, α turns out

to lie between 0.3 and 0.7, and it can usually be approximated by 0.5 in the absence of actual measurements [6].

In order to enhance the ORR activity, there could be several approaches based on the stated rate equation. One is increasing the rate constant by reducing the activation energy (E_a) of reaction. Greeley et al. reported that 6-10 fold activity increase compared to that of Pt was achieved with Pt-ETM (ETM: Y, Sc) alloy [7]. The Pt-Y alloy was suggested to have optimum free energy for ORR intermediates. The other is increase of site availability by decreasing the surface coverage of absorbing anions. Stamenkovic et al. showed that the $Pt_3Ni(111)$ surface is 10-fold more active for ORR than corresponding Pt(111) surface in acidic electrolyte [8]. The decrease of θ_{OH}, increasing the site availability for ORR, was attributed to the increase of ORR activity. Usually the two factors are concomitant and could not be varied independently as the primal and dominant reaction intermediate of ORR is hydroxyl ion. In another word, for homogeneous metal surfaces, tuning the adsorption energy of hydroxyl ion changes the activation energy of ORR and, at the same time, varies the surface coverage of hydroxyl ion.

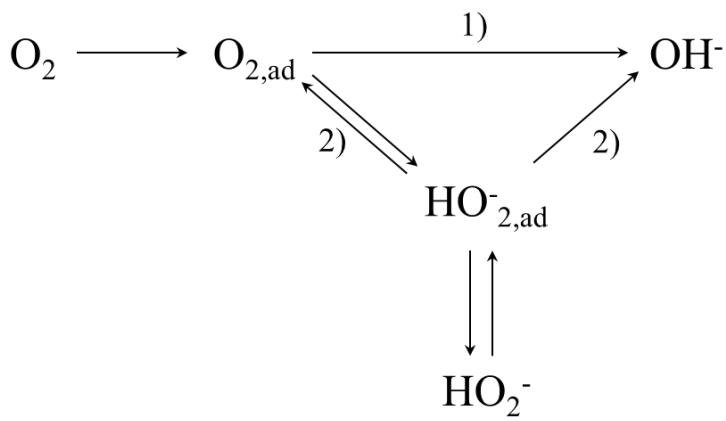

Figure 1.1 ORR reaction scheme for the ORR: 1) direct pathway, and 2) peroxide pathway.

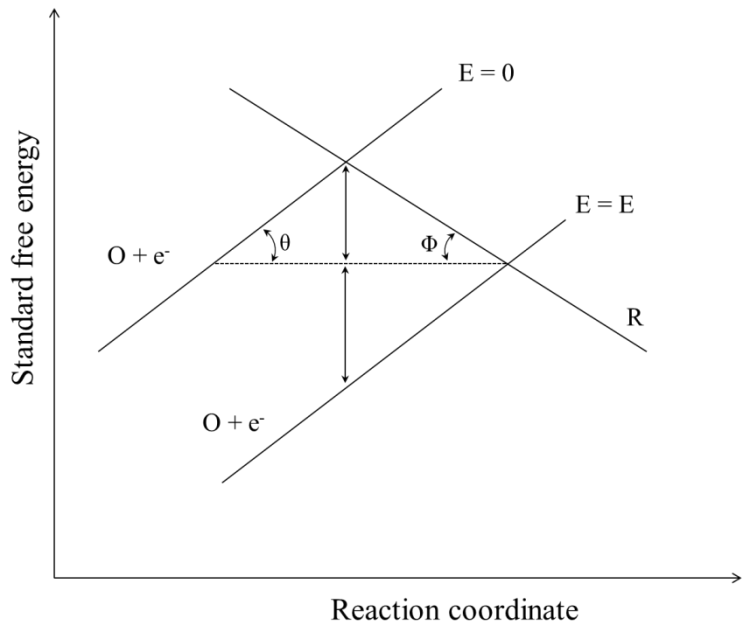

Figure 1.2 Relationship of the transfer coefficient to the angles of intersection of the free energy curves.

1.5 Subject of the thesis

Since electrocatalytic reactions are strongly dependent on the surface structure of metal catalysts, the atom-leveled design of the surface structure plays a significant role in a high catalytic activity and the utilization of electrocatalysts. Therefore, surface-modified electrocatalysts have attracted much attention due to their unique structure and new electronic and electrocatalytic properties. Various methods had been employed to achieve the surface-modified nanoparticles, such as under-potential deposition (UPD), thermal treatment, spontaneous deposition, and successive reduction process.

Recent advances in the surface modified electrocatalysts have been focused on the so called “Pt-skin” structure which expected to have uniform monolayer of Pt on various substrates. The enhanced ORR activity of Pt skin on single crystal substrates had been suggested Marcovich et al. Adzic’s group reported various Pt skin electrocatalyst which was prepared using Cu displace reaction. The Pt skin catalyst showed 10-fold mass activity compared to Pt nanoparticle catalyst. Norskove’s group has intensively investigated the effect of substrate on the electronic structure and electrocatalytic properties of Pt skin catalyst. They suggested “d-band model” which describes the ORR activity of Pt skin catalysts using a one primal parameter, average energy level of filled 5d-band in Pt skin

layer.

Though heterogeneous atoms on the catalyst surfaces affecting the reaction mechanism is common sense, there had been little effort on investigating the effect of heterogeneous atoms on the catalysts surface for hydrogen oxidation reaction or oxygen reduction reaction, whereas, for methanol oxidation reaction, the effect of heterogeneous atoms, so called “bifunctional effect” had been widely investigated. Traditionally, the ORR and HOR characteristics of alloy which may have heterogeneous atoms on the catalyst surfaces had been investigated based on the bulk properties of alloy catalyst, such as electronic structure and lattice parameter, though intensive research had been conducted.

In this thesis, the effect of surface modification on the ORR/HOR activity was investigated using carbon supported nanoparticle catalysts which have various surface modification methods and discussed based on the effect of heterogeneous atoms in the catalyst surfaces. The surface modifications were conducted in three different ways: 1) deposition of Pt-sub-monolayer shell on Pd-core nanoparticles, 2) thermal treatment of Pt-Au alloy nanoparticles under CO or Ar gas which led to different surface Pt-Au compositions but identical bulk compositions, and 3) selective adsorption of phosphoric acid on Se in $RuSe_y$/C catalyst.

1.6 References

[1] M. Debe, Handbook of Fuel Cells-Fundamentals, Technology, and Applications, in, 2003, pp. 576-589.

[2] T.J. Schmidt, V. Stamenkovic, J.P.N. Ross, N.M. Markovic, Temperature dependent surface electrochemistry on Pt single crystals in alkaline electrolyte Part 3. The oxygen reduction reaction, Physical chemistry chemical physics, 5 (2003) 400-406.

[3] B.E. Conway, J.O.M. Bockris, The d-Band Character of Metals and the Rate and Mechanism of the Electrolytic Hydrogen Evolution Reaction, Nature, 178 (1956) 488-489.

[4] E. Santos, W. Schmickler, Electrocatalysis of hydrogen oxidation - Theoretical foundations, Angewandte Chemie - International Edition, 46 (2007) 8262-8265.

[5] J. Greeley, M. Mavrikakis, Near-surface alloys for hydrogen fuel cell applications, Catalysis Today, 111 (2006) 52-58.

[6] A.J. Bard, L.R. Faulkner, Electrochemical methods : fundamentals and applications, 2nd ed., John Wiley & Sons, Inc., New York, 2001.

[7] GreeleyJ, I.E.L. Stephens, A.S. Bondarenko, T.P. Johansson, H.A. Hansen, T.F. Jaramillo, RossmeislJ, ChorkendorffI, J.K. Norskov, Alloys of platinum and early transition metals as oxygen reduction electrocatalysts, Nature Chemistry, 1

(2009) 552-556.

[8] V.R. Stamenkovic, B. Fowler, B.S. Mun, G.F. Wang, P.N. Ross, C.A. Lucas, N.M. Markovic, Improved oxygen reduction activity on Pt3Ni(111) via increased surface site availability, Science, 315 (2007) 493-497.

Chapter 2

Experimental

2.1 Catalyst preparation

2.1.1. Reagents

$Pd(OAc)_2$ (Aldrich Chemical, 99.9%), $Pt(acac)_2$ (Aldrich Chemical, 99.9%), $HAuCl_4 \cdot 3H_2O$ (Aldrich Chemical, 99.9%), $H_2PtCl_6 \cdot xH_2O$ (Aldrich Chemical, 99.99%), $Na_3C_6H_5O_7 \cdot 2H_2O$ (Aldrich Chemical, ACS reagent), $NaBH_4$ (Aldrich Chemical, ACS reagent), 1-decylalcohol (Aldrich Chemical, 99.9 %), $RuCl_3$ (Aldrich Chemical, 99.99%), SeO_2 (Aldrich Chemical, 99.99%), Vulcan® XC72 (Cabot Corp., Boston, MA, USA), $HClO_4$ (Aldrich Chemical, ACS reagent), methanol (Aldrich Chemical, ACS reagent), benzoic acid (Aldrich Chemical, 99%), and 2-propanol (Aldrich Chemical, HPCL grade) were used without further purification. All aqueous solutions were made with deionized (DI) water, which was further purified using a Milli-Q system (18.2 MΩ cm; Millipore, Bedford, MA, USA).

2.1.2 Pt-sub-monolayer-shell@Pd-core nanoparticles

Pt-sub-monolayer-shell@Pd-core nanoparticles were prepared using a colloidal approach with modifications [1]. Briefly, the Pd salt and PVP were dissolved in 200 mL of 1-decylalcohol. The solution was refluxed at 130℃ for 12 hours under an Ar atmosphere to obtain a dark brown colloid solution and then cooled to room temperature. The appropriate amount of $Pt(acac)_2$ was dissolved in 20 mL of 1-decylalcohol and added to the colloid solution. The mixture was refluxed at 130 ℃ for 12 hours under an Ar atmosphere, and we obtained the Pt_x@Pd (The x is the Pt surface concentrations calculated from HR-XPS intensities of Pt 4f and Pd 3d) colloid solution. Carbon black powder (0.1801 g, Vulcan® XC-72) and a benzoic acid/methanol solution were added to the Pt_x@Pd colloid solution to obtain carbon supported Pt_x@Pd nanoparticles (Pt_x@Pd/C). The Pt_x@Pd/C was washed with a large volume of methanol and water to remove impurities and then dried at room temperature. Carbon supported Pd nanoparticles (Pd/C) were also prepared with the same procedure as the Pt_x@Pd/C, except for the addition of Pt salt.

2.1.3 Surface-modified PtAu alloy nanoparticles

Carbon supported PtAu nanoparticle catalysts (40 wt% PtAu/C) were prepared by modifying the method from previous work done by our group [2]. Briefly, an

appropriate amount of $H_2PtCl_6 \cdot xH_2O$ (0.128 mmol), $HAuCl_4 \cdot 3H_2O$ (0.128 mmol), and sodium citrate (0.068 mmol) was dissolved in 800 ml of DI water. Under vigorous stirring, an aqueous solution of sodium citrate (0.034 mmol) and sodium borohydide (2.64 mmol) was quickly added to the precursor solution. The color of the solution immediately changed from transparent yellow to translucent dark brown, indicating colloid formation. After thirty minutes, 0.075 g of carbon support (Vulcan-XC72) was added to the colloid solution and stirred for 12 hr and followed by addition of 200 ml of a 0.2 M $HClO_4$ solution. The mixture was filtered and washed with a copious amount of water. The catalyst was dried at room temperature and denoted as PtAu-AP. The surface segregation process was conducted using a tube furnace at 423 K for 1 hr under a CO (99.9 %) or Ar (99.999 %) atmosphere to achieve a Pt or Au segregated surfaces, which was denoted as PtAu-CO and PtAu-Ar, respectively. The CO or Ar flow during surface segregation was 500 cm^3 min^{-1}.

2.1.4 Se-modified-Ru nanoparticles on carbon support

The Ru/C and $RuSe_y$/C catalysts were prepared by a reported procedure [3]. Briefly, Vulcan XC-72 carbon was dispersed in 250 mL of water with ultrasonic agitation and stirring. Appropriate amount of $RuCl_3$ and SeO_2 were dissolved in the carbon/water mixture. Before the chemical reduction process, the reaction vessel

was purged with Ar for 1 hr. The precursor-carbon mixture solution was heated up to 80 ℃ and cooled to room temperature. An aqueous solution of $NaBH_4$ in 0.1 M NaOH (20 mL) was added drop wisely to the mixture solution using a syringe pump for 2 h and a black precipitate was obtained. The black precipitate, $RuSe_y/C$, was filtered and washed with copious amount of water and dried under vacuum. For Ru/C, the same procedure for Ru_xSe_y/C was adopted without addition of SeO_2. The catalysts were stored in vacuum desiccator to prevent further oxidation of catalyst. The nominal Ru-to-carbon ratio was 20% by weight and the atomic ratios of Se-to-Ru were nominally 33%, 66% and 133%.

2.2 Physicochemical characterizations

2.2.1 X-ray diffraction

X-ray diffraction (XRD) is a non-destructive, relatively easy, and fast analyzing technique in examining the structure of materials. The diffractions originated the existence of phase relations between two or more X-ray waves. In the case of X-ray diffraction of a crystal, an interaction between the incident X-ray and the crystalline planes which satisfy Bragg condition make constructive interference.

$$n\lambda = 2d \sin\theta$$

where, n is the order of diffraction (natural number), λ is wave length of the X-ray, d is the distance between crystalline planes, and θ is incident angle of X-ray. In θ-2θ scan mode, the diffraction angle of perfect crystal gives crystallographic structure of materials, such as crystal structure and lattice parameter. Imperfectness of crystal make line broadening of diffraction peak which is commonly represented by full with half maxima (FWMH). As the finite size of crystal gave increase of FWHM which follows the Scherrer equation, the crystalline size of nanoparticles can be calculated form the line broadening of XRD peak.

$$\mathrm{L} = \frac{K\lambda}{B\cos\theta}$$

Where, L is crystalline size, K is constant which is subject to the shape of crystals, λ is wave length of X-ay, B is the FWMH in radians, and θ is diffraction angle of the crystal plane.

In this thesis, the XRD analysis was performed using a D/MAX 2500 (Rigaku) or MINI FLEX diffractometer (Rigaku) with an X-ray wave length of 0.154056 nm.

2.2.2 Transmission electron microscopy

Transmission electron microscopy (TEM) constitutes one of the most efficient and versatile tools for the characterization of materials over spatial ranges from the atomic scale up to the micrometer level. Extremely short wavelength of electron beam (~4 pm for electron energy of 100 keV) allowed characterizing the atomic arrangement of the materials with a spatial resolution of below ~0.1 nm [4]. TEM is impressive instrument for the characterization of nano-sized materials with a number of advantages: powerful magnifications, elemental resolution with a scanning prove apparatus, and an intuitive grasp of the structure and shape of nano-materials. However, as here exist potential limitations of TEM analysis, such as projection artifact, electron beam damage, and narrow sampling range, careful attention is needed analyzing the TEM images.

In this thesis, TEM images were taken by using a JEOL 2010 or TEKNI F-20 electron microscope for TEM and scanning transmission electron microscopic images, respectively, at the acceleration voltage of 200 kV. The samples were prepared by dispersing a small part of catalyst powder in ethanol with ultrasonic agitation. Then, the catalyst/ethanol mixture was dropped onto a carbon coated copper grid and dried under vacuum at 40 ℃.

2.2.3 X-ray photoelectron spectroscopy

X-ray photoelectron spectroscopy (XPS) is one of the most widely used surface analysis technique because of its relative simplicity in use and data interpretation. XPS utilizes photo-ionization and analysis of the kinetic energy distribution of the emitted photoelectrons to study the composition and electronic state of the surface region of a sample. Photoelectron spectroscopy is based upon a single photon in-electron out process. The energy of a photon of all types of electromagnetic radiation is given by the Einstein relation:

$$E = h\nu$$

where, h is Planck constant (6.62×10^{-34} J s) and ν is frequency (Hz) of the radiation.

The kinetic energy distribution of the emitted photoelectrons can be measured using any appropriate electron energy analyzer. Since the electron's energy is present solely as kinetic energy (KE) this can be rearranged to give the following expression for the KE of the photoelectron:

$$KE = h\nu - BE - q\Phi_{sp}$$

Where, BE is the difference in energy between the ionized and neutral atoms, so called “binding energy” and Φ_{sp} is work function of the analyzer (3~4 eV). As the

KE depends on the incident X-ray energy, the X-ray being monochromatic is important.

The chemical surrounding of the X-ray absorbing atoms affect the BE, the chemical state of materials could be analyzed comparing the BEs of samples to known reference materials. The BEs for elements and compounds are easily available in handbooks and graphs.

As the mean free path of the photoelectrons in metals are below a few nanometers, despite the deeper penetration of the incident X-rays, XPS is considered surface sensitive method. As the penetration depth of photoelectrons is governed by the KE of the photoelectron, the higher incident X-ray energy provides the deeper analyzing depth. Despite the short penetration depth of photoelectrons from conventional X-ray sources, the XPS signal contains bulk properties as well as surface properties of materials if one analyzes nano-sized samples. Thus, care should be taken in analyzing XPS data from nano-sized materials.

In this thesis, two X-ray sources were used to characterize the surface structure of the catalysts: synchrotron radiation in Pohang Acceleration Laboratory (PAL) and Al K_{α} radiation. Using a synchrotron radiation source (8A in PAL) (Figure 2.1) allowed changing the energy of incident X-ray form 1k eV to 0.1k eV.

The decrease of incident X-ray energy led to the decrease of photoelectron mean free path and made it possible to analyze the surface composition of nanoparticles.

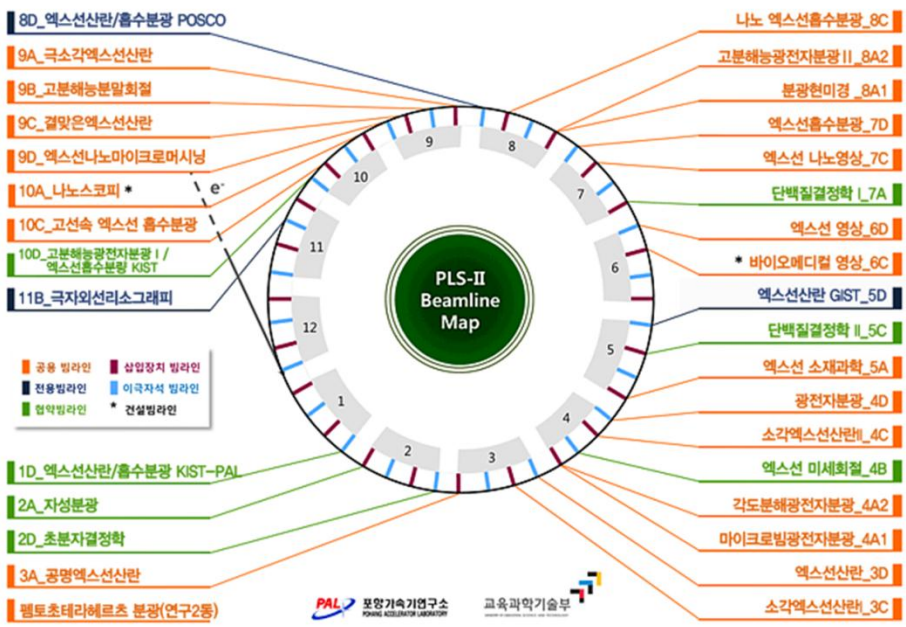

Figure 2.1 Beamline map in the PAL. Form the webpage, http://pal.postech.ac.kr.

2.3 Electrochemical characterizations

2.3.1 Cyclic voltammetry

Cyclic Voltammetry (CV) is one of most effective and versatile technique available for the study of redox systems. In general redox system,

$$O + e^- \leftrightarrows R$$

due to the periodical inversion of potential sweep directions, surface concentration of O or R changes periodically. The maximum concentration of O or R can be achieved in the point of inversion. Similarly, adsorption/desorption of electrochemical species on electrodes also can be analyzed easily using the CV.

For the analysis of electrocatalysts for fuel cell applications, generally carbon supported Pt nanoparticles, adsorption/desorption of hydronium ion and hydroxyl anion was primal concern as the adsorbed hydronium ion and hydroxyl anion were major reaction intermediates of HOR and ORR, respectively.

2.3.2 Rotating disk electrode technique

Rotating disk electrode (RDE) technique is a primal electrochemical technique in which the electrode moves with respect to the solution. The methods involving convective mass transport of reactant and product are referred to “hydrodynamic method”.

Among the hydrodynamic methods, RDE is one of the few system for which the hydrodynamic equations and convective-diffusion equation have been solved rigorously for steady state. The RDE is consisting of a disk of electrode material, commonly glassy carbon or platinum, in a rod of insulating material (Figure 2.2).

The general equation of the flux species j, $\mathbf{J_j}$, is

$$\boldsymbol{J_j} = -D_j \boldsymbol{\nabla C_j} - \frac{Z_j F}{RT} D_j C_j \boldsymbol{\nabla} \emptyset + C_j \mathbf{v}$$

where the "$-D_j \boldsymbol{\nabla C_j}$" represents diffusion term, "$-\frac{Z_j F}{RT} D_j C_j \boldsymbol{\nabla} \emptyset$" is for migration, and "$C_j V$" describes convection. For solutions containing excess of supporting electrolyte, the ionic migration, "$-\frac{Z_j F}{RT} D_j C_j \nabla \emptyset$", can be neglected. The velocity vector, **v**, represents the motion of the solution and is given in rectangular coordinates by

$$\mathbf{v}(x, y, z) = \mathbf{i} v_z + \mathbf{j} v_y + \mathbf{k} v_z$$

where i, j, and k are unit vectors, and v_x, v_y, and v_z are the magnitude of the solution velocities in the x, y, and z directions at point (x,y,z).

In rectangular coordinates, diffusion term of the equation is,

$$\boldsymbol{\nabla C_j} = \mathbf{i}\frac{\partial C_j}{\partial x} + \mathbf{j}\frac{\partial C_j}{\partial y} + \mathbf{k}\frac{\partial C_j}{\partial z}$$

The variation of C_j with time is given by

$$\frac{\boldsymbol{\partial C_j}}{\boldsymbol{\partial t}} = -\boldsymbol{\nabla} \cdot \mathbf{J}_j$$

By combining the general flux equation and the velocity vector equations, assuming that the migration is absence and the diffusion coefficient, D_j, is not a function of x, y, and z, we can obtain the general convective-diffusion equation:

$$\frac{\boldsymbol{\partial C_j}}{\boldsymbol{\partial t}} = D_j \nabla^2 C_j - \mathbf{v} \cdot \boldsymbol{\nabla} \mathbf{C}_j$$

In RDE conditions, the velocity profile, **v**, of a fluid near a rotating disk was given by von Karman and Cochran by solving the hydrodynamic equations under steady-state [5, 6]. For cylindrical coordinates (figure 2.3), the velocity profile is,

$$\mathbf{v} = \boldsymbol{\mu_1} v_r + \boldsymbol{\mu_2}\,\mathbf{j} v_y + \boldsymbol{\mu_3} v_\phi$$

$$\boldsymbol{\nabla} = \boldsymbol{\mu_1}\left(\frac{\partial}{\partial r}\right) + \boldsymbol{\mu_2}\left(\frac{\partial}{\partial y}\right) + \left(\frac{\boldsymbol{\mu_3}}{r}\right)\left(\frac{\partial}{\partial \emptyset}\right)$$

where, $\boldsymbol{\mu_1}$, $\boldsymbol{\mu_2}$, and $\boldsymbol{\mu_3}$ are unit vectors in the dirctions of position changes of r, y, and $\emptyset$ at a given position.

At a fixed RDE rotating speed of ω, the steady state convective-diffusion equation, written in terms of cylindrical coordinates, becomes

$$v_r\left(\frac{\partial C_o}{\partial}\right) + \frac{v_\emptyset}{r}\left(\frac{\partial C_o}{\partial}\right) + v_y\left(\frac{\partial C_o}{\partial}\right) = D_o\left[\frac{\partial^2 C_o}{\partial y^2} + \frac{\partial^2 C_o}{\partial} + \frac{1}{r}\frac{\partial C_o}{\partial} + \frac{1}{r^2}\left(\frac{\partial^2 C_0}{\partial}\right)\right]$$

Adopting the boundary conditions at limiting current state, y=0, Co==, and $\lim_{y\to 0} C_o = C_o^*$, one can obtain the Levich equation:

$$i_l = 0.62nFAD_o^{2/3}\omega^{1/2}\nu^{-1/6}C_o^*$$

where, n is number of electrons involved the reaction, A is area, D_o is diffusion coefficient of reactant, ω is rotating speed of RDE, ν is kinematic viscosity of electrolyte, and C_o^* is bulk concentration of reactant.

In the study, the electrochemical data collected using the RDE technique was analyzed using the Koutechy-Levich equation:

$$\frac{1}{i} = \frac{1}{i_k} + \frac{1}{0.62nFAD_o^{2/3}\omega^{1/2}\nu^{-1/6}C_o^*}$$

where, i is the measured current and i_k is kinetic current which reflected the activity of electrocatalyst.

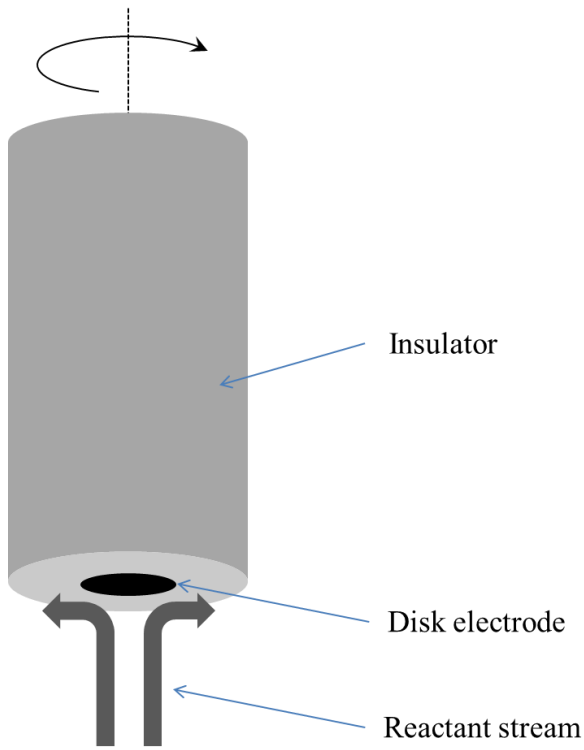

Figure 2.2 Schematic representation of an RDE.

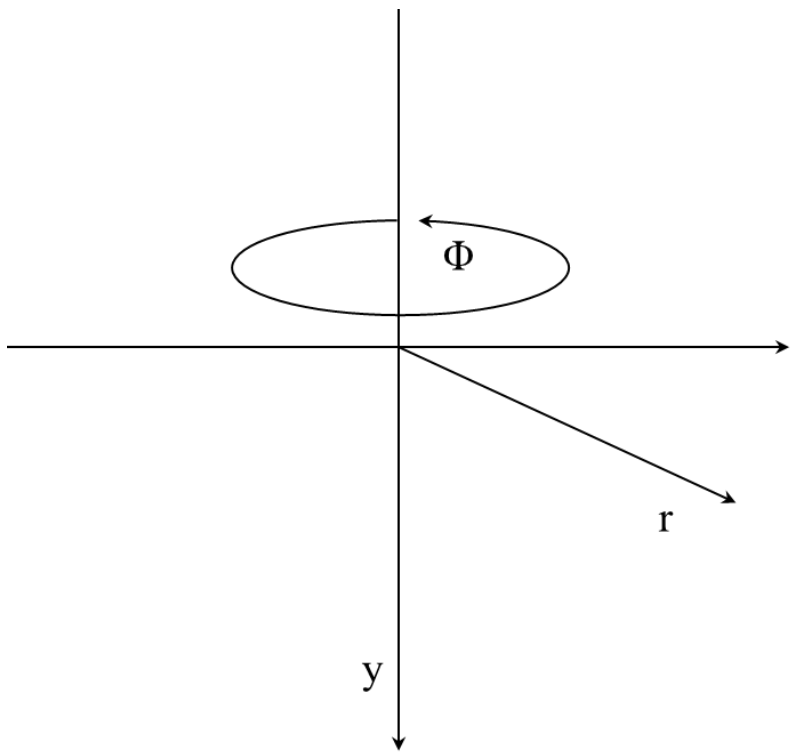

Figure 2.3 Cylindrical coordinate for an RDE.

2.3.3 CO electrooxidation

Electrooxidation of pre-adsorbed CO molecules, so called "CO stripping voltammetry", on electrocatalysts has been widely adopted to investigate the electrochemical properties of Pt or platinum group metal nanoparticle catalysts. The mechanism of electrochemical oxidation of CO on Pt electrode is given follows [7]:

$$Pt + CO \rightarrow Pt\text{-}CO_{ad}$$

$$Pt + H_2O \rightarrow Pt\text{-}OH_{ad} + H^+ + e^-$$

$$Pt\text{-}CO_{ad} + Pt\text{-}OH_{ad} \rightarrow 2Pt + CO_2 + H^+ + e^-$$

The oxidation rate of CO on Pt single crystal electrodes have been rigorously investigated in acidic solutions. The reaction was well characterized with Langmuir–Hinshelwood model and RDS was reaction between CO_{ad} and OH_{ad} [8].

2.3.4 CO-displacement method

In order to determine potential of zero total charge (PZTC), CO-displacement method reported by Orts et al. was employed [9]. The PZTC was determined form the voltammetric contributions of specifically adsorbed anions that was displaced

by neutral prove, CO. Briefly, CV was recorded in Ar saturated electrolyte to characterize the total charge contribution of anion and cation in the potential range where is expected to cover PZTC. Then, CO was introduced into the Ar saturated electrolyte at a constant electrode potential, 0.05 V. During CO adsorption, the resulting displacement current was recorded and calculated into charge by integration. In order to calculate PZTC, the CO-displacement charge was subtracted from the charge contributions determined form CV. The PZTC is a potential where the subtraction equals zero. The schematic of calculating the PZCT form the charge contributions of CO-displacement and CV was presented in Figure 2.4. At CO adsorption potential (E_{ad}), total CO-displacement charge is sum of the anionic contributions and cationic contributions ($Q^{total}_{CO\text{-}displaecement}$). Note that the anionic (Q^{-}_{CO}) and cationic (Q^{+}_{CO}) charges due to the CO-displacement have opposite direction. At the potential of E where the CO displacement charge is equal to total charge contributions of CV,

$$Q^{total}_{CO\text{-}displaecement} = Q^{+}_{CV} + (-Q^{-}_{CV})$$

where, Q^{+}_{CV} is cationic charge contribution of CV, in this case underpotentially adsorbed hydrogen, and Q^{-}_{CV} is anionic charge contribution of CV.

Thus, we can obtain

$$Q^{+}_{E} - (Q^{-}_{E} - Q^{-}_{CV}) = -2 \times Q^{-}_{CO\text{-}displacement} - Q^{-}_{CV}$$

where, Q^{+}_{E} and Q^{-}_{E} represent surface charge from cations and anions, respectively.

As shown in the figure 2.4,

$$Q^{-}_{E} - Q^{-}_{CV} = Q^{-}_{CO\text{-}diplacement}$$

Finally, we can obtain

$$Q^{+}_{E} = -Q^{-}_{CO\text{-}displacement} - Q^{-}_{CV} = -Q^{-}_{E}$$

Thus, from the definition of PZTC, the potential of E where the charge contributions form CO-displacement is equal to that from CV is PZTC.

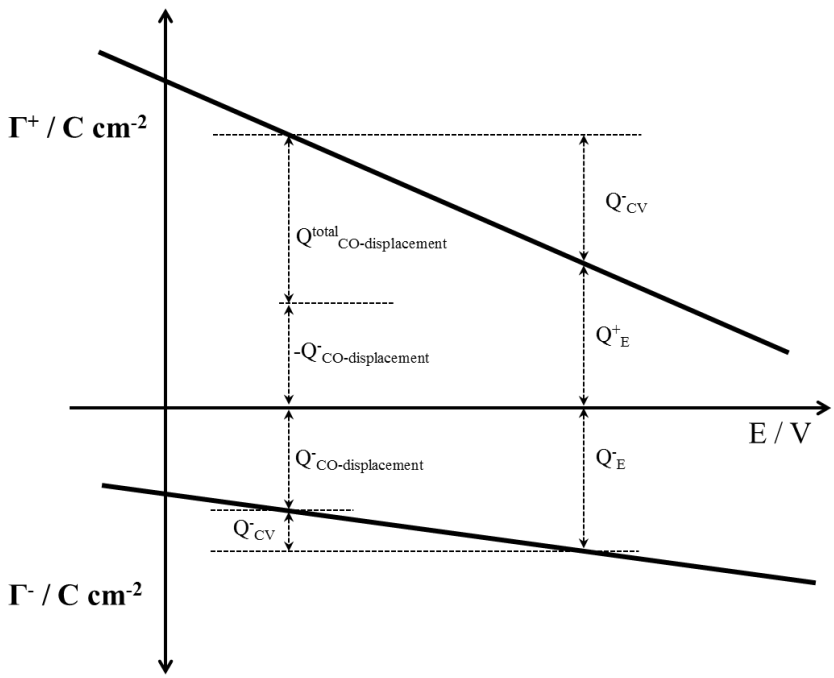

Figure 2.4 Schematic representation of method for calculating PZTC from the CO-displacement charge ($Q^{totoa}_{CO\text{-}displacement}$) and charge contribution of CV (Q_{CV}).

2.4. Electrochemical *in-situ* X-ray absorption spectroscopy

2.4.1 X-ray absorption spectroscopy (XAS)

X-rays are ionizing radiation and thus, by definition, have sufficient energy to eject a core election from an atom. Each core level has a distinct binding energy, and thus, there is an abrupt increase in absorption cross-section, so called "absorption edge" during energy scan of X-ray through the binding energy of a core level. (figure 2.5a) The X-ray absorption can be understood form the Fermi's Golden Rule which describes transition rate from an initial state to a final state that is part of a continuum of states:

$$\mathcal{W} = \frac{d\mathcal{P}(t)}{dt} = \frac{2\pi}{\hbar} W_{fi}^2 \rho(E_{fi})$$

Where, $\mathcal{W}$ is transition rate, $\mathcal{P}(t)$ is probability of finding the system in the eigenstate $|\varphi_f\rangle$, W_{fi} is perturbation matrix element of the transition from initial state to final state, and $\rho(E_{fi})$ is density of state.

The XAS often interpreted two regions: X-ray absorption near edge structure (XANES) and Extended X-ray absorption fine structure (EXAFS) region (figure 2.5b). Despite the same fundamental physics governing the photoabsorption over the entire XAS region, the EXAFS and XANES are widely used as the

EXAFS and XANES regions are commonly analyzed differently. XANES is sensitive to the oxidation state and chemical environment of absorbing element, but hardly analyzed quantitatively. Contrary, the EXAFS region is sensitive to the radial distribution of electron density around the absorbing atoms and is useful to analyze quantitatively the bond length and coordination number.

Schematic representation of XAS apparatus was shown in Figure 2.6. The XAS apparatus consists of an X-ray source, a double-crystal monochrometer (DCM), detectors collecting the intensities of incident beam (i_0), fluorescence (i_f), reference (i_r), and transmission (i_t), and data acquisition system.

XAS of Pt L_{III} were measured in 10A beamline of PAL. Before the measurements, X-ray energy was calibrated respect to the Pt L_{III} edge energy of Pt foil. The incident X-ray flux was detuned by 30 % to banish high order harmonics from Si(111) monochrometer. XAS spectra were collected using a fluorescence detector in air ambient and recorded. The XAS data were process to obtain the absorbance and analyzed with ATHENA and ARTHEMIS software. The pre-edge absorption was corrected using a linear fit of data in the range of from -200 to -70 eV respect to absorption edge energy (E_0). The E_0 was determined from the first inflection point of first derivative of absorption edge. The XANES spectra were obtained by normalization.

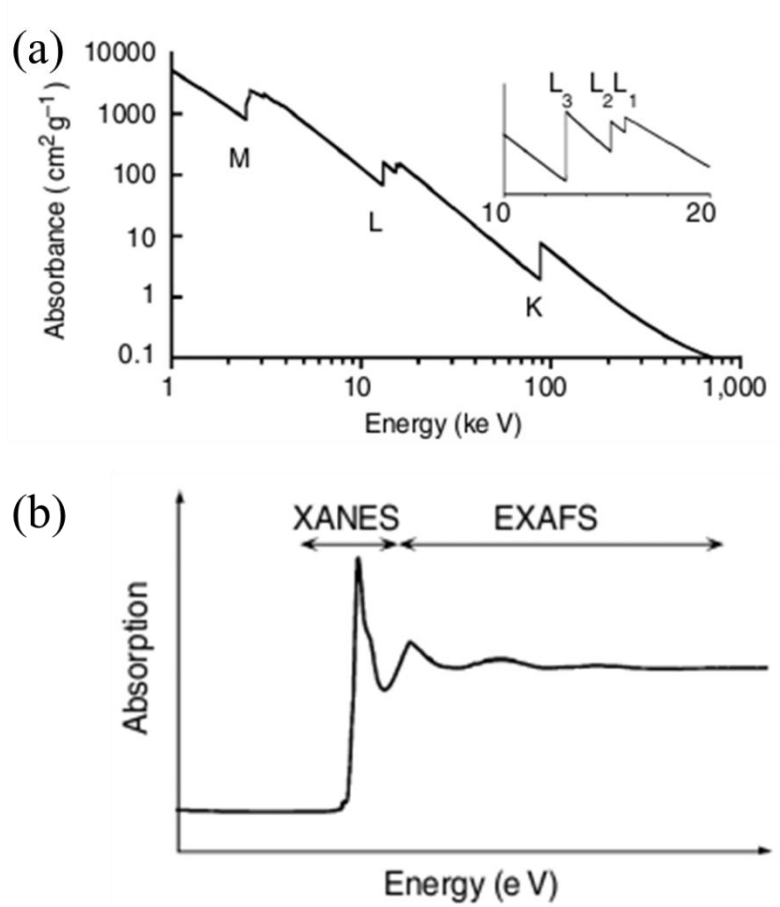

Figure 2.5 (a) Low resolution and higher resolution (inset) X-ray absorption spectrum for Pb. (b) Schematic illustration of an X-ray absorption spectrum, showing the structured absorption that is seen both within ca. 50 eV of the edge (XANES) and for several hundred to >1,000 eV above the edge (EXAFS) [10].

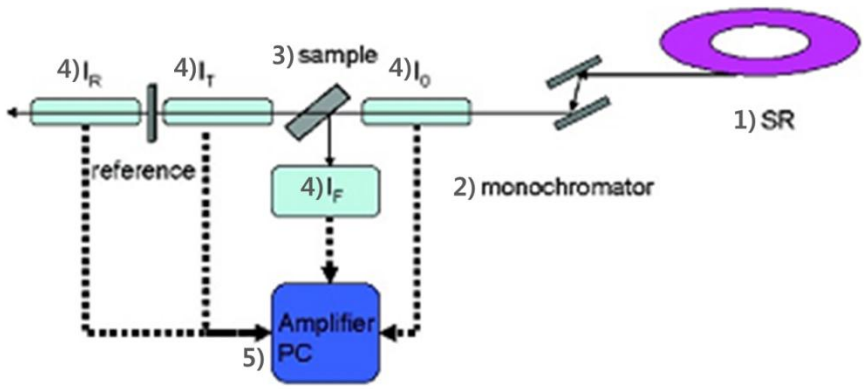

Figure 2.6 Typical XAFS setup diagram. The five parts of the experiment are (1) the X-ray source from synchrotron radiation, (2) the optics, monochrometer, (3) sample, (4) detectors, and (5) the electronics and computer [11].

2.4.2 Electrochemical in-situ XAS

In-situ XAS of Ru K and Se K were measured in 10C beamline of PAL with a homemade electrochemical cell. Figure 2.7 and Figure 2.8 gave a schematic and real image of electrochemical cell for XAS, respectively. The cell was made of polytetrafluoroethylene (PTFE) to avoid corrosion of electrochemical cell during measurement.

The working electrode was catalyst coated carbon paper (Toray 10 BC). Before measurement, the working electrode was fully hydrated in contact with deionized water to achieve facile proton transfer in the catalyst layer. The working electrode was place in the electrochemical cell, and then CV was carried out in the potential range of -0.2 V ~ 0.8 V respect to NHE with a scan rate 5 mV s^{-1}. The XAS was recorded under constant potentials of 50 mV, 300 mV, 600 mV, 800 mV and 1 V. Total collection time of XAS for the five electrode potentials was ~5 h. A silver/silver chloride and a glassy carbon rod were used as a reference and counter electrode, respectively. In order to investigate the effect of phosphoric acid adsorption on the XAS of Ru/C and $RuSe_y$/C catalyst, XAS measurement was performed in Ar-purged 0.1 M $HClO_4$ and 0.1 M $HClO_4$ + 10 mM H_3PO_4 solution. Electrode potential of the working electrode was controlled by a PGSTAT potentiostat (AUTOLAB).

Before the measurements, the photon energy of incident X-ray was calibrated respect to the Ru K and Se K edge energy of corresponding reference foil, respectively. The incident X-ray flux was detuned by 50 % to banish high order harmonics from Si(111) monochrometer. XAS spectra were collected using a fluorescence detector in air ambient and recorded. The XAS data were process to obtain the absorbance and analyzed with ATHENA and ARTHEMIS software. The pre-edge absorption was fitted using a linear fit of data in the range of from -200 to -70 eV respect to E_0 and followed by extrapolation over the energy range of measurement and subtracted from the XAS data. The background corrected XAS data was normalized using an extrapolation of a third-order polynomial fit of XAS data over the 150-1000 eV respect to E_0.

The Extended X-ray absorption fine structure (EXAFS) spectra were isolated from the normalized XAS by subtracting a background which was approximated with a piecewise spline. The k^2-weighted EXAFS function, $\chi(k^2)$, was Fourier Transformed to radial distribution functions to show the distance and coordination of the neighboring atoms around absorbing atoms. The Fourier Transform was performed in the k range of 2-3 Å (k_{min}) ~ 12-13 Å (k_{max}). Kaiser-Bassel function was adopted as a window function. The R-range of the radial distribution function was restricted to 1-4 Å to avoid meaningless signals and multiple scattering effects.

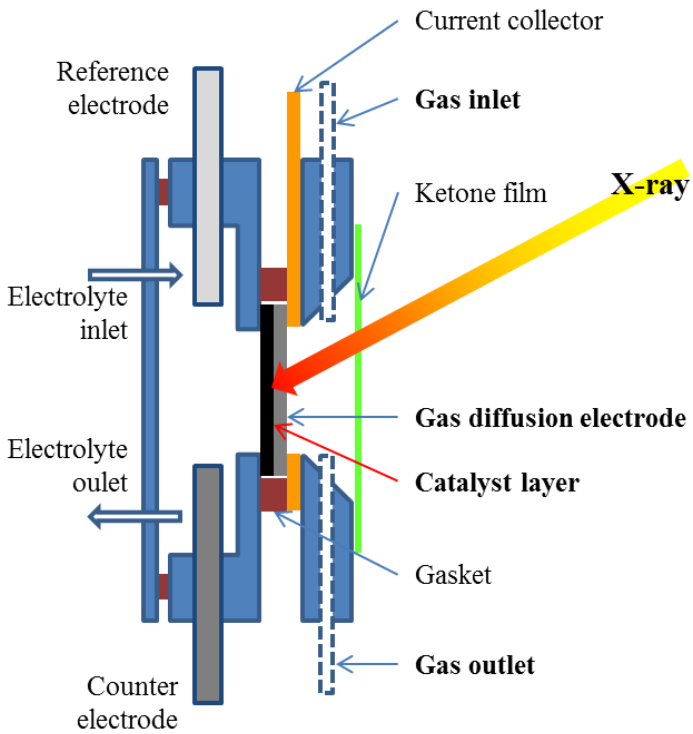

Figure 2.7 Schematic of electrochemical cell for *in-situ* XAS.

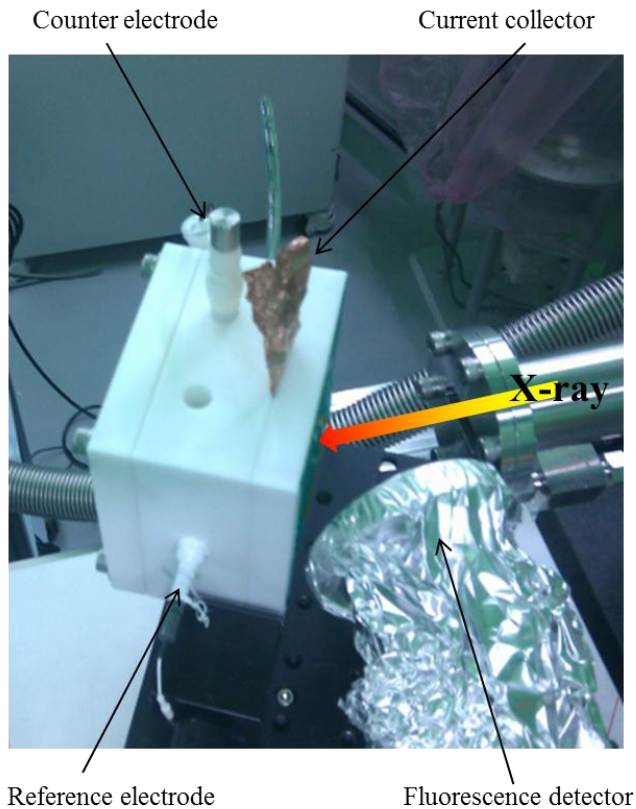

Figure 2.8 Image of electrochemical cell for *in-situ* XAS.

2.5 References

[1] D. Mandler, I. Willner, Photohydrogenation of acetylenes in water-oil two-phase systems: application of novel metal colloids and mechanistic aspects of the process, The Journal of Physical Chemistry, 91 (1987) 3600-3605.

[2] I.S. Park, K.S. Lee, J.H. Choi, H.Y. Park, Y.E. Sung, Surface structure of Pt-modified Au nanoparticles and electrocatalytic activity in formic acid electro-oxidation, The Journal of Physical Chemistry C, 111 (2007) 19126-19133.

[3] C. Delacôte, A. Bonakdarpour, C.M. Johnston, P. Zelenay, A. Wieckowski, Aqueous-based synthesis of ruthenium-selenium catalyst for oxygen reduction reaction, Faraday Discussions, 140 (2009) 269-281.

[4] D.B. Willams, C.B. Carter, Transmission electron microscopy, 2nd edtion ed., Springer, New York, 2009.

[5] W.G. Cochran, The flow due to a rotating disc, Mathematical Proceedings of the Cambridge Philosophical Society, 30 (1934) 365-375.

[6] T.V. Kármán, Ü ber laminare und turbulente Reibung, Zeitschrift für Angewandte Mathematik und Mechanik, 1 (1921) 233-252.

[7] S. Gilman, The Mechanism of Electrochemical Oxidation of Carbon Monoxide and Methanol on Platinum. II. The "Reactant-Pair" Mechanism for Electrochemical Oxidation of Carbon Monoxide and Methanol1, The Journal of

Physical Chemistry, 68 (1964) 70-80.

[8] P. Inkaew, C. Korzeniewski, Kinetic studies of adsorbed CO electrochemical oxidation on Pt(335) at full and sub-saturation coverages, Physical chemistry chemical physics, 10 (2008) 3655-3661.

[9] J.M. Orts, R. Gómez, J.M. Feliu, A. Aldaz, J. Clavilier, Potentiostatic charge displacement by exchanging adsorbed species on Pt(111) electrodes—acidic electrolytes with specific anion adsorption, Electrochimica Acta, 39 (1994) 1519-1524.

[10] J.E. Penner-Hahn, X-ray absorption spectroscopy, Elsevier Ltd., 2003.

[11] Z. Li, E. Dervishi, V. Saini, L. Zheng, W. Yan, S. Wei, Y. Xu, A.S. Biris, X-ray Absorption Fine Structure Techniques, Particulate Science and Technology, 28 (2010) 95-131.

Chapter 3

Results and discussion

3.1 Pt-sub-monolayer-shell on Pd-core nanoparticles

Carbon supported Pt nanoparticles have been considered one of the most efficient catalysts for HOR and ORR but limited deposits and the high price of Pt are crucial obstacles for commercialization of PEMFC. To reduce Pt consumption, Pt skin electrocatalysts, so-called “core/shell”, which have Pt overlayers on other metals, have been suggested, because the electrochemical reactions only occur on the catalyst surfaces. In addition to high Pt utilization, the electrochemical activity of Pt overlayers is enhanced by the substrates due to interactions between Pt overlayers and the substrate [1]. Thus, there have been many attempts to make thin Pt films on various metal nanoparticles for PEMFC applications [2-8].

Due to ligand and geometric effects, Pd is one of the most efficient core materials for core/shell electrocatalysts of the HOR and ORR [9]. As the effect of substrates is known to be limited to a few overlayers, generating uniform Pt shells on Pd nanoparticles is a significant issue to achieve high catalytic activity with

minimized Pt use. The Pt shells on Pd or Pd alloy nanoparticles have been synthesized by electrochemical methods [1, 5, 10] and chemical reduction processes [2, 11-15]. Adzic et al. reported that uniform Pt shells could be prepared on Pd nanoparticles by an electrochemical method to provide Pd-core/Pt-shell catalysts with enhanced activity [5].

Monolayer or more Pt shells on Pd nanoparticles have been widely investigated for core-shell catalyst development, but a sub-monolayer Pt shell on Pd nanoparticles has received less attention. As the sub-monolayer core-shell electrocatalysts have heterogeneous atoms on their surface, the electrochemical properties of the sub-monolayer core-shell nanoparticles may differ from those of monolayer or multilayer Pt shell electrocatalysts. Heterogeneous atoms on the surface can change the adsorption strength of ions [16], and provide different active site for reactions with an ensemble effect [17-19].

In this study, sub-monolayer modified Pt-shell@Pd-core nanoparticles on carbon support (Pt_x@Pd/C) with various Pt surface concentrations were prepared using a colloidal method and characterized to investigate the effect of Pt deposition on the HOR activity of Pt_x@Pd nanoparticles. Defect sites in the Pt-shell@Pd-core nanoparticles were investigated using electrochemical methods. The oxidation state of the Pd surfaces and Pt shell in the Pt-shell@Pd-core nanoparticles were examined with high resolution-X-ray photoelectron spectroscopy (HR-XPS) and

XAS, respectively. HOR activity was measured to investigate the effect of Pt shell growth on the Pd nanoparticles.

3.1.1 Crystalline structure of the Pt_x@Pd/C

Figure 3.1 shows the HR-TEM images of the catalysts. The Pt_x@Pd nanoparticles had narrow size distributions. The mean particle diameter of the catalysts (Figure 3.2) was 3.08, 3.07, 3.06, 3.19, 2.98, 2.99, and 3.02 nm for Pd/C, $Pt_{0.8\%}$@Pd/C, $Pt_{1.7\%}$@Pd/C, $Pt_{2.2\%}$@Pd/C, $Pt_{4.9\%}$@Pd/C, and $Pt_{5.7\%}$@Pd/C, respectively, and did not show any significant size change during Pt deposition.

The XRD of Pt_x@Pd/C showed little changes in XRD pattern compared to that of Pd/C suggested little changes in the crystallographic structure of Pt_x@Pd/C during Pt overlayer deposition process (Figure 3.3). The Pd/C showed superposed diffraction peaks of Pd (111) and (200) phase at the 2θ angle of 39.5 ° and 43.3 °. The diffraction angles of Pd (111) and Pd (200) in Pd/C shifted negative directions compared to those of bulk Pd crystal (PDF# 60-6174) suggesting existence of carbon or oxygen contaminations in the Pd nanoparticles [20]. The HR-TEM and XRD analysis showed that the crystalline structure of Pd nanoparticles hardly affected by Pt deposition.

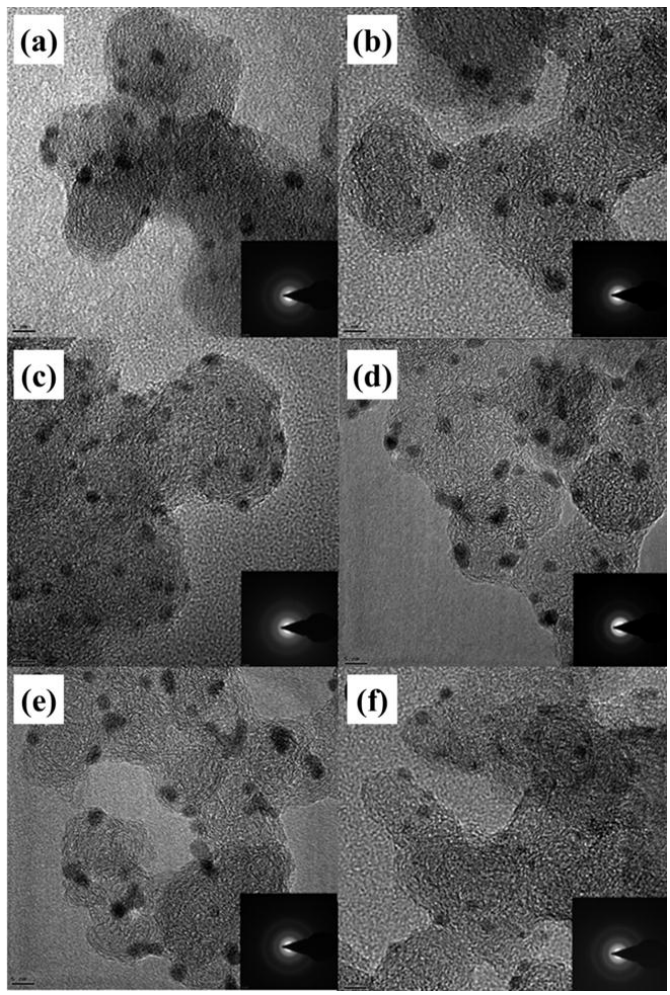

Figure 3.1 TEM image of (a) Pd/C, (b) $Pt_{0.8\%}$@Pd/C, (c) $Pt_{1.7\%}$@Pd/C, (d) $Pt_{2.2\%}$@Pd/C, (e) $Pt_{4.9\%}$@Pd/C, and (f) $Pt_{5.7\%}$@Pd/C, and SAD pattern (inset).

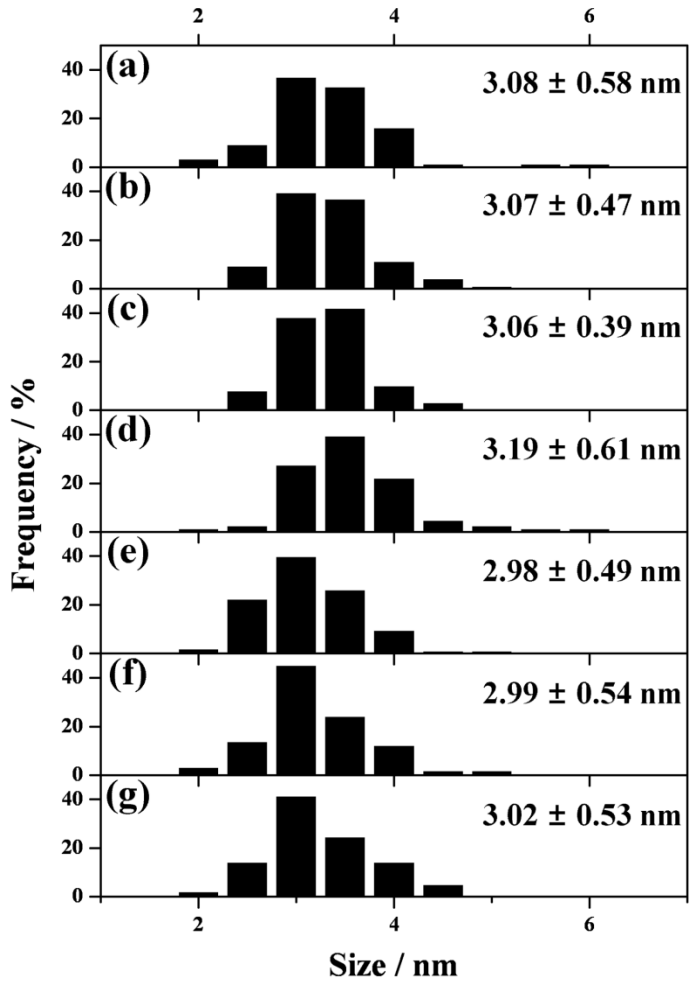

Figure 3.2 Size distribution of Pt_x@Pd nanoparticles in (a) Pd/C, (b) $Pt_{0.8\%}$@Pd/C, (c) $Pt_{1.7\%}$@Pd/C, (d) $Pt_{2.2\%}$@Pd/C, (e) $Pt_{4.9\%}$@Pd/C, and (f) $Pt_{5.7\%}$@Pd/C.

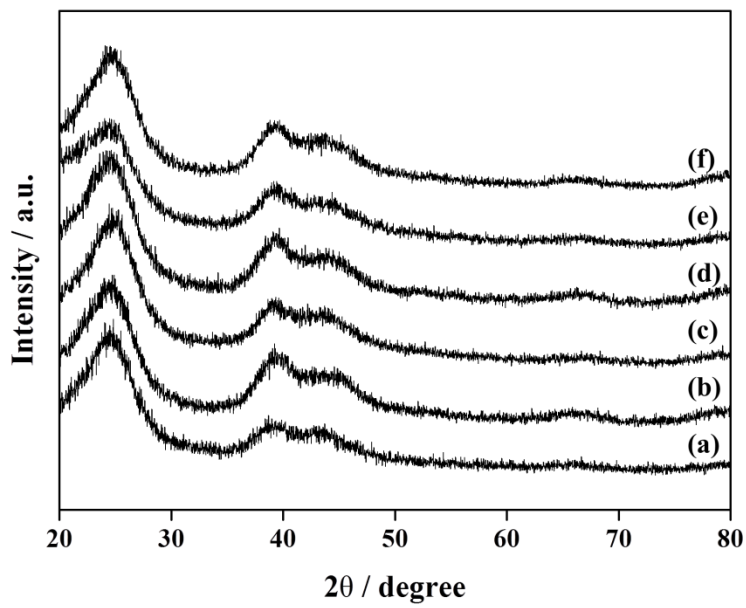

Figure 3.3 X-ray diffraction pattern of (a) Pd/C, (b) $Pt_{0.8\%}$@Pd/C, (c) $Pt_{1.7\%}$@Pd/C, (d) $Pt_{2.2\%}$@Pd/C, (e) $Pt_{4.9\%}$@Pd/C, and (f) $Pt_{5.7\%}$@Pd/C.

3.1.2 Surface structure of the Pt_x@Pd/C

Total Pt concentrations in the Pt_x@Pd nanoparticles (number of Pt atoms/number of Pd and Pt atoms) were determined using HR-XPS (Figure 3.4). HR-XPS was conducted with an 8A1 beamline in the Pohang Acceleration Laboratory (PAL). Pd and Pt binding energies were calibrated with respect to the energy of Au $4f_{7/2}$. Intensities of photoelectrons are given following the basic equation for a plane surface,

$$I = \sigma N \left[exp\left(-\frac{d}{\lambda}\right)\right]$$

where I is intensity, σ is the photoionization cross-section, N is the number of atoms, d is depth, and λ is the inelastic electron mean free path. The total photoelectrons from Pt_x@Pd nanoparticles are given by integrating individual photoelectrons from Pt or Pd atoms, and the photoelectron intensity depended on their position in the Pt_x@Pd nanoparticles. With simple assumptions (only topmost Pt sub-mono-layer and uniform spherical nanoparticles), we obtained the total photoelectron intensities from Pt or Pd in a Pt_x@Pd nanoparticle.

$$I_{total,Pt} = \int_0^R \sigma_{Pt} N_{Pt} \delta(R-r) \frac{3r^2}{R^2} exp\left(-\frac{R-r}{\lambda_{Pt}}\right) dr$$

$$I_{total,Pd} = \int_0^R \sigma_{Pd} N_{Pd} \frac{3r^2}{R^2} exp\left(-\frac{R-r}{\lambda_{Pd}}\right) dr$$

where I_{total} is total intensity of a photoelectron, σ_i is photoionization cross-section

of *i*, N_i is the number of total i atoms in a Pt_x@Pd nanoparticle, *R* is the radius of a nanoparticle, *r* is the distance from the center of the nanoparticle, and λ_i is the inelastic electron mean free path of photoelectrons from *i*.

The HR-XPS measurements were conducted with 630 eV of X-ray energy, and the work function of the analyzer was 2.5 eV. Thus, kinetic energies of photoelectrons from Pt 4f and Pd 3d were approximately 560 eV and 300 eV, respectively. Empirically, λ is directly proportional to the three-fourth power of the kinetic energy. Here, we adopted 13 Å and 7 Å for the mean free path of photoelectrons from Pt and Pd, respectively [21]. The XAS analysis was conducted in the 10A beamline (high flux XAS apparatus) at PAL. The PAL storage ring was operated at electron energy of 2.5 GeV and an electron current of 150 ~ 170 mA. All X-ray absorption spectra were taken in fluorescence mode under ambient air.

Total Pt concentrations were calculated from photoelectron intensities of Pt 4f and Pd 3d [22], and was 0.25, 0.53, 0.73, 1.62, and 1.89% for $Pt_{0.8\%}$@Pd/C, $Pt_{1.7\%}$@Pd/C, $Pt_{2.2\%}$@Pd/C, $Pt_{4.9\%}$@Pd/C, and $Pt_{5.7\%}$@Pd/C, respectively.

The Pt surface concentration (number of surface Pt atoms/number of total surface atoms in Pt_x@Pd nanoparticles) was calculated to be 0.76, 1.70, 2.17, 4.85, and 5.72% for $Pt_{0.8\%}$@Pd/C, $Pt_{1.7\%}$@Pd/C, $Pt_{2.2\%}$@Pd/C, $Pt_{4.9\%}$@Pd/C, and $Pt_{5.7\%}$@Pd/C, respectively, from the total Pt concentration and the average size of the nanoparticles (3.1 nm) with an assumption of the topmost Pt layer on uniform

spherical nanoparticles (figure 3.5).

$$\text{Surface Pt concentration} = \text{Total Pt concentration} \times \frac{3}{\pi d}$$

The effect of Pt deposition on the surface oxidation state of Pd nanoparticles was examined by analyzing the Pd 3d XPS. The atomic ratio of Pd(0) increased by 13.4 % and 23.4 % in $Pt_{0.8\%}$@Pd/C and $Pt_{1.7\%}$@Pd/C, respectively, compared to that in Pd/C (Figure 3.6). A further increase in the Pd(0) ratio was not detected at the higher Pt concentration. The decrease in Pd oxidation state in Pt_x@Pd/C seemed to be attributed to dissolution of Pd surface oxide due to galvanic displacement, as the standard reduction potential of Pt is more positive than that of Pd. The binding energies of Pd 3d hardly changed during Pt deposition, indicating that the electron transfer from Pt to Pd was negligible at Pt surface concentrations < 5.7%.

The Pt oxidation state in the Pt_x@Pd nanoparticles was investigated by Pt L_{III} XAS with a high flux XAS apparatus at the PAL (10A beam line). The XANES of Pt_x@Pd/C was presented in figure 3.7. The white line intensity ($\Delta\mu$) reflecting the oxidation state of Pt gradually increased with the increase in Pt concentration (Figrue 3.8):

$$\Delta\mu = \mu_{max} - \mu^0$$

Where, μ_{max} is maximum normalized X-ray absorbance and μ^0 is normalized absorbance of Pt L_{III} edge.

The white line intensity in the Pt L_{III} edge implied unoccupied 5d state resulting from Pt-O bond formation or electron transfer from Pt to Pd [23]. The increase in $\Delta\mu$ seemed to be attributed to the increase in the Pt-O bond, as electron transfer from Pt to Pd was negligible (Pd 3d XPS) [24, 25].

To characterize the increase in the Pt-O bond with the increase in Pt concentration, the k^3-weighted Fourier transform (FT) of the Pt L_{III} EXAFS spectra was analyzed for $Pt_{2.2\%}$@Pd/C, $Pt_{4.9\%}$@Pd/C, and $Pt_{5.7\%}$@Pd/C, which provided reliable S/N ratios in the EXAFS region. In EXAFS spectra, more Pt-O bonding was confirmed from the increased intensity of the first shell (2.05 Å) [26] with an increase in Pt concentration, which agreed with the increase in white line intensities (Figure 3.9). In addition, smaller contributions of Pt-Pt or Pt-Pd bond were observed with higher Pt concentration from the second shell intensity (2.75 Å).

The more oxidized Pt shell in the higher Pt concentrations could be understood in terms of preferred deposition of the Pt shell. Considering that Pt adatoms on the Pd nanoparticles may have preference for a more stable site, higher Pt-Pt or Pt-Pd contributions in Pt_x@Pd nanoparticles at the lower Pt concentration was reasonable, because the first Pt adatom deposited on a Pd nanoparticle may sit on the most stable site for higher coordination, i.e., step edges or kink. As the Pt concentration increased, fewer stable sites remain, which provided more Pt-Pd coordination. In

other words, the total defect site on the Pt_x@Pd nanoparticles decreased with an increase in Pt surface concentrations as the Pt shell covered the Pt surface defect sites.

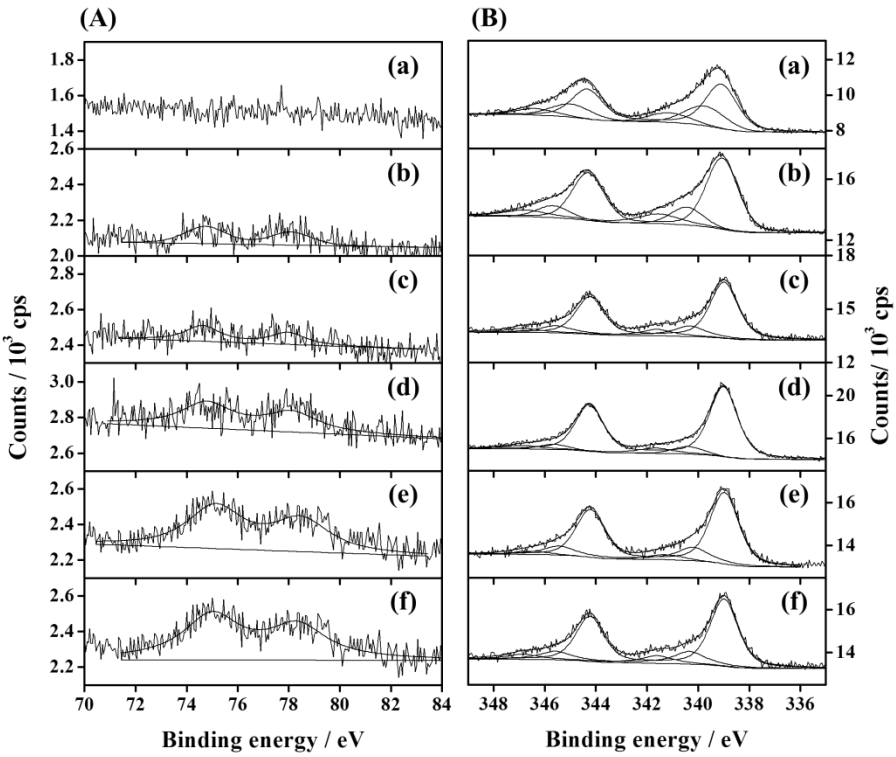

Figure 3.4 (A) Pt 4f and (B) Pd 3d XPS of (a) Pd/C, (b) $Pt_{0.8\%}$@Pd/C, (c) $Pt_{1.7\%}$@Pd/C, (d) $Pt_{2.2\%}$@Pd/C, (e) $Pt_{4.9\%}$@Pd/C, and (f) $Pt_{5.7\%}$@Pd/C.

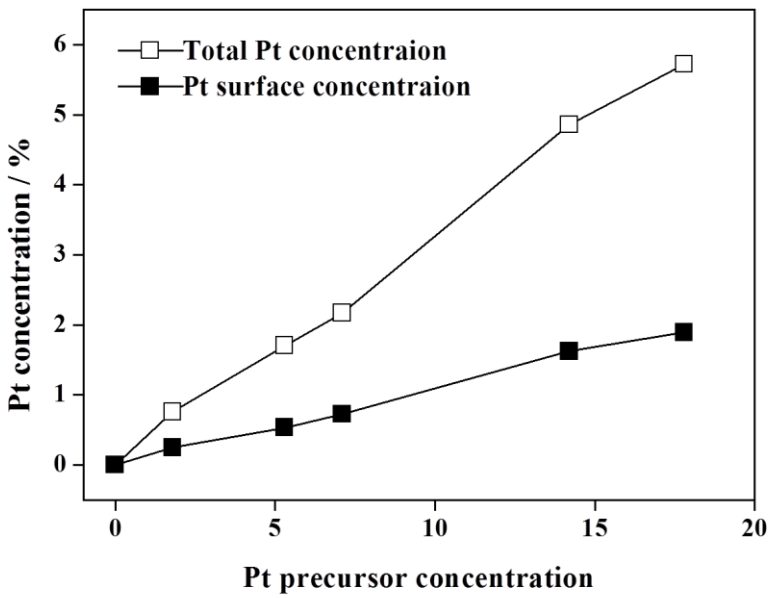

Figure 3.5 Total Pt concentrations (■) and Pt surface concentration (□) of Pd and Pt_x@Pd nanoparticles.

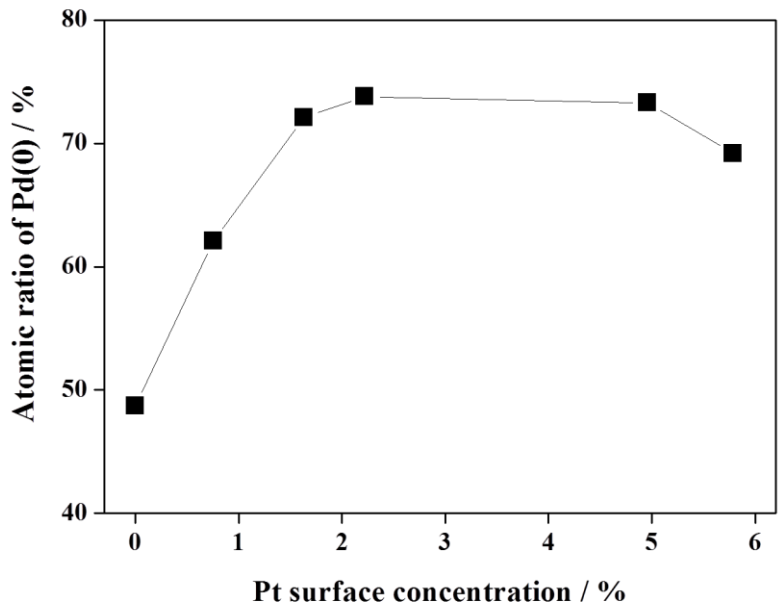

Figure 3.6 Atomic ratio of $Pd(0)/Pd_{total}$ calculated from Pd 3d XPS.

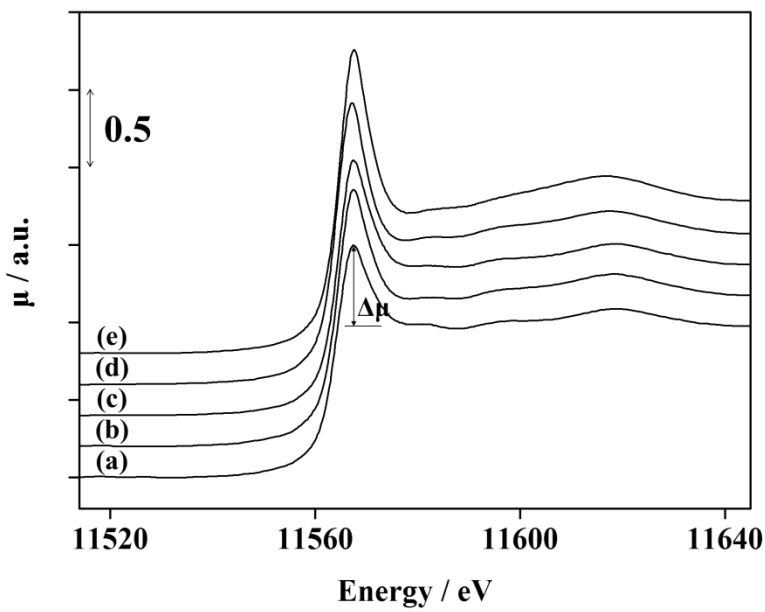

Figure 3.7 XANES spectra of (a) Pd/C, (b) $Pt_{0.8\%}$@Pd/C, (c) $Pt_{1.7\%}$@Pd/C, (d) $Pt_{2.2\%}$@Pd/C, (e) $Pt_{4.9\%}$@Pd/C, and (f) $Pt_{5.7\%}$@Pd/C.

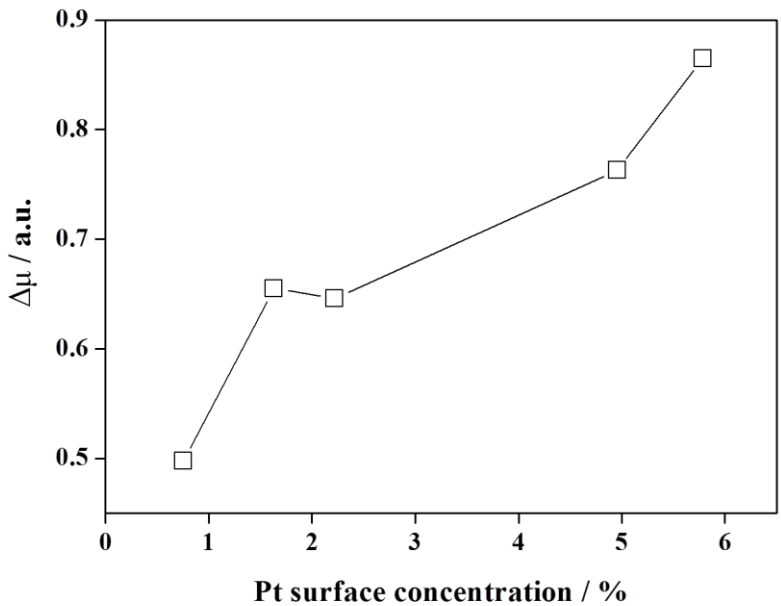

Figure 3.8 Δμ determined from the XANES spectra of Pt L_{III}.

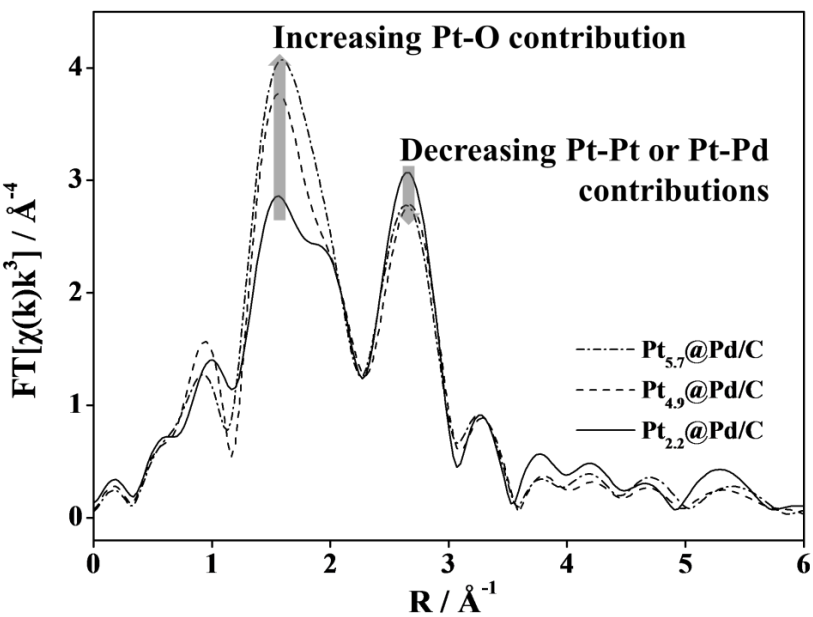

Figure 3.9 Radial distribution function of FT of k^3-weighted Pt L_{III} EXAFS spectra in $Pt_{2.2\%}$@Pd/C (——), $Pt_{4.9\%}$@Pd/C (– – –), and (f) $Pt_{5.7\%}$@Pd/C (– • –).

3.1.3 Electrochemical characterization

Electrochemical measurements were conducted in a temperature-controlled electrolyte with a saturated calomel reference electrode. All experiments were conducted nonisothermally. Reference electrode temperature was kept constant (25 ℃), whereas the temperature of the working electrode was varied from 2 to 18 ℃. The reference electrode was separated from the working electrode compartment by an electrolyte bridge with a proton membrane connector to avoid chloride contamination. The reference electrode potential was corrected with respect to the reversible hydrogen electrode (RHE) using a homemade RHE before measurement. A catalyst-coated glassy carbon (GC, 0.196 cm^{-2}) substrate was used as the working electrode. Catalyst ink was made of Pt_x@Pd/C catalyst, 5 wt% Nafion® solution, and 2-propanol. The catalyst ink (5 μL) was dropped onto the GC substrate and dried at 70 ℃ to prevent detaching of the catalyst during measurement.

Cyclic voltammogram (CV) were taken in an Ar saturated 0.1 M $HClO_4$ solution with a scan rate of 50 mV s^{-1} at 20 ℃. Before the CV measurements, potential cycling from 0 V to 0.4 V was repeated until the voltammogram was stable. Electrooxidation of irreversibly adsorbed CO (so-called CO stripping voltammetry) was conducted in the same electrolyte with the CV measurement. For

CO adsorption, the electrolyte was purged with 100 % CO at the electrode potential of 50 mV for 20 min followed by Ar purging for 30 min to remove CO from the electrolyte. The CO was oxidized with CV in the potential range of 0.05 ~ 1.1 V and a scan rate of 20 mV s^{-1}. HOR polarization was examined under hydrogen saturated 0.1 M $HClO_4$ at 2 ~ 18℃ with a RDE rotation speed of 1600 rpm and a scan rate of 5 mV s^{-1}. Our catalysts contained ~5 wt% metal nanoparticles to avoid high rotation speed, which can evoke turbulent flow [27].

To investigate adsorption strength of hydrogen, CO adsorption strength was characterized with CO stripping voltammetry, as the CO bond strength has a positive relationship with hydrogen bond strength. In CO stripping voltammetry (Figure 3.10), the peak potential of CO electrooxidation (E_p) in Pt_x@Pd/C shifted positive with an increase in Pt concentrations (from 972 mV to 952 mV for $Pd_{0.8\%}$@/C and $Pt_{5.7\%}$Pd@/C). The positive shift in E_p indicates weaker CO adsorption with higher Pt concentrations and Pt shell formation on Pd nanoparticles [28, 29]. The decrease in the ratio between the main peak (i_p) and the tail of the oxidation current at 1.05 V ($i_{1.05}$) also suggested weaker CO adsorption with higher Pt concentration (Figure. 3.11). The tail of the CO stripping voltammetry represents electrooxidation of strongly adsorbed CO, as the electrooxidation rate of CO at a high overpotential region is (>E_P) governed by the diffusion rate of the adsorbed CO on the electrode surface [30-33]. Thus, a positive shift of E_P and depression of

tails in the CO stripping voltammetry suggests a decrease in strongly adsorbed CO on the Pt_x@Pd nanoparticles and, therefore, a decrease in adsorption energy of hydrogen with the increase in Pt surface concentration.

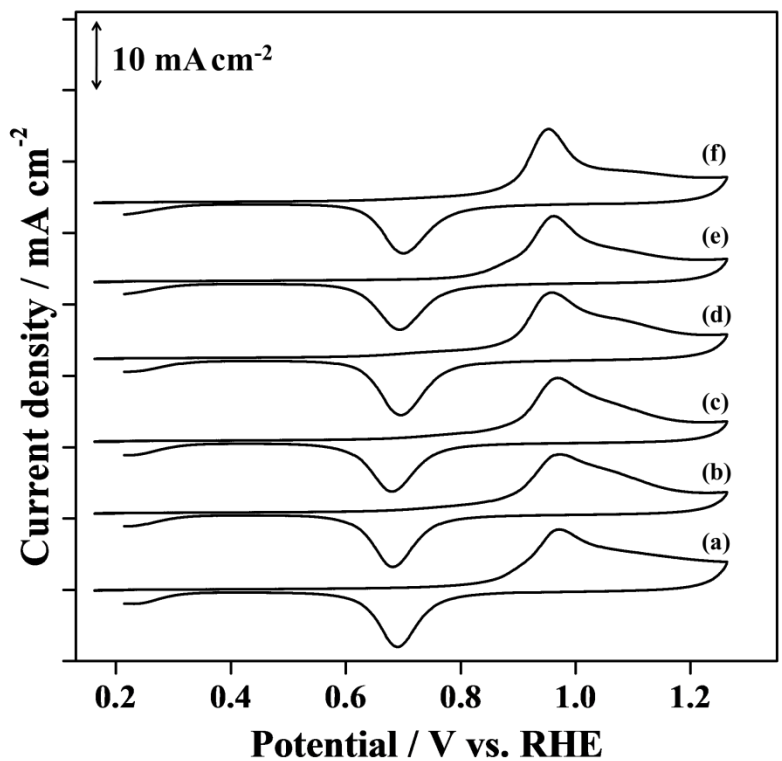

Figure 3.10 CO stripping voltammogram of (a) Pd/C, (b) $Pt_{0.8\%}$@Pd/C, (c) $Pt_{1.7\%}$@Pd/C, (d) $Pt_{2.2\%}$@Pd/C, (e) $Pt_{4.9\%}$@Pd/C, and (f) $Pt_{5.7\%}$@Pd/C.

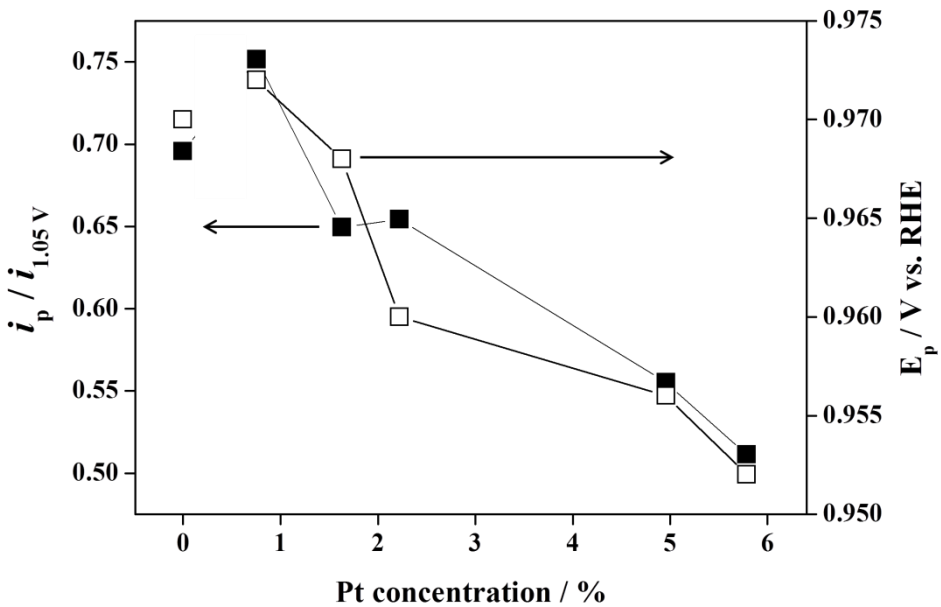

Figure 3.11 CO electrooxidation current density ratio ($i_p/i_{1.05}$) (■) and peak potential of CO stripping voltammogram (□).

3.1.4 HOR activity

HOR polarization on Pt_x@Pd/C was examined using a RDE in 0.1 M $HClO_4$ to investigate the effect of Pt deposition on the Pd nanoparticles. The exchange current density (i_0) (Figure 3.12) was calculated with the following relationship using potential-current profiles of the "micropolarization region" [34]:

$$i = i_0(\eta F/RT)$$

where i is measured current density and η is overpotential (~10 mV).

Compared to i_0 of Pd/C (0.56 mA cm^{-2}), that of Pt_x@Pd/C was increased 3.5 times to achieve 1.96 mA cm^{-2} ($Pt_{4.9\%}$@Pd/C), which was comparable to reported i_0 values of Pt surfaces [34-37]. As the surface Pt concentration of 4.9 % corresponded to the total concentration of 1.6 %, it can be concluded that we achieved comparable enhancement of HOR activity with 1/3 the Pt consumption compared to our previous Pt-Pd alloy nanoparticles and demonstrating 3.4-fold increase in HOR activity with total Pt concentrations of 5% [38].

To investigate the reaction mechanism of HOR on Pt_x@Pd surfaces, apparent enthalpy ($\Delta H^{0\#}$) was determined by plotting Arrhenius plots (i_0 vs. 1/T) (Figure 3.13).

$$\frac{d(\log i_0)}{d(\frac{1}{T})} = -\frac{\Delta H^{o\#}}{2.3R}$$

With the higher Pt concentration, the calculated $\Delta H^{0\#}$ initially decreased

significantly from 99 kJ/mol (Pd/C) to 55.2 kJ/mol ($Pt_{1.7\%}$@Pd/C), but became virtually constant with a Pt surface concentration > 1.7% (Figure 3.14). As the $\Delta H^{0\#}$ represents activation energy of RDS, the Pt_x@Pd/C HOR mechanism can be investigated with variations in Pt surface concentration.

Rau et al. reported the kinetic parameter analysis of HOR on Pd thin film and showed that the Tafel–Volmer pathway is dominant in the low overpotential region (~40 mV) [39]. The Tafel reaction involves dissociative adsorption of molecular hydrogen and the Volmer reaction involves desorption of hydrogen atom. The Volmer reaction was RDS on the Pd surface, as the Volmer reaction rate on Pd ($\upsilon^V = 1.66 \times 10^{-7}$ mol cm^{-2} s^{-1}) was slower than Tafel reaction rate on Pd ($\upsilon^T = 2.26 \times 10^{-7}$ mol cm^{-2} s^{-1}). Ignoring the effect of the interactions between Pt and Pd atoms on the υ^V in the Pt_x@Pd nanoparticles, the $\upsilon^V_{Ptx@Pd}$ could be expressed as the sum of υ^V on the Pt (υ^V_{Pt}) and Pd (υ^V_{Pd}) surfaces.

$$\upsilon^V_{Ptx@Pd} = x \cdot \upsilon^V_{Pt} + (1-x/100)\upsilon^V_{Pd}$$

where $\upsilon^V_{Ptx@Pd}$ is the Volmer reaction rate on Pt_x@Pd nanoparticle surfaces and x is the Pt surface concentration. As the υ^V_{Pt} (6.06×10^{-6} mol cm^{-2} s^{-1}) was ~37 times higher than that on Pd [40], increasing the Pt surface concentration should increase the $\upsilon^V_{Ptx@Pd}$. The $\upsilon^V_{Ptx@Pd}$ on $Pt_{1.7\%}$Pd/C was calculated to be 2.66×10^{-7} mol cm^{-2} s^{-1} and was higher than υ^T on the Pd surface (2.26×10^{-7} mol cm^{-2} s^{-1}) by 18%, whereas the $\upsilon^V_{Ptx@Pd}$ on $Pt_{0.8\%}$@Pd/C (2.1×10^{-7} mol cm^{-2} s^{-1}) was lower than υ^T_{Pd}.

This suggested that the RDS of HOR on Pd/C and $Pt_{0.8\%}$@Pd/C was the Volmer reaction, whereas that on $Pt_{1.7\%}$@Pd/C ~ $Pt_{5.7\%}$@Pd/C was the Tafel reaction. As the weaker hydrogen adsorption lead to a faster Volmer reaction, the $\Delta H^{0\#}$ on Pt_x@Pd/C at x<1.7 % decreased with an increase in Pt surface concentrations.

In $Pt_{1.7\%}$@Pd/C–$Pt_{5.7\%}$@Pd/C, RDS of HOR was Tafel reaction and it seemed to have little relationship with Pt shell growth. We speculated that the ensemble effect hindered the increase in the Tafel reaction rate on Pt_x@Pd surfaces. Unlike the hydrogen desorption reaction (Volmer reaction), the dissociative adsorption of hydrogen (Tafel reaction) requires more than three neighboring atoms (ensemble effect) [41]. Thus, the increase in the Tafel reaction rate may be significantly slower than the increase in the Volmer reaction rate. Thus, the slow increase in the Tafel reaction rate may lead to similar $\Delta H^{0\#}$ with Pt surface concentrations of 1.7 ~ 5.7 %.

The $\Delta H^{0\#}$ changes due to Pt shell growth suggested that the Pt shell deposition changed the RDS of HOR on the electrocatalyst surface. The turning point, surface Pt concentration changing the RDS, can be significantly low (~2 %) and highly active Pt-shell/Pd-core electrocatalyst could be achieved with 1/3 of Pt concentration compared to the Pd-Pt alloy electrocatalyst.

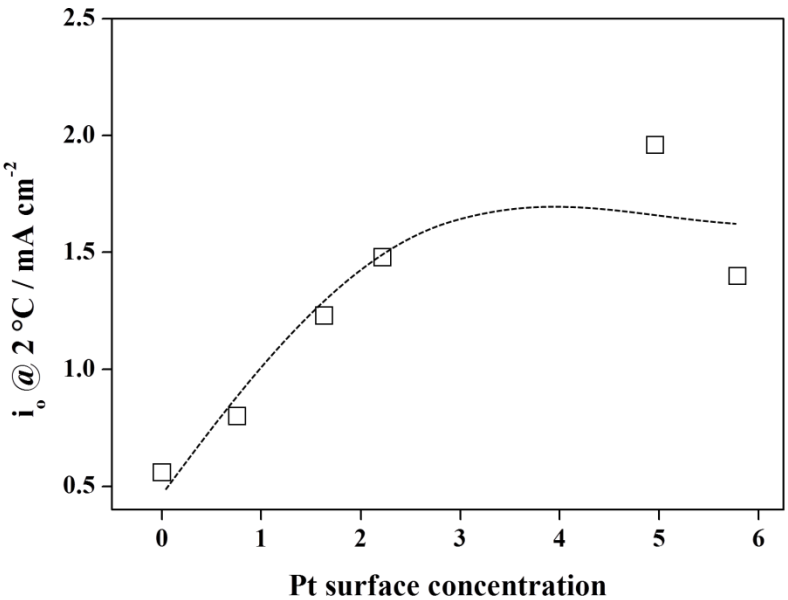

Figure 3.12 Exchange current density (i_0) of HOR on Pd/C and Pt_xPd/C at 2 ℃.

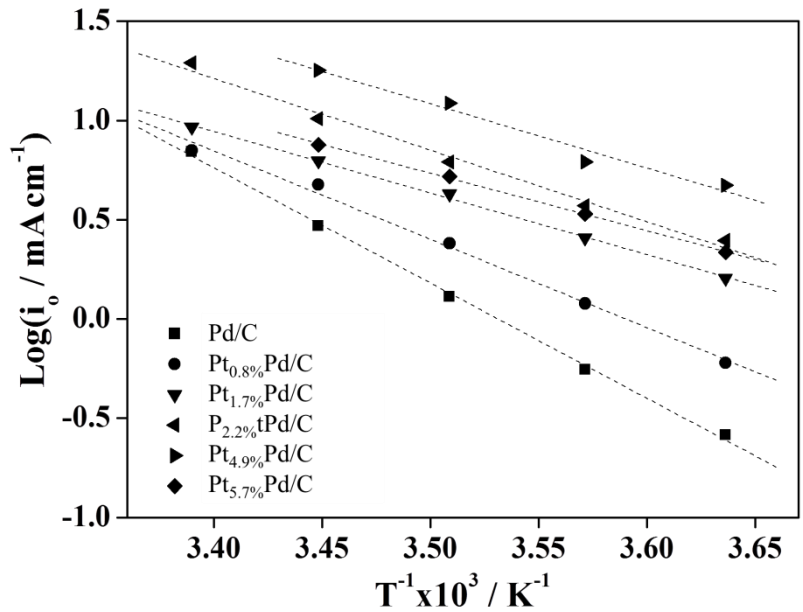

Figure 3.13 Arrhenius plot of HOR on Pd/C and Pt_x@Pd/C electrocatalysts.

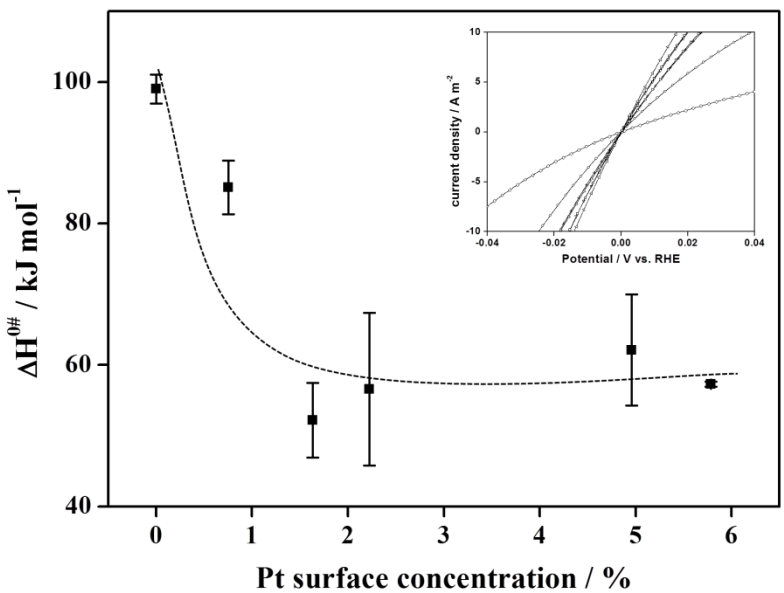

Figure 3.14 Apparent enthalpy ($\Delta H^{0\#}$) of HOR on Pd/C and Pt_x@Pd/C electrocatalysts; HOR polarization of Pd/C and Pt_x@Pd/C at micropolarizaion region (inset)

3.2 CO induced Pt segregation in PtAu alloy nanoparticles

Due to the excellent intrinsic stability of Au [42], several studies have developed and analyzed Pt-Au electrocatalysts, such as PtAu alloy or Pt thin films on Au substrate, for fuel cell applications, including the oxygen reduction reaction (ORR) [43-45], formic acid oxidation [46-50], and methanol oxidation [48-51]. Pt-Au nanoparticles often showed enhanced ORR compared with Pt nanoparticles with weaker OH adsorption due to the contraction strain effect [52-58], while, in bulk material, Pt-Au has lower activity due to the lattice mismatch between Pt and Au (4.1%) [59, 60]. However, ORR activity on PtAu alloy nanoparticles are lower than that on PtTM nanoparticles and improving the ORR activity of PtAu nanoparticles is still of significant importance. There are two different ways to increase the ORR activity of PtAu nanoparticles. One is to reduce the OH adsorption energy by modifying the electronic structure of PtAu nanoparticles, where the OH adsorption is stronger than optimum [61]. Another is to increase the number of active sites for ORR by controlling the surface composition.

CO induced surface segregation is an attractive strategy to improve the ORR activity of PtAu alloy nanoparticles, since the electronic structure and surface composition can be simultaneously modified. CO induced segregation was

predicted by Greeley et al. via computational simulations for various combinations of metals [62]. To the best of my knowledge, there has only been one report that examined the relationship between CO induced surface segregation during thermal treatment and ORR activity. Mayrhofer et al. reported that thermal CO annealing could improve ORR mass activity of Pt-Co/C by a factor of ~3 when compared with untreated Pt-Co nanoparticles in alkaline media, but the specific activity and surface property changes during CO annealing was not examined [63]. Investigating qualitatively the changes of surface properties and ORR activity of PtAu nanoparticles during CO exposure will allow us to better understand the effect of surface comsption on the ORR activity and could help improve the ORR activity of Pt alloy nanoparticles. Core-shell structured Au-Pt nanoparticles with a Pt monolayer are the most efficient way to achieve 100% utilization and strong electronic modification of Pt, but have been prepared using an electrochemical method, which is not suitable for mass production. Thus, CO induced segregation could provide a practical way to increase Pt utilization and the specific activity of PtAu alloy nanoparticles. Therefore, improving our understanding of PtAu nanoparticle surfaces during CO induced Pt enrichment is expected to help overcoming the technical barriers; the sluggish ORR activity on Pt and instability of PtTM catalysts.

Here, we demonstrated enrichment of surface Pt concentrations in PtAu

nanoparticles under a CO atmosphere, which enhanced the ORR activity. Pt enrichment and ORR activity was characterized by XPS and electrochemical techniques. In addition, comparison of surface Pt concentration and activity changes of PtAu nanoparticles during CO induced segregation allowed us to investigate the relationship between surface properties, surface atomic composition and OH adsorption strength, and ORR activity with little changes in total atomic composition, crystalline structure, and size of PtAu nanoparticles.

3.2.1 Crystalline structure of PtAu/C

Figure 3.15 shows a schematic of surface enrichment during CO or Ar exposure. A Pt rich surface could be achieved under a CO atmosphere since the CO adsorption energy is much higher for Pt (-1.35 eV) compared to the Au (-0.35eV) [55, 62, 64, 65], while Au segregation is favored under an Ar atmosphere due to the lower surface free-energy of Au (1.41 J m^{-2}) than that of Pt (2.34 J m^{-2}) [66].

The particle size of the PtAu nanoparticles was investigated using TEM and XRD. TEM images were taken using a JEM-2010 (JEOL Ltd.) microscope at an acceleration voltage of 200 kV. The PtAu alloy nanoparticles have uniform sized and little aggregations (figure 3.16). The average size of the nanoparticles from TEM were 1.86 ± 0.31 nm, 2.00 ± 0.21 nm, and 1.96 ± 0.29 nm for PtAu-AP, PtAu-CO, and PtAu-Ar, respectively (Figure 3.17). Little aggregation or crystalline

growth (~7.5%) of the nanoparticles was observed after heat-treatment.

The XRD patterns of the PtAu/C catalysts are presented in Figure 3.18 (Pt/C and Au/C were presented as a comparison). The XRD patterns were collected using a D-MAX2500 diffractometer (Rigaku Corp., The Woodlands, TX, USA) at a gun power of 8 kW and a scan rate of 0.2 ° min^{-1}.

The XRD peak of PtAu nanoparticles suggested that the nanoparticles had typical fcc structure. The lattice constants of the PtAu nanoparticles (PtAu-AP : 3.99 Å , PtAu-CO: 4.00 Å , PtAu-Ar: 4.01 Å) were very similar to that of PtAu alloy (4.00), which was calculated by Vegard's law using the lattice constants of Au (4.10 Å) and Pt (3.91 Å) nanoparticles. As shown in Figure 3.19a, the binding energy of Pt 4f in the PtAu nanoparticles (70.7 eV) shifted to negative values when compared with Pt/C (71.4 eV). PtAu nanoparticles showed a lower binding energy of Au 4f (83.6 eV) when compared with that of Au/C (84.2 eV). (Figure 3.19b) This observed binding energy shift was in good agreement with previous reports, and suggested that our catalysts were alloy nanoparticles [67, 68].

The crystalline sizes of PtAu nanoparticles determined using the line broadening of (220) peak were 2.2 nm, 2.4 nm, and 2.2 nm for PtAu-AP, PtAu-CO, and PtAu-Ar respectively, which was in good agreement with the TEM analysis. The crystalline structure of the PtAu nanoparticles hardly changed during heat treatment, as the surface segregation is expected to occur near few layers of surface.

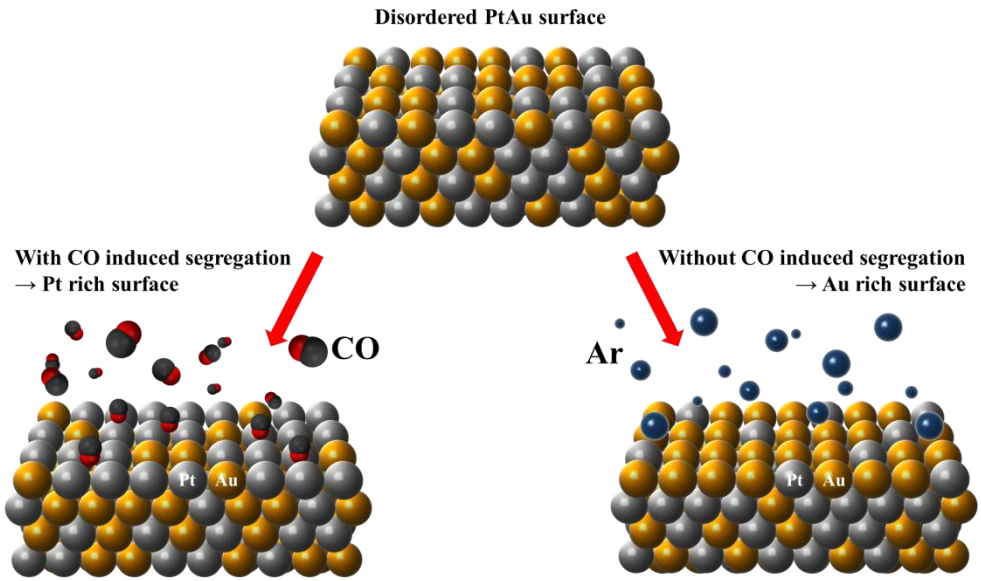

Figure 3.15 Schematic representation of surface segregation process with (left) and without (right) CO induced segregation.

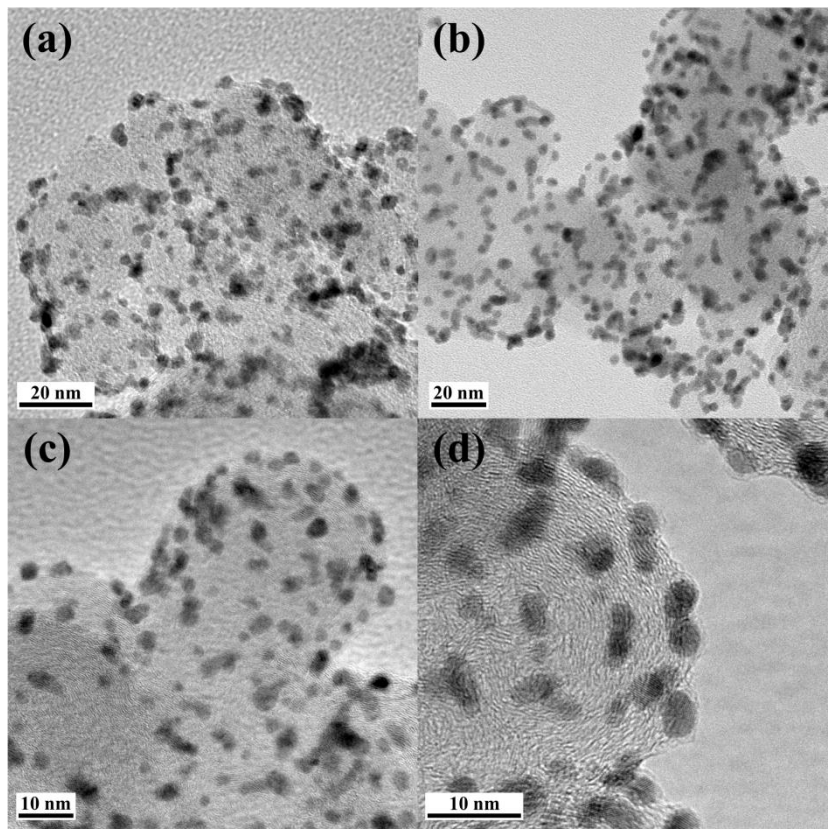

Figure 3.16 TEM image of (a) PtAu-AP, (b) PtAu-Ar, (c) PtAu-CO, and (d) a magnified image of PtAu-CO.

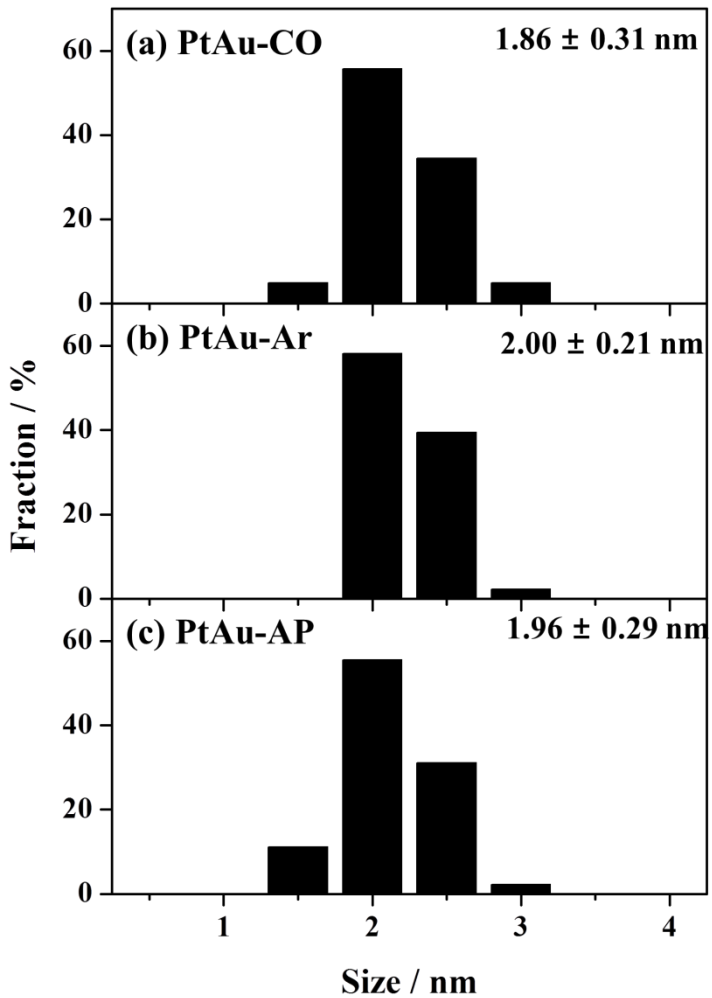

Figure 3.17 Size distributions of PtAu nanoparticles in (a) PtAu-CO, (b) PtAu-Ar, and (c) PtAu-AP.

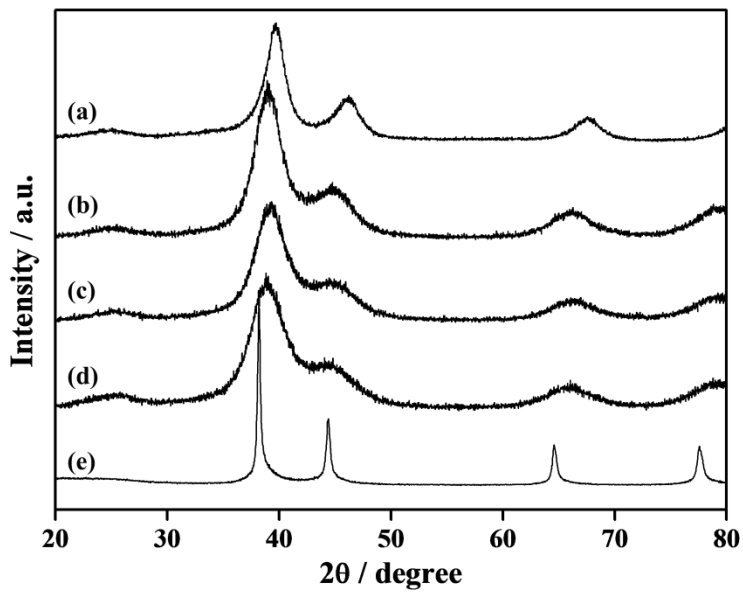

Figure 3.18 XRD of (a) Pt/C, (b) PtAu-CO, (c) PtAu-Ar, (d) PtAu-AP and (e) Au/C.

3.2.2 Surface structure of PtAu/C

In order to determine the bulk and surface composition of PtAu/C catalysts, XPS analysis was performed with a Theta Probe (Thermo Electron Corp., Waltham, MA, USA) at the Korea Basic Science Institute. The bulk composition of PtAu nanoparticles were determined from the intensity ratio of Pt 4f and Au 4f XPS (Figure 3.19), since the mean free path of the photoelectron is >20 Å with high kinetic energies (>1000 eV) [21]. The XPS intensity ratios of Pt and Au were obtained from the average of 5 different samplings of a catalyst to confirm that the compositions of the catalysts were uniform. The bulk fraction of Pt (# of Pt atoms / # of Pt and Au atoms in PtAu nanoparticles) was 55.1 ± 0.5 % in PtAu-AP. The higher Pt atomic fraction of PtAu-AP than that of precursor solution (0.128 mmol for Pt and Au) likely originated from the higher Pt fraction near the surface region [69, 70]. The bulk atomic fraction of Pt hardly changed during heat treatment under the Ar (55.2 ± 0.5%) or CO (55.2 ± 0.3%) atmosphere.

The surface atomic fraction of Pt to total metal was determined from the XPS intensity of Pt $4p_{3/2}$ and Au $4P_{3/2}$ (Figure 3.20) correction of the photoelectron cross section [67, 71]. The mean free path of the photoelectrons Pt $4p_{3/2}$ and Au $4p_{3/2}$ were approximately 14 Å [21, 72]. The surface atomic fraction of Pt calculated from the XPS intensity ratio of Pt $4p_{3/2}$ and Au $4p_{3/2}$ was 74 ± 2 %, which corresponded to 1.12 times that of the PtAu-AP (66 ± 2 %), whereas the

surface atomic fraction of Pt in the PtAu-Ar was only 50 ± 1 % (Figure 3.21).

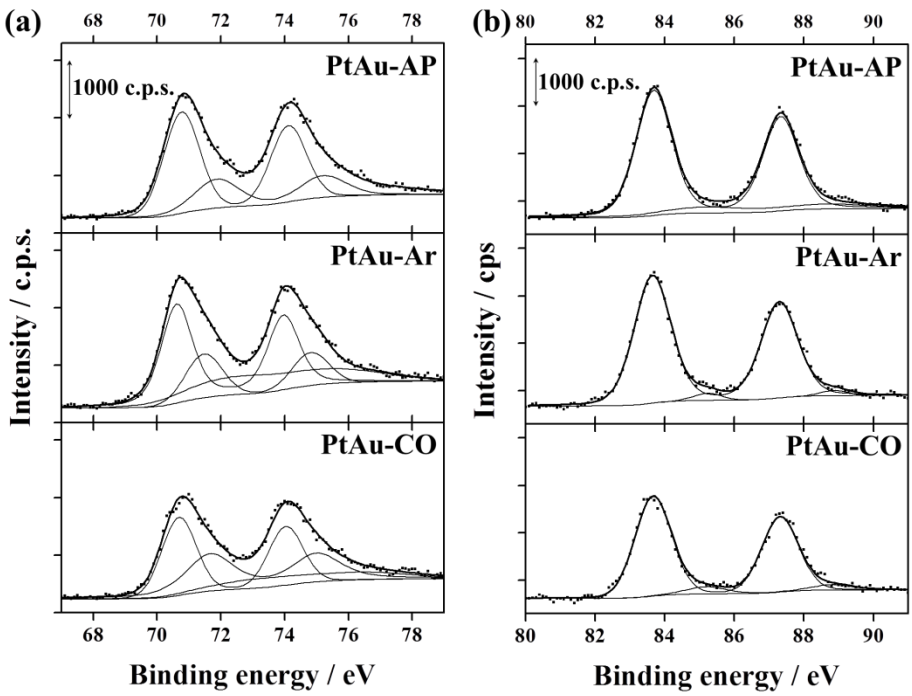

Figure 3.19 XPS of (a) Pt 4f (A) and (b) Au 4f of the PtAu/C catalysts.

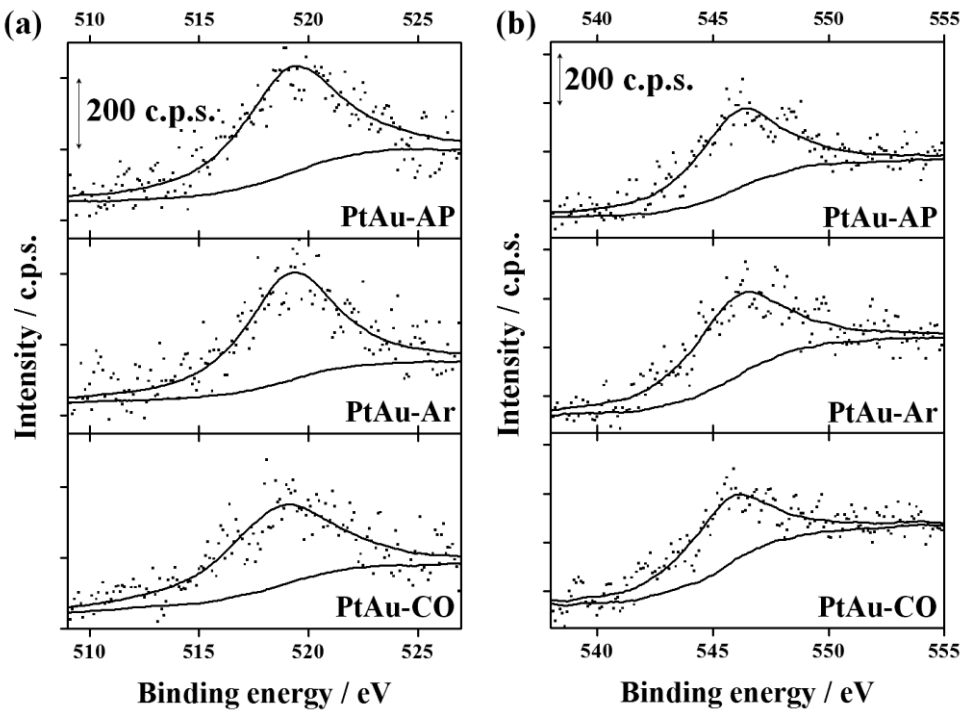

Figure 3.20 XPS of (a) Pt $4p_{3/2}$ and (b) Au $4p_{3/2}$ of the PtAu/C catalysts.

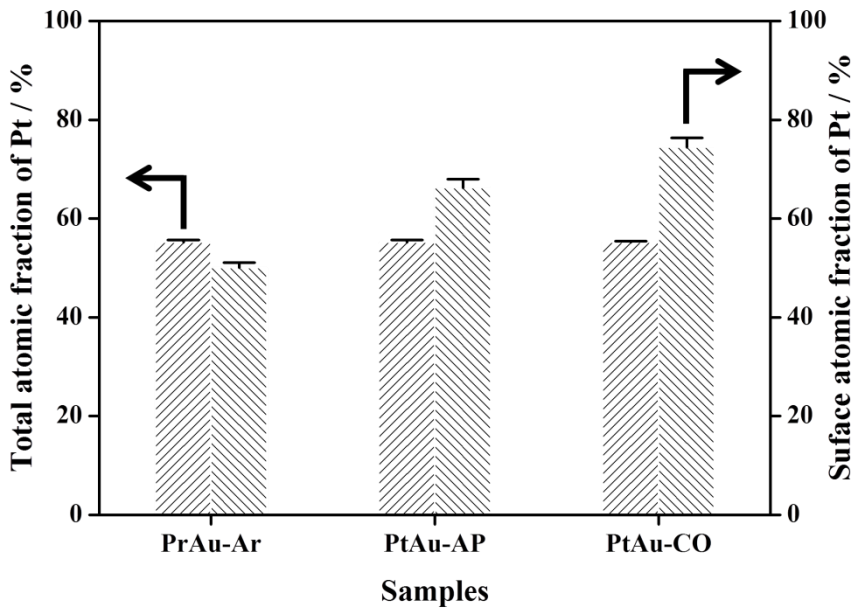

Figure 3.21 Total (left) and surface (right) atomic fraction of Pt determined by intensities of X-ray photoelectron spectra in the 4f and $4p_{3/2}$ regions, respectively.

3.2.3 Electrochemical characterization

Electrochemical measurements were conducted in a standard three-compartment electrochemical cell using a rotating disk electrode system (Eco Chemie BV). A catalyst-coated glassy carbon (GC, 5 mm diameter) substrate, GC rod, and saturated calomel electrodes were used as working, counter, and reference electrodes, respectively. However, all potentials were calibrated using a homemade reversible hydrogen electrode (RHE) and reported with respect to the RHE. The reference was separated from the working electrode compartment by an electrolyte bridge to avoid chloride contamination. Ar-purged 0.1 M $HClO_4$ was used for all electrochemical measurements, except for the ORR polarization measurements. Cyclic voltammetry was conducted at a scan rate of 20 mV s^{-1}. Before the CV measurement, potential cycling in the range from 0 V to 0.4 V was performed to obtain a stable voltammogram. The cyclic voltammograms were reproducible with a deviation in the hydrogen desorption charge density of ~3 %. ORR polarization was obtained in a O_2 saturated 0.1 M $HClO_4$ solution at a rotating rate of 1600 rpm and a scan rate of 5 mV s^{-1} [73]. All electrochemical measurements were conducted isothermally at 20 ± 0.5℃.

The surface fraction of Pt was electrochemically characterized by comparing the ratio between electrochemical surface area (ECA) of Pt and Au deduced from the hydrogen desorption on Pt ($Q_{H,Pt}$) and reduction charge of Au

surface oxide ($Q_{OH,Au}$), respectively. The electrochemical surface area of Au (ECA_{Au}) was determined from the CV of the catalysts between 0.05 V ~ 1.50 V (Figure 3.22a). This was used because Au has a characteristic reduction peak at ca. 1.3 V with a charge density of 400 μC cm^{-2}. The ECA_{Au} decreased by 18.3 % during CO exposure (PtAu-AP: 17.5 m^2 g_{Au}^{-1}, PtAu-CO: 14.3 m^2 g_{Au}^{-1}), but Ar treatment led to a 58.9 % (27.8 m^2 g_{Au}^{-1}) increase in ECA_{Au}. Since the CV measurement at >1.3 V could result in irreversible oxidation of Pt, the $Q_{H,Pt}$ was obtained from another CV measurement with an anodic limit of 1.15 V (Figure 3.22b). The ECA_{Pt} of PtAu-AP, PtAu-CO, and PtAu-Ar were 33.0 m^2 g_{Pt}^{-1}, 38.2 m^2 g_{Pt}^{-1}, and 31.5 m^2 g_{Pt}^{-1}, respectively, based on the hydrogen desorption charge density on polycrystalline Pt (210 μC cm^{-2}). From the ECA_{Pt} and ECA_{Au}, the surface Pt fraction of PtAu-AP was determined to be 65.3 %. The surface Pt fraction of PtAu-CO was 1.11 times higher (72.8 %) than that of PtAu-AP, whereas the surface Pt fraction of PtAu-Ar was 53.1 %. (Figure 3.23) The surface Pt fractions form the ECA ratio were in good agreement with the results obtained from the XPS analysis, which indicated surface enrichment of Pt in the PtAu nanoparticles.

As shown in the ORR polarization curves (Figure 3.24), the half wave potential ($E_{1/2}$) of PtAu-CO (903 mV) was more positive compared to the PtAu-AP (887 mV), demonstrating that the ORR activity was enhanced by the CO induced

Pt segregation. When the ECA was increased from 33.0 $m^2\ g_{Pt}^{-1}$ (PtAu-AP) to 38.2 $m^2\ g_{Pt}^{-1}$ (PtAu-CO), the $E_{1/2}$ shift with a larger active Pt area was estimated to be +4.0 mV according to the relationship between ECA and $E_{1/2}$ suggested by Adzic et al [74]. However, in this study, the experimental $E_{1/2}$ shift was as large as +16 mV, suggesting that the turnover frequency, current density normalized with respect to the ECA_{Pt} in electrocatalysis, was also enhanced, as well as the ECA, through the heat-treatment under the CO condition.

From the polarization data, the mass activity was calculated to be 18.9 A g_{Pt}^{-1} (PtAu-AP), 33.2 A g_{Pt}^{-1} (PtAu-CO), and 11.4 A g_{Pt}^{-1} (PtAu-Ar), by using the Koutecky-Levich equation:

$$1/i = 1/i_k + 1/i_{dl}$$

where i is the measured current, i_k is measured kinetic current, and i_{dl} is diffusion limiting current [75]. The specific activity was determined by dividing i_k by the ECA_{Pt} values. As shown in Figure 3.25, the specific activity of PtAu-CO (1.74 mA cm_{Pt}^{-2}) was 1.53 times higher than that of PtAu-AP (1.14 mA cm_{Pt}^{-2}), which was expected based on the large shift in the polarization curves. Since the ORR reaction on the Pt-Au alloy is limited by the desorption step of intermediate OH [7, 76, 77], it seems that the adsorption energy of OH decreased as a result of CO induced surface modification.

To experimentally validate the change in OH adsorption energy, the

potential of total zero charge (PZTC) values were measured for each sample using the CO-displacement technique, which was suggested by Orts et al [78]. Briefly, CO was adsorbed onto the electrode at 0.104 V where the specially adsorbed hydrogen is the dominant ion species and desorption charge due to the adsorption of CO was recorded (Figure 3.26). The PZTC was calculated from the charge contribution of hydrogen desorption, which were displaced by CO [78, 79]. As stated in the Experimental, the potential having an identical charge density, PZTC, form CO-displacement and integration of cyclic voltammogram was determined. The cationic contribution of surface charge could be calculated from the CV measurement, since the underpotentially deposited hydrogen is the dominant cationic species in the potential range of CO-displacement. The anionic contribution to the surface charge could be determined by subtracting the total surface charge collected during CO adsorption from the cationic surface charge, $Q_{H,Pt}$ above the CO adsorption potential (0.104 V).

Even though there exist hindrance by specific adsorption, Gomez et al. found that the PZTC is linearly related to the work function level, which is directly connected to the adsorption strength of ions [80]. Thus, the PZTC by CO-displacement technique has been widely utilized to investigate adsorption energy of ions [80-86]. The experimental PZTC values were more positive for PtAu-CO (221 mV) when compared to the PtAu-AP (209 mV), which clearly demonstrates that

the OH adsorption became much weaker through the CO induced Pt segregation (Figure 3.25). The specific activity enhancement of 53% with a PZTC increase of 12 mV seems to be reasonable, while the activity was reported to increase be a factor of 5 with a 35 mV PZTC variation when the Pt nanoparticle size was increased (1 nm → 30 nm) [87]. Therefore, it can be summarized that the increased surface Pt fraction (65.3 % → 72.8 %) by CO heat treatment led to weaker OH adsorption, enhancing overall ORR activity, which is in consistent with the Pedersen et al.'s report, weaker OH adsorption energy with higher Pt fraction, for the PtAu monolayer on Pt(111) or Au(111) with various surface Pt fractions between 40% and 100 % [88].

The comparison of the surface Pt concentration and ORR activity of PtAu nanoparticles during CO induced segregation allowed us to evaluate the enhanced ORR activity on PtAu alloy nanoparticles. The enhanced ORR activity was attributed to enrichment of surface Pt, which led to weaker OH adsorption as well as a higher Pt surface area. Since the properties and optimum structure of surface alloys have been well established through computational simulations, this strategy (CO induced segregation) could be expended to other Pt alloy surfaces to improve ORR activity. This finding suggests that CO induced surface segregation could be used to enhance the catalytic activity of the carbon-supported alloy nanoparticles without changing the total composition.

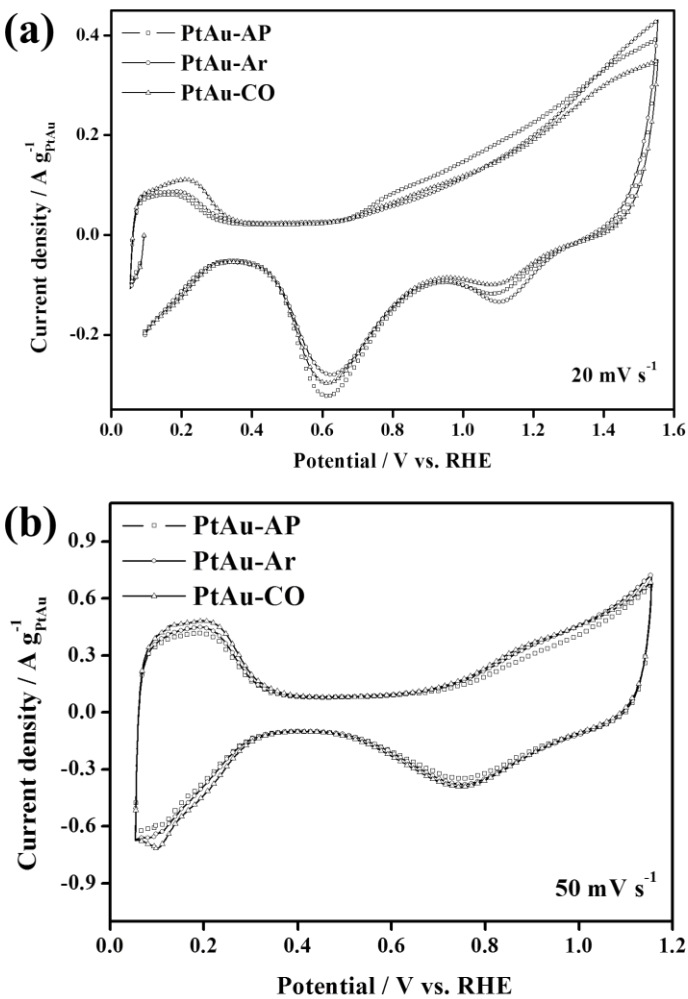

Figure 3.22 Cyclic voltammogram in the potential range of (a) 54–1554 mV (scan rate of 20 mV s^{-1}) and (b) 54-1154 mV (scan rate of 50 mV s^{-1}).

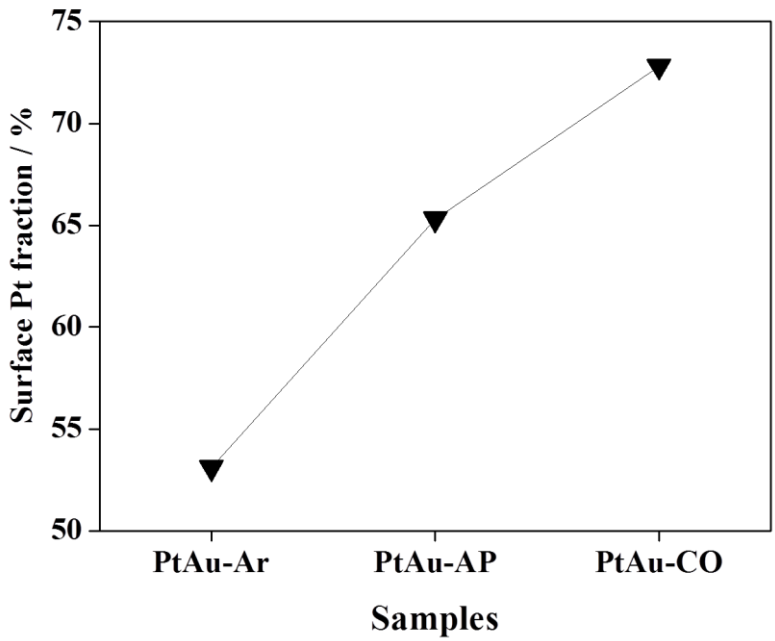

Figure 3.23 Surface atomic fractions of Pt in the PtAu nanoparticles calculated from ECA_{Pt} and ECA_{Au}.

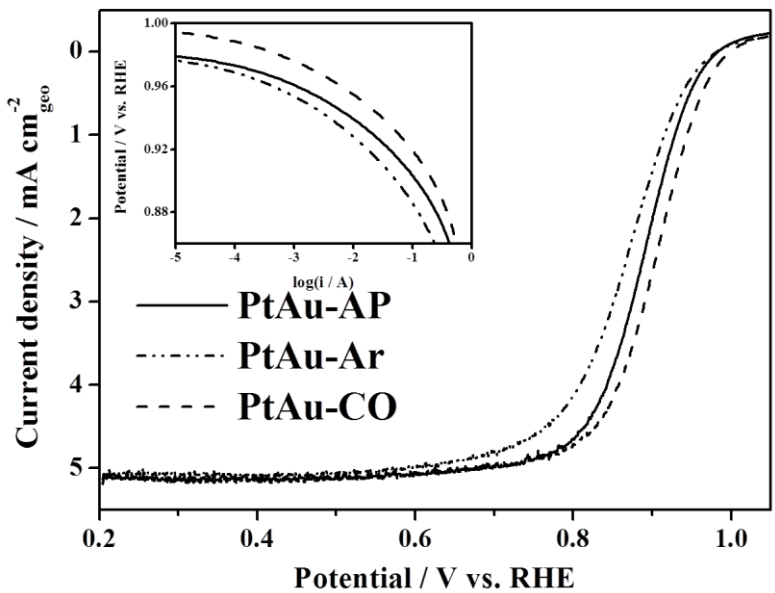

Figure 3.24 ORR polarization curve of PtAu-CO (- - -), PtAu-Ar (–•–), and PtAu-AP (——); Corresponding Tafel plot of the catalysts (instet).

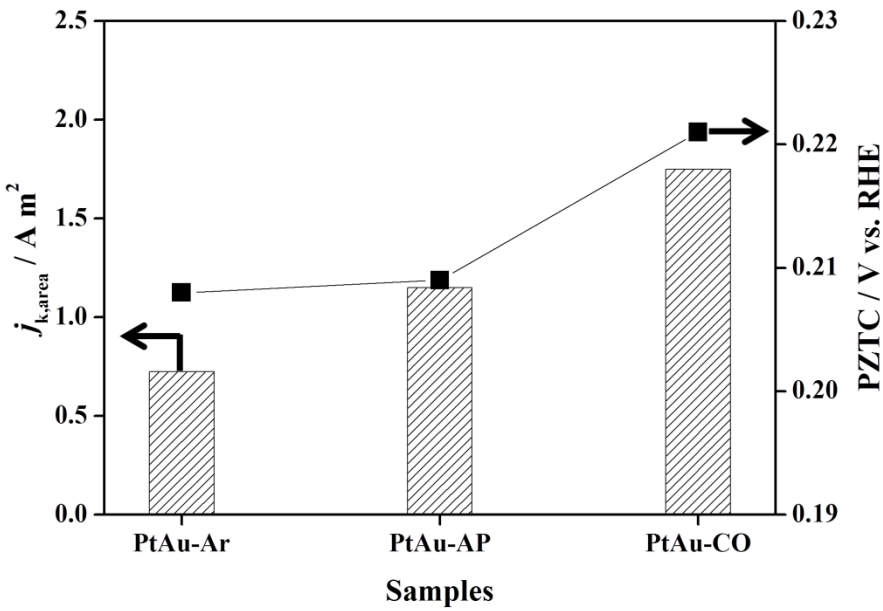

Figure 3.25 Specific activity (i_k / ECA_{Pt} at 0.9 V) (bar, left) and PZTC (■, right) of PtAu/C catalysts.

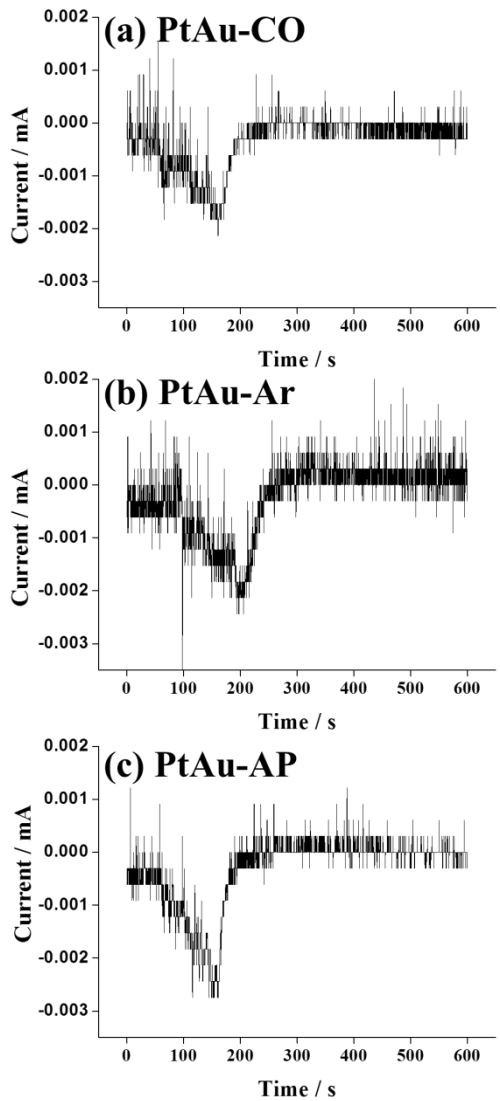

Figure 3.26 CO-displacement current-time profile of (a) PtAu-CO, (b) PtAu-Ar and (c) PtAu-AP.

3.3 Se-modified-Ru nanoparticles with phosphoric acid

High temperature-polymer electrolyte membrane fuel cells (HT-PEMFCs) have received increasing interest because they are highly efficient and exhibit fuel flexibility [89]. Phosphoric acid-doped polybenzimidazole (PBI) membranes have been widely adopted as polymer electrolyte membranes because they have high ionic conductivity and stability under HT-PEMFC operating conditions [90]. However, because strong phosphoric acid adsorption decreases platinum utilization, large quantities of a platinum catalyst must be used to facilitate good performance. Therefore, to enhance platinum utilization, several studies have reduced phosphate adsorption through, for example, surface modification of platinum [91], electronic structure modification with Pt alloys [92] and Pt_{shell}-Au_{core} electrocatalysts [93]. Despite recent advances in catalyst design, Pt loading for HT-PEMFC is still high, and the electrode is expensive. To produce cheaper and efficient fuel cells, non-platinum catalysts that are less affected by phosphoric acid may be a promising alternative.

As a non-platinum electrocatalyst, Se-modified-Ru ($RuSe_y$) has been studied because it has high ORR activity, high selectivity for a four-electron pathway, and an intrinsic tolerance for methanol oxidation [94]. Malakhov et al.

suggested that the ORR active site for $RuSe_y$ was the Ru surface [95], which was confirmed by *in-situ* XAS analysis of Se under ORR reaction conditions [96]. Se modification has been shown to decrease Ru-O bond energy and enhance ORR activity [97]. These findings suggest that Se modification may also decrease phosphoric acid adsorption on Ru because phosphoric acid adsorption strength should be proportionate to the Ru-O bond strength.

Herein, carbon-supported Se-modified-Ru catalysts ($RuSe_y$/C) were synthesized via a co-precipitation and reduction method [98], and their phosphate-adsorption characteristics were evaluated using electrochemical techniques and *in-situ* XAS. The effects of phosphoric acid on the oxidation states of Ru and Se and the Se-O interaction were analyzed at 600 mV to elucidate the phosphate adsorption site and investigate the interaction under ORR conditions. The effect of Se modification on the ORR activities with phosphoric acid was discussed based on the XAS analysis.

3.3.1 Physicochemical characterization

The Ru/C and $RuSe_y$/C catalysts were prepared by a reported procedure [98]. The nominal Ru-to-carbon ratio was 20% by weight. The atomic ratios of Se-to-Ru were nominally 33%, 66% and 133%. The Se-to-Ru atomic ratios for the $RuSe_y$/C were determined using X-ray photoelectron spectroscopy, which was consistent

with the nominal ratio; the catalysts were designated according to the Se-to-Ru ratio as follows: $RuSe_{0.31}$/C, $RuSe_{0.76}$/C, and $RuSe_{1.56}$/C.

In investigate the crystallographic structure of Ru/C and $RuSe_y$/C, XRD patterns for the catalysts were collected using a MiniFlex II diffractometer (Rigaku). XRD of Ru/C showed a typical hcp Ru structure (Figure 3.27a) and the $RuSe_y$/C samples were analyzed to be composed of $RuSe_2$ and Ru (Figure 3.27b-d). To elucidate the crystalline structure of $RuSe_y$/C catalysts, the broad peak of $RuSe_{1.56}$/C around 40^o could be deconvoluted, after background correction of carbon support, by the $RuSe_2$ pyrite (PDF# 65-3328) phase and Ru hcp (PDF# 65-1863) phase (Figure 3.28). The deconvolution of XRD peak was performed with a constant FWHM of 6.92° for all individual diffraction peaks. The deconvolution of XRD clearly suggested that the broad peak at 30-37° is the superposed diffraction peak of RuSe2 (200), (210), and (211) and the peak at ~43° is from Ru (100), (002), and (101). The variation of $RuSe_2$ and Ru peak intensities shows that the $RuSe_2$ content increased with higher Se content.

In order to confirm the structure of $RuSe_y$/C which was suggested to be mixture of crystalline Ru and amorphous like $RuSe_2$, heat-treatment was conducted with $RuSe_{1.56}$/C at 500 ℃ for 2 h under an Ar gas. After heat-treatment, pyrite structure of $RuSe_2$ and hcp Ru structure was clearly identified (Figure 3.29) [98]..

Bright field image of the Ru/C showed well dispersed Ru nanoparticle on

carbon support (Figure 3.30). TEM images of $RuSe_{1.56}$/C gave amorphous like nanoparticles on carbon support, which was likely consisted of $RuSe_2$. SAD pattern of the catalysts suggested that the Ru/C showed the highest crystallinity and the crystallinity decreased with the increase of Se contents (Figure 3.31). The decrease of crystallinity with the increase of Se contents accorded well with the XRD data which suggested decrease of crystalline Ru phase with the increase of Se contents.

Figure 3.32 presented the dark field image and corresponding EDS line scan profile of the $RuSe_y$/C catalysts. In $RuSe_{0.32}$/C, the EDS intensity ratio between Se and Ru showed poor relation likely due to low Se concentrations. As the increase of Se content, the intensity of Se became well corresponding to that of Ru. The EDS intensity of Ru and Se in $RuSe_{1.56}$/C showed virtually identical trend, indicating atomically well mixed Ru and Se compound.

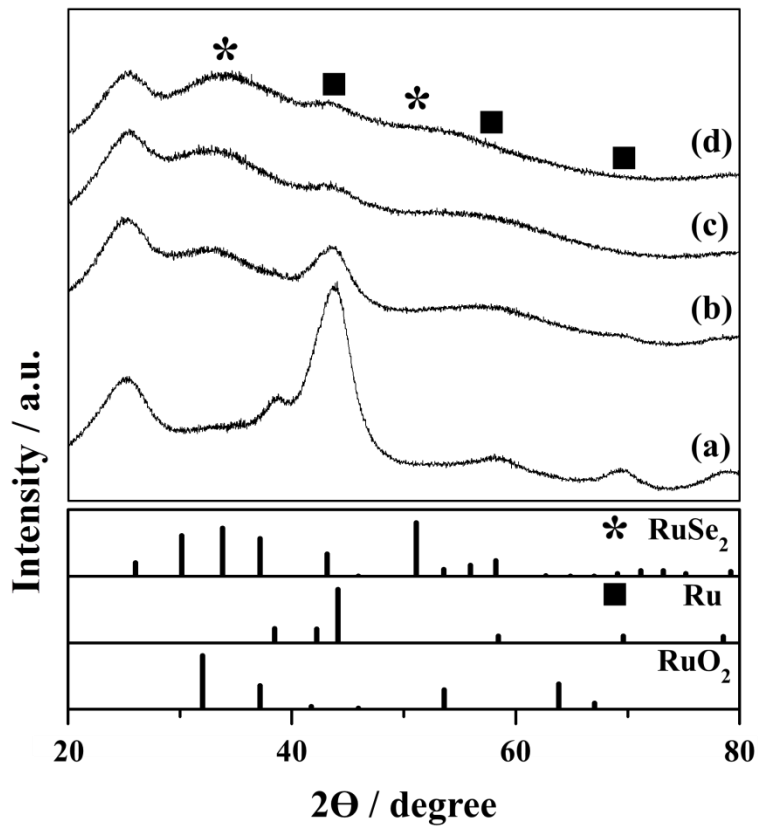

Figure 3.27 XRD of (a) Ru/C, (b) $RuSe_{0.32}$/C, (c) $RuSe_{0.76}$/C, and (d) $RuSe_{1.56}$/C.

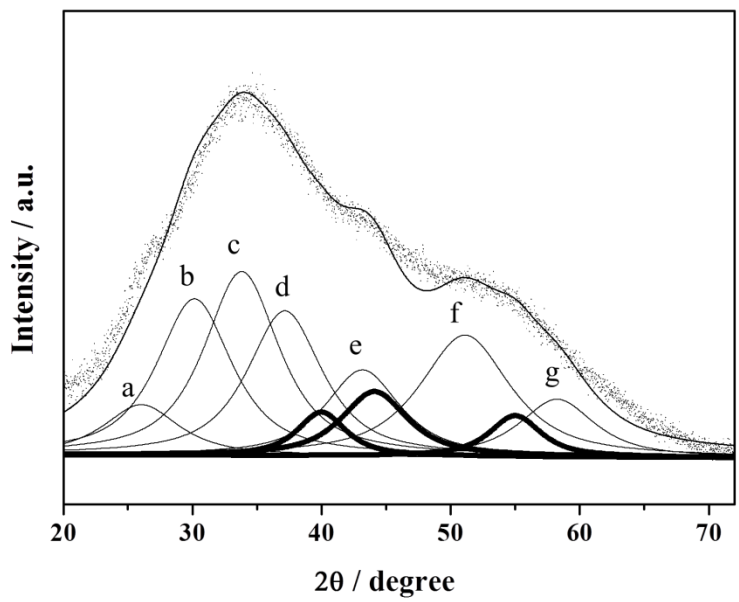

Figure 3.28 XRD curve fitting of $RuSe_{1.56}$/C with a constant line broadening. Thin lines (a-g) and thick lines correspond to XRD of $RuSe_2$ (pyrite structure) and Ru (hcp structure), respectively. The peaks (a-g) denote $RuSe_2$ (111), (200), (210), (211), (220), (311), and (321), peaks, respectively.

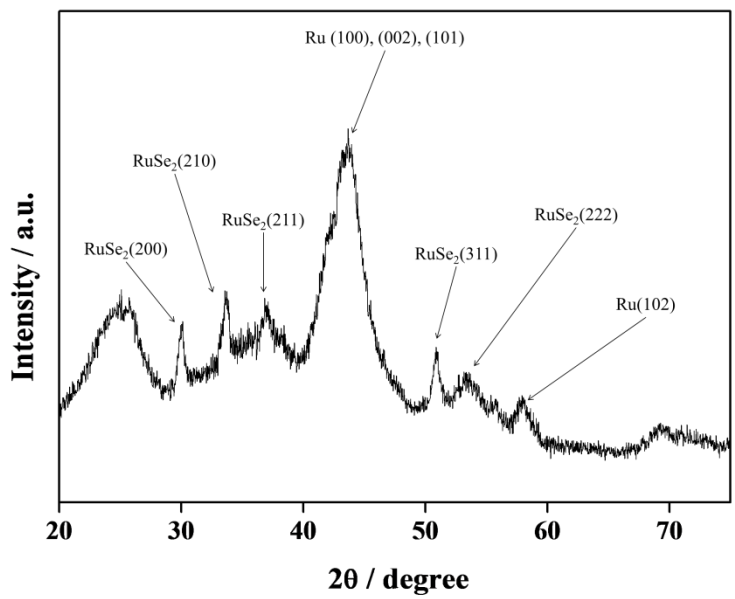

Figure 3.29 XRD of heat-treated $RuSe_{1.56}$/C.

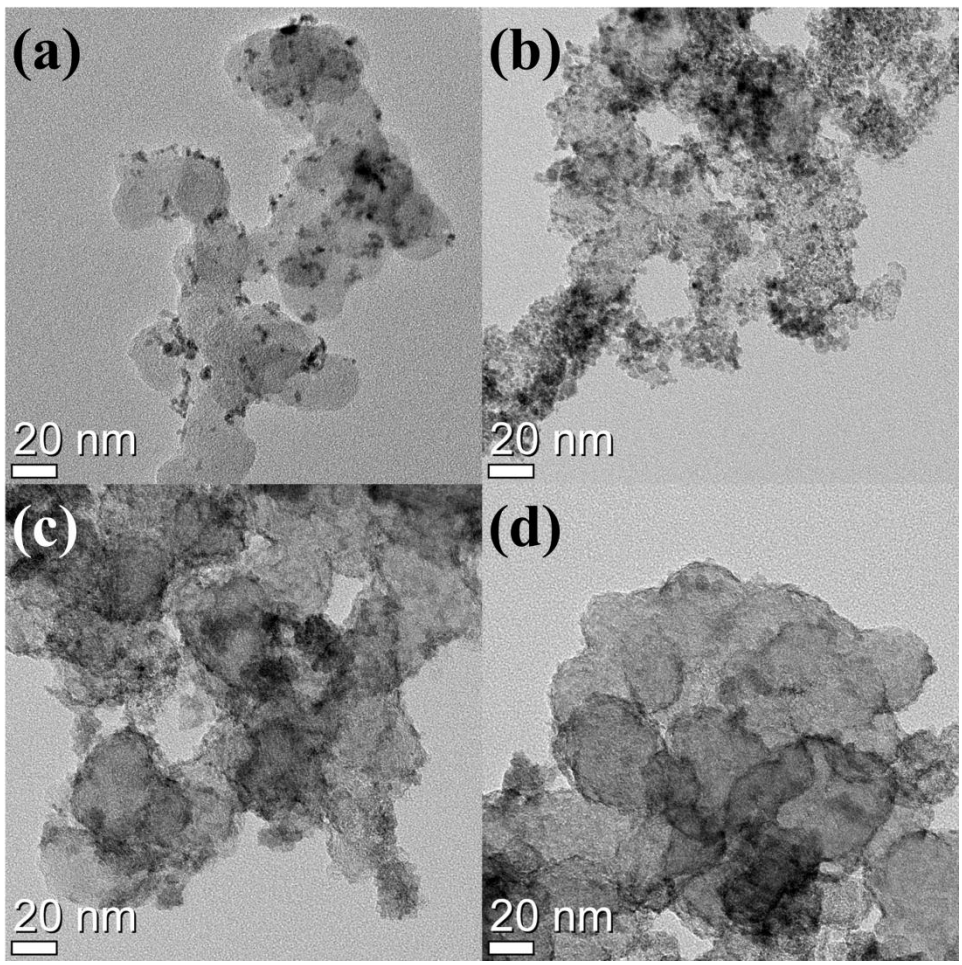

Figure 3.30 Bright field image of (a) Ru/C, (b) $RuSe_{0.32}$/C, (c) $RuSe_{0.76}$/C, and (d) $RuSe_{1.56}$/C.

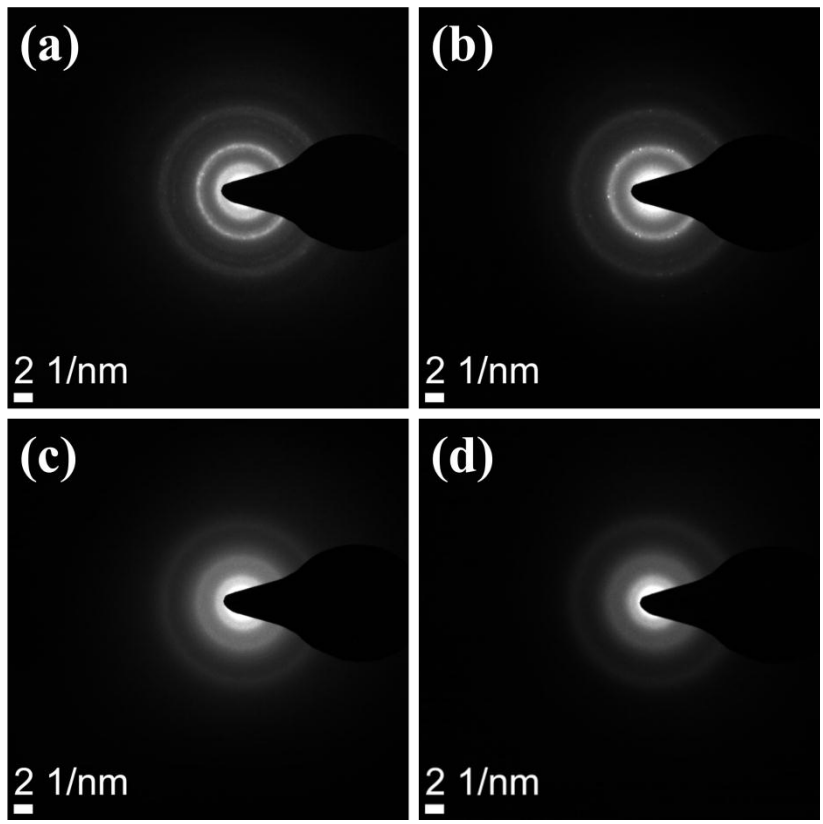

Figure 3.31 SAD pattern of (a) Ru/C, (b) $RuSe_{0.32}$/C, (c) $RuSe_{0.76}$/C, and (d) $RuSe_{1.56}$/C.

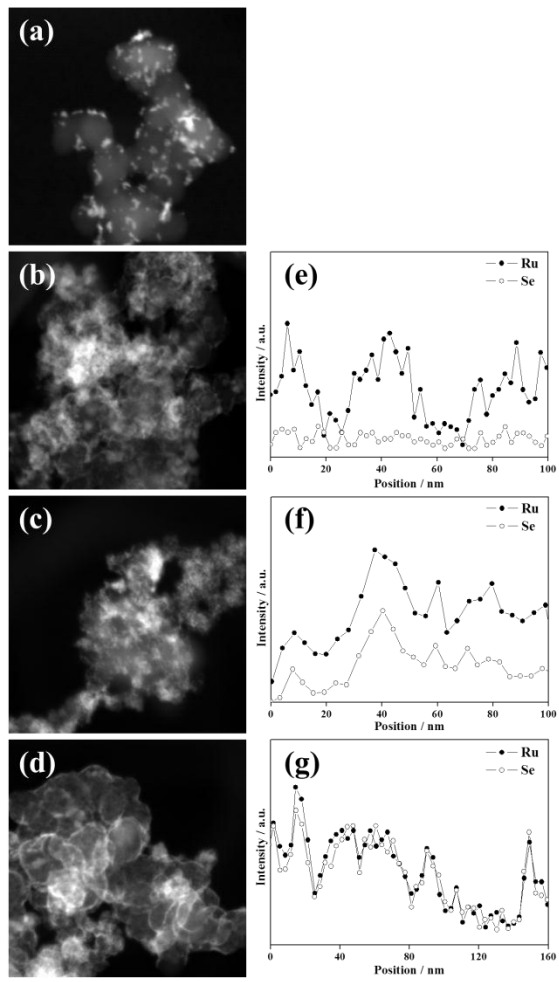

Figure 3.32 Dark field image of of (a) Ru/C, (b) $RuSe_{0.32}$/C, (c) $RuSe_{0.76}$/C, and (d) $RuSe_{1.56}$/C; EDS line scan profile of (e) $RuSe_{0.32}$/C, (f) $RuSe_{0.76}$/C, and (g) $RuSe_{1.56}$/C.

3.3.2 Electrochemical characterization

The cyclic voltammogram (CV) and ORR polarization of the catalysts were determined using a PGSTAT potentiostat (Eco Chemie) in Ar and O_2 saturated 0.1 M $HClO_4$, respectively. To investigate the effect of phosphoric acid on CV and ORR polarization, the CV and ORR polarization curves were recorded in 0.1 M $HClO_4$ + 10 mM H_3PO_4. The electrode potential was reported with respect to a normal hydrogen electrode (NHE).

In an RDE experiment, the ORR activity of Ru/C decreased after addition of 10 mM H_3PO_4 (Figure 3.33), which was demonstrated by the polarization curve shift in the negative potential direction. From the experimental current density (i) and limiting current (i_l), the kinetic current density (i_k) was calculated based on the Koutecky-Levich equation ($1/i = 1/i_k + 1/i_l$). The kinetic current density at 0.6 V ($i_{k,0.6\,V}$) decreased by 26.8% (2.61 mA g_{Ru}^{-1} → 1.91 mA g_{Ru}^{-1}).

Depressed ORR activity upon phosphoric acid addition has been explained by active site blocking due to the adsorption of phosphoric acid molecules (HPA: H_3PO_4) or phosphate anions (PA^-: $H_2PO_4^-$) [91-93, 99]. However, for $RuSe_{1.56}$/C, which is primarily composed of $RuSe_2$, the ORR activity was enhanced by phosphoric acid addition as shown in Figure 3.34 ($i_{k,0.6\,V}$: 1.63 mA g_{RuSey}^{-1} → 2.66 mA g_{RuSey}^{-1}). Accordingly, enhancement of $i_{k,0.6\,V}$ with 10 mM phosphoric acid gradually increased with higher Se content as follows: 17.8%

($RuSe_{0.32}$/C) → 43.4% ($RuSe_{0.76}$/C) → 63.8% ($RuSe_{1.56}$/C). Even though the activity was changed by phosphoric acid, the ORR mechanism on Ru/C and $RuSe_y$/C catalysts seems to be not changed based on the constant Tafel slopes.

The enhanced ORR activity with phosphoric acid addition suggests that the activity at the active site in $RuSe_y$/C catalysts increases with HPA/PA^- adsorption, which compensates for the decreased number of active sites. For $RuSe_y$/C, it has been reported that, when the Ru catalyst is modified by Se atoms, the Ru-O bonding energy decreases through electronic repulsion between OH_{ad} and neighboring Se atoms [97], and accordingly, the overall ORR reaction is enhanced as the rate-determining OH_{ad} desorption process becomes faster [100]. Thus, when phosphoric acid is added to $RuSe_y$/C catalysts, HPA/PA^- adsorption on Ru atoms is likely less favorable compared with Ru/C, and the ORR reaction may be further enhanced if electrostatic repulsion is increased by HPA/PA^- adsorption on Se (Se-PA_{ad}).

For experimental characterization of HPA/PA^- adsorption on the Ru and $RuSe_y$ surfaces, CV and *in-situ* XAS were performed with and without 10 mM H_3PO_4 in Pohang Accelerator Laboratory (PAL) 10C beamline. The spectra were collected under the fluorescence mode at 0.6 V. Before investigating the HPA/PA^- adsorption on $RuSe_y$/C surfaces, in-situ XAS of Ru/C and $RuSe_y$/C in 0.1 M HClO4 was performed to verify the experimental techniques. As reported by

Ramaswamy et al. [97], the XANES of Ru/C was gradually increased as the electrode potential increased (Figure 3.35). The increase of XANES peak was suggested to be oxidation of Ru surfaces. In $RuSe_y$/C, the XANES was hardly affected by the applied potential up to 800 mV and showed large increase of XANES peak at 1 V, and were in good agreement with the previous report. The virtually identical XASNE peak in $RuSe_y$/C up to the applied potential of 800 mV (Figure 3.35) was attributed to the hindered oxidation of Se by Se atoms in $RuSe_y$/C. Se atoms in the RuSey/C was suggested to be oxidized and protect the Ru from oxidation [97].

In 0.1 M $HClO_4$, the Ru/C and $RuSe_{1.56}$/C catalysts had a typical CV (Figure 3.36) [94, 101]. The Ru/C had a large double layer capacitance from multilayer oxidation of Ru surfaces and an oxide reduction peak at ~0.2 V, which is consistent with the reported characteristics of polycrystalline Ru [102]. When 10 mM H_3PO_4 was added to Ru/C, a broad anodic peak appeared at ~0.5 V, which originated from the electrochemical adsorption of HPA and PA^- to form Ru-PA_{ad} [103, 104]. The PA_{ad} to Ru surface atomic ratio was estimated at 7% from the integrated charge for Ru-PA_{ad} formation (13.3 C g_{Ru}^{-1}) with the assumption of uniform and spherical Ru particles (diameter: 5 nm). Because one PA_{ad} typically coordinates with three surface atoms, PA_{ad} coverage on a Ru surface may be as high as 21%. However, *in-situ* XAS analysis showed that the absorption edge

energy (E_0) in Ru/C (Figure 3.37a), which depends on Ru-O bond formation [95-97], was not significantly changed after the H_3PO_4 addition. Therefore, it can be concluded that Ru surfaces are initially covered in high levels of OH_{ad} or H_2O_{ad} at 0.6 V [105, 106], and high levels of PA_{ad} replace these chemicals through phosphoric acid addition, which was confirmed by CV and XANES spectra.

In $RuSe_{1.56}$/C, the Ru oxide reduction peak was significantly depressed from the increased $RuSe_2$ [97]. When 10 mM H_3PO_4 was added to $RuSe_{1.56}$/C, the anodic peak near 0.5 V was not observed, which indicates that electrochemical adsorption of HPA/PA^- was not significant. However, HPA/PA^- may affect $RuSe_{1.56}$/C in different ways because phosphoric acid addition decreased Ru oxidation state in $RuSe_{1.56}$/C compared to that without phosphoric acid (Figure 3.37b).

In-situ XAS analysis of the Se K region, which was recorded at 0.6 V, strongly suggests an interaction between the Se atom and HPA/PA^-. When phosphoric acid was added, the E_0 for Se K shifted positively, which indicates Se oxidation (Figure 3.38a), and the Se-O interaction increased as shown in the extended X-ray absorption fine structure (EXAFS) data (Figure 3.38b). The effect of HPA/PA^- adsorption on the Ru oxidation state at the $RuSe_y$ surface is not clearly understood, but electrostatic repulsion between Se-PA_{ad} and O_{ad} on Ru is likely ascribed to the suppressed Ru oxidation. As the electron-rich PA_{ad} on Se should

increase electrostatic repulsion between O_{ad} on Ru and Se, the PA_{ad} should decrease Ru-O bond energy. Future research on charge redistribution at the Se-PA_{ad} and Ru surfaces should yield a detailed explanation of the effect of Se-PA_{ad} on the Ru oxidation state and the electrostatic repulsion between Se and O_{ad}.

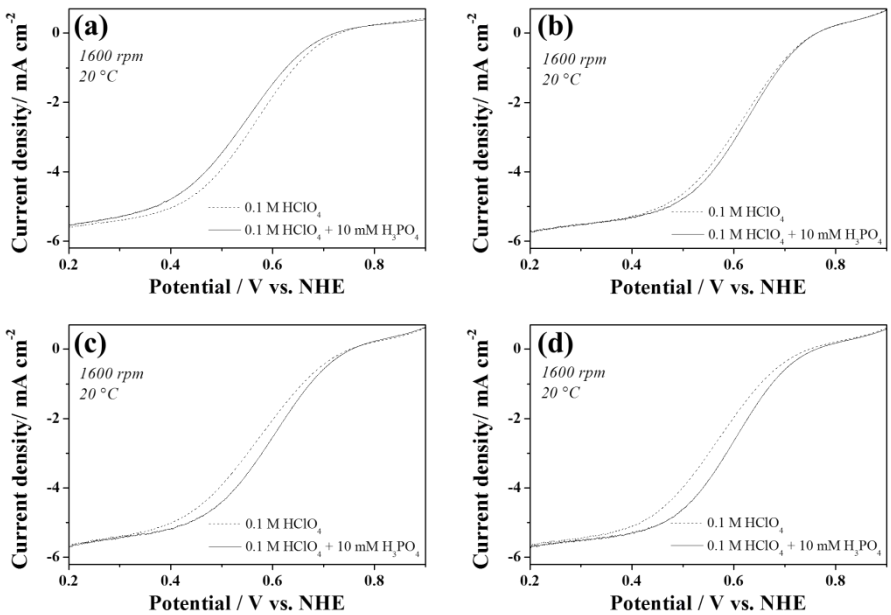

Figure 3.33 ORR polarization curves of (a) Ru/C, (b) $RuSe_{0.32}$/C, (c) $RuSe_{0.76}$/C, and (d) $RuSe_{1.56}$/C in 0.1 M $HClO_4$ (— · —) and 0.1 M $HClO_4$ + 10 mM H_3PO_4 (——).

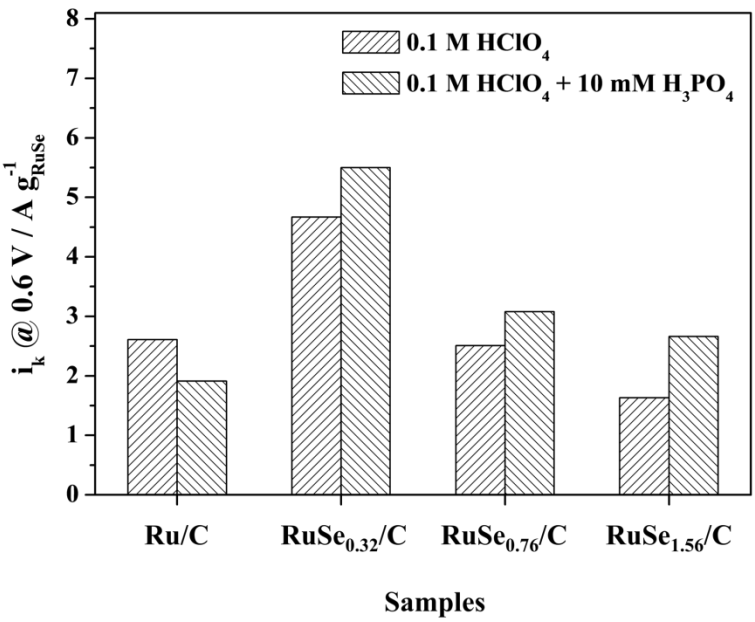

Figure 3.34 ORR mass activity (i_k / g_{RuSe} @ 0.6 V) of catalysts with (▧) and without (▨) 10 mM phosphoric acid.

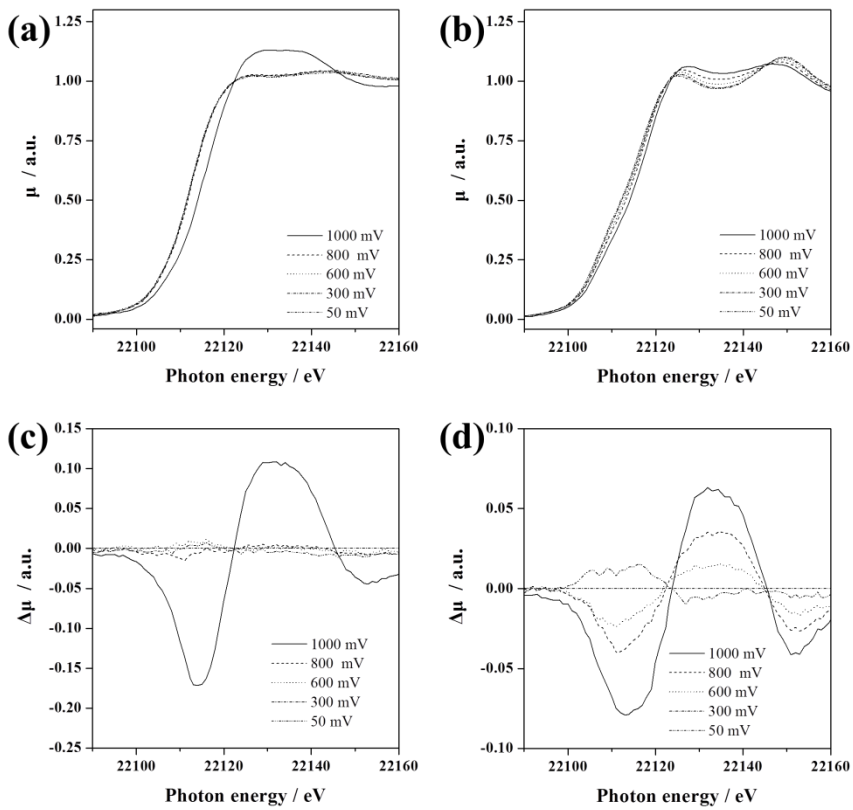

Figure 3.35 XANES spectra of (a) Ru/C and (b) $RuSe_{1.56}$/C at 50 (− ·· −), 300 (− ·−), 600 (·····), 800 (−−−), and 1000 (——) mV.; Differences in XANES spectra (Δμ = μ(x mV) - μ(300 mV)) at a potential of interest and 300 mV.

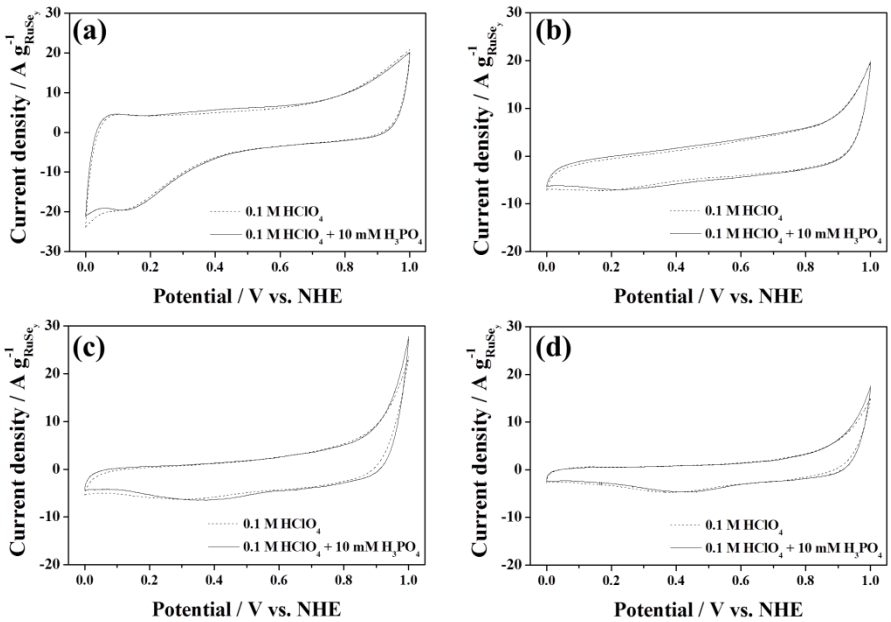

Figure 3.36 CV of (a) Ru/C, (b) $RuSe_{0.32}$/C, (c) $RuSe_{0.76}$/C, and (d) $RuSe_{1.56}$/C in 0.1 M $HClO_4$ (– · –) and 0.1 M $HClO_4$ + 10 mM H_3PO_4 (——) at a scan rate of 20 mV s^{-1}.

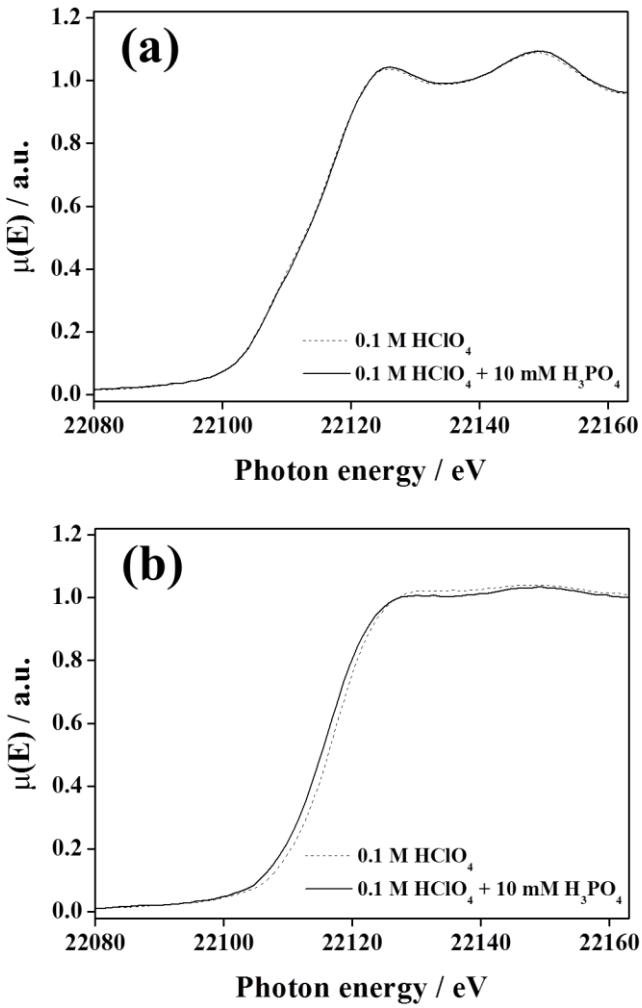

Figure 3.37 XANES spectra of Ru K in (a) Ru/C and (b) $RuSe_{1.56}$/C at 600 mV with (– – –) and without (——) 10 mM phosphoric acid.

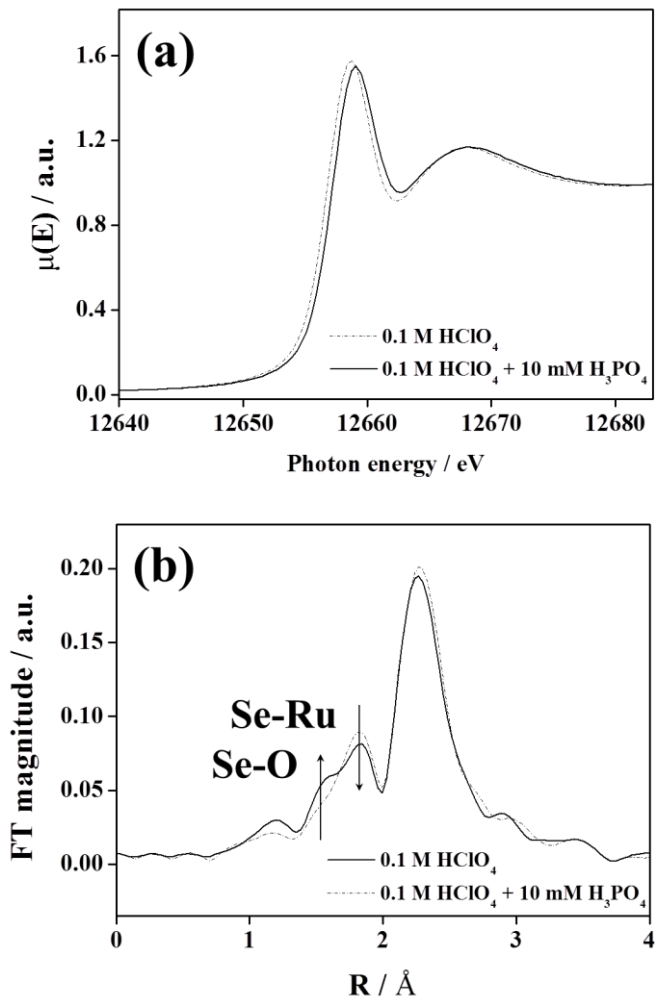

Figure 3.38 (a) XANES spectra of Se K in $RuSe_{1.56}$/C at 600 mV with (– – –) and without (——) 10 mM phosphoric acid.; (b) Radial distribution function obtained from k-weighted EXAFS of Se K in $RuSe_{1.56}$/C at 600 mV with (– – –) and without (——) 10 mM phosphoric acid.

3.4 References

[1] W.P. Zhou, X. Yang, M.B. Vukmirovic, B.E. Koel, J. Jiao, G. Peng, M. Mavrikakis, R.R. Adzic, Improving electrocatalysts for O2 reduction by fine-tuning the Pt-support interaction: Pt monolayer on the surfaces of a Pd3Fe(111) single-crystal alloy, Journal of the American Chemical Society, 131 (2009) 12755-12762.

[2] L. Wang, Y. Yamauchi, Autoprogrammed Synthesis of Triple-Layered Au@Pd@Pt Core−Shell Nanoparticles Consisting of a Au@Pd Bimetallic Core and Nanoporous Pt Shell, Journal of the American Chemical Society, 132 (2010) 13636-13638.

[3] K.S. Lee, I.S. Park, H.Y. Park, T.Y. Jeon, Y.E. Sung, PtRu overlayers on Au nanoparticles for methanol electro-oxidation, Catalysis Today, 146 (2009) 20-24.

[4] J.L. Zhang, M.B. Vukmirovic, Y. Xu, M. Mavrikakis, R.R. Adzic, Controlling the catalytic activity of platinum-monolayer electrocatalysts for oxygen reduction with different substrates, Angewandte Chemie International Edition, 44 (2005) 2132-2135.

[5] J. Zhang, Y. Mo, M.B. Vukmirovic, R. Klie, K. Sasaki, R.R. Adzic, Platinum Monolayer Electrocatalysts for O2Reduction: Pt Monolayer on Pd(111) and on Carbon-Supported Pd Nanoparticles, The Journal of Physical Chemistry B, 108

(2004) 10955-10964.

[6] K. Sasaki, R.R. Adzic, Monolayer-level Ru- and NbO2-supported platinum electrocatalysts for methanol oxidation, Journal of the Electrochemical Society, 155 (2008) B180-B186.

[7] M. Shao, A. Peles, K. Shoemaker, M. Gummalla, P.N. Njoki, J. Luo, C.-J. Zhong, Enhanced Oxygen Reduction Activity of Platinum Monolayer on Gold Nanoparticles, The Journal of Physical Chemistry Letters, 2 (2010) 67-72.

[8] Y. Xing, Y. Cai, M.B. Vukmirovic, W.-P. Zhou, H. Karan, J.X. Wang, R.R. Adzic, Enhancing Oxygen Reduction Reaction Activity via Pd−Au Alloy Sublayer Mediation of Pt Monolayer Electrocatalysts, The Journal of Physical Chemistry Letters, 1 (2010) 3238-3242.

[9] R. Adzic, J. Zhang, K. Sasaki, M. Vukmirovic, M. Shao, J. Wang, A. Nilekar, M. Mavrikakis, J. Valerio, F. Uribe, Platinum Monolayer Fuel Cell Electrocatalysts, Topics in Catalysis, 46 (2007) 249-262.

[10] W.-P. Zhou, K. Sasaki, D. Su, Y. Zhu, J.X. Wang, R.R. Adzic, Gram-Scale-Synthesized Pd2Co-Supported Pt Monolayer Electrocatalysts for Oxygen Reduction Reaction, The Journal of Physical Chemistry C, 114 (2010) 8950-8957.

[11] I. Choi, S.H. Ahn, J.J. Kim, O.J. Kwon, Preparation of Ptshell–Pdcore nanoparticle with electroless deposition of copper for polymer electrolyte

membrane fuel cell, Applied Catalysis B-Environmental, 102 (2011) 608-613.

[12] N.V. Long, T. Duy Hien, T. Asaka, M. Ohtaki, M. Nogami, Synthesis and characterization of Pt–Pd alloy and core-shell bimetallic nanoparticles for direct methanol fuel cells (DMFCs): Enhanced electrocatalytic properties of well-shaped core-shell morphologies and nanostructures, International Journal of Hydrogen Energy, 36 (2011) 8478-8491.

[13] F. Taufany, C.-J. Pan, J. Rick, H.-L. Chou, M.-C. Tsai, B.-J. Hwang, D.-G. Liu, J.-F. Lee, M.-T. Tang, Y.-C. Lee, C.-I. Chen, Kinetically Controlled Autocatalytic Chemical Process for Bulk Production of Bimetallic Core–Shell Structured Nanoparticles, ACS Nano, 5 (2011) 9370-9381.

[14] W.-r. Lee, M.G. Kim, J.-r. Choi, J.-I. Park, S.J. Ko, S.J. Oh, J. Cheon, Redox−Transmetalation Process as a Generalized Synthetic Strategy for Core−Shell Magnetic Nanoparticles, Journal of the American Chemical Society, 127 (2005) 16090-16097.

[15] Y. Wang, N. Toshima, Preparation of Pd−Pt Bimetallic Colloids with Controllable Core/Shell Structures, The Journal of Physical Chemistry B, 101 (1997) 5301-5306.

[16] J. Zhang, M.B. Vukmirovic, K. Sasaki, A.U. Nilekar, M. Mavrikakis, R.R. Adzic, Mixed-Metal Pt Monolayer Electrocatalysts for Enhanced Oxygen Reduction Kinetics, Journal of the American Chemical Society, 127 (2005)

12480-12481.

[17] C. Roth, N. Benker, R. Theissmann, R.J. Nichols, D.J. Schiffrin, Bifunctional Electrocatalysis in Pt−Ru Nanoparticle Systems, Langmuir, 24 (2008) 2191-2199.

[18] N.M. Markovic, T.J. Schmidt, V. Stamenkovic, P.N. Ross, Oxygen Reduction Reaction on Pt and Pt Bimetallic Surfaces: A Selective Review, Fuel Cells, 1 (2001) 105-116.

[19] C. Roth, A.J. Papworth, I. Hussain, R.J. Nichols, D.J. Schiffrin, A Pt/Ru nanoparticulate system to study the bifunctional mechanism of electrocatalysis, Journal of Electroanalytical Chemistry, 581 (2005) 79-85.

[20] N. Krishnankutty, J. Li, M. Albert Vannice, The effect of Pd precursor and pretreatment on the adsorption and absorption behavior of supported Pd catalysts, Applied Catalysis A: General, 173 (1998) 137-144.

[21] F. Tao, M.E. Grass, Y. Zhang, D.R. Butcher, J.R. Renzas, Z. Liu, J.Y. Chung, B.S. Mun, M. Salmeron, G.A. Somorjai, Reaction-Driven Restructuring of Rh-Pd and Pt-Pd Core-Shell Nanoparticles, Science, 322 (2008) 932-934.

[22] D. Szczuko, J. Werner, S. Oswald, G. Behr, K. Wetzig, XPS investigations of surface segregation of doping elements in SnO2, Applied Surface Science, 179 (2001) 301-306.

[23] J.E. Muller, O. Jepsen, O.K. Andersen, J.W. Wilkins, Systematic structure in

the K-edge photoabsorption spectra of the 4d transition metals: Theory, Physical Review Letters, 40 (1978) 720-722.

[24] I. Moysan, V. Paul-Boncour, S. Thiéaut, E. Sciora, J.M. Fournier, R. Cortes, S. Bourgeois, A. Percheron-Guéan, Pd-Pt alloys: correlation between electronic structure and hydrogenation properties, Journal of Alloys and Compounds, 322 (2001) 14-20.

[25] I. Moysan, V. Paul-Boncour, S. Thiébaut, E. Sciora, J.M. Fournier, R. Cortes, S. Bourgeois, A. Percheron-Guégan, Pd–Pt alloys: correlation between electronic structure and hydrogenation properties, Journal of Alloys and Compounds, 322 (2001) 14-20.

[26] P. Lagarde, T. Murata, G. Vlaic, E. Freund, H. Dexpert, J.P. Bournonville, EXAFS studies of PtAl2O3 catalysts, Journal of Catalysis, 84 (1983) 333-343.

[27] S. Chen, A. Kucernak, Electrocatalysis under Conditions of High Mass Transport: Investigation of Hydrogen Oxidation on Single Submicron Pt Particles Supported on Carbon, The Journal of Physical Chemistry B, 108 (2004).

[28] P.P. Wells, E.M. Crabb, C.R. King, R. Wiltshire, B. Billsborrow, D. Thompsett, A.E. Russell, Preparation, structure, and stability of Pt and Pd monolayer modified Pd and Pt electrocatalysts, Physical Chemistry Chemical Physics, 11 (2009) 5773-5781.

[29] C. Wang, B. Peng, H.-N. Xie, H.-X. Zhang, F.-F. Shi, W.-B. Cai, Facile Fabrication of Pt, Pd and Pt−Pd Alloy Films on Si with Tunable Infrared Internal Reflection Absorption and Synergetic Electrocatalysis, The Journal of Physical Chemistry C, 113 (2009) 13841-13846.

[30] A.V. Petukhov, W. Akemann, K.A. Friedrich, U. Stimming, Kinetics of electrooxidation of a CO monolayer at the platinum/electrolyte interface, Surface Science, 402–404 (1998) 182-186.

[31] C. Saravanan, M.T.M. Koper, N.M. Markovic, M. Head-Gordon, P.N. Ross, Modeling base voltammetry and CO electrooxidation at the Pt(111)-electrolyte interface: Monte Carlo simulations including anion adsorption, Physical Chemistry Chemical Physics, 4 (2002) 2660-2666.

[32] B. Andreaus, M. Eikerling, Active site model for CO adlayer electrooxidation on nanoparticle catalysts, Journal of Electroanalytical Chemistry, 607 (2007) 121-132.

[33] H. Wang, Z. Jusys, R.J. Behm, H.D. Abruña, New Insights into the Mechanism and Kinetics of Adsorbed CO Electrooxidation on Platinum: Online Mass Spectrometry and Kinetic Monte Carlo Simulation Studies, The Journal of Physical Chemistry C, 116 (2012) 11040-11053.

[34] N.M. Marković, B.N. Grgur, P.N. Ross, Temperature-Dependent Hydrogen Electrochemistry on Platinum Low-Index Single-Crystal Surfaces in Acid

Solutions, The Journal of Physical Chemistry B, 101 (1997) 5405-5413.

[35] I. Esparbé, E. Brillas, F. Centellas, J.A. Garrido, R.M. Rodríguez, C. Arias, P.-L. Cabot, Structure and electrocatalytic performance of carbon-supported platinum nanoparticles, Journal of Power Sources, 190 (2009) 201-209.

[36] Y. Sun, Y. Dai, Y. Liu, S. Chen, A rotating disk electrode study of the particle size effects of Pt for the hydrogen oxidation reaction, Physical Chemistry Chemical Physics, 14 (2012) 2278-2285.

[37] A.F. Innocente, A.C.D. Â ngelo, Electrocatalysis of oxidation of hydrogen on platinum ordered intermetallic phases: Kinetic and mechanistic studies, Journal of Power Sources, 162 (2006) 151-159.

[38] Y.-H. Cho, B. Choi, Y.-H. Cho, H.-S. Park, Y.-E. Sung, Pd-based PdPt(19:1)/C electrocatalyst as an electrode in PEM fuel cell, Electrochemistry Communications, 9 (2007) 378-381.

[39] M.S. Rau, P.M. Quaino, M.R. Gennero de Chialvo, A.C. Chialvo, Hydrogen oxidation reaction: Evidences of different electrocatalytic activity between α and β Pd–H, Electrochemistry Communications, 10 (2008) 208-212.

[40] P.M. Quaino, J.L. Fernández, M.R. Gennero de Chialvo, A.C. Chialvo, Hydrogen oxidation reaction on microelectrodes: Analysis of the contribution of the kinetic routes, Journal of Molecular Catalysis A: Chemistry, 252 (2006) 156-162.

[41] T. Mitsui, M.K. Rose, E. Fomin, D.F. Ogletree, M. Salmeron, Dissociative hydrogen adsorption on palladium requires aggregates of three or more vacancies, Nature, 422 (2003) 705-707.

[42] J. Greeley, J.K. Nørskov, Electrochemical dissolution of surface alloys in acids: Thermodynamic trends from first-principles calculations, Electrochimica Acta, 52 (2007) 5829-5836.

[43] Y. Zhang, Q. Huang, Z. Zou, J. Yang, W. Vogel, H. Yang, Enhanced durability of Au cluster decorated Pt nanoparticles for the oxygen reduction reaction, The Journal of Physical Chemistry C, 114 (2010) 6860-6868.

[44] P. Hernández-Fernández, S. Rojas, P. Ocón, J.L.G. De La Fuente, J.S. Fabián, J. Sanza, M.A. Peña, F.J. García-García, P. Terreros, J.L.G. Fierro, Influence of the preparation route of bimetallic Pt-Au nanoparticle electrocatalysts for the oxygen reduction reaction, The Journal of Physical Chemistry C, 111 (2007) 2913-2923.

[45] M.I. Awad, M.S. El-Deab, T. Ohsaka, Tailor-designed platinum nanoparticles electrodeposited onto gold electrode: Catalytic activity for oxygen reduction, Journal of the Electrochemical Society, 154 (2007) B810-B816.

[46] G. Chen, Y. Li, D. Wang, L. Zheng, G. You, C.J. Zhong, L. Yang, F. Cai, J. Cai, B.H. Chen, Carbon-supported PtAu alloy nanoparticle catalysts for enhanced electrocatalytic oxidation of formic acid, Journal of Power Sources, 196 (2011)

8323-8330.

[47] I.S. Park, K.S. Lee, J.H. Choi, H.Y. Park, Y.E. Sung, Surface structure of Pt-modified Au nanoparticles and electrocatalytic activity in formic acid electro-oxidation, The Journal of Physical Chemistry C, 111 (2007) 19126-19133.

[48] N. Kristian, Y. Yu, P. Gunawan, R. Xu, W. Deng, X. Liu, X. Wang, Controlled synthesis of Pt-decorated Au nanostructure and its promoted activity toward formic acid electro-oxidation, Electrochimica Acta, 54 (2009) 4916-4924.

[49] J. Huang, H. Hou, T. You, Highly efficient electrocatalytic oxidation of formic acid by electrospun carbon nanofiber-supported Pt_xAu_{100-x} bimetallic electrocatalyst, Electrochemistry Communications, 11 (2009) 1281-1284.

[50] J. Wang, D.F. Thomas, A. Chen, Direct growth of novel alloyed PtAu nanodendrites, Chemical Communications, (2008) 5010-5012.

[51] J.H. Choi, K.W. Park, I.-S. Park, K. Kim, J.S. Lee, Y.-E. Sung, A PtAu nanoparticle electrocatalyst for methanol electro-oxidation in direct methanol fuel cells, Journal of the Electrochemical Society, 153 (2006) A1812-A1817.

[52] C.-W. Liu, Y.-C. Wei, K.-W. Wang, Preparation and characterization of carbon-supported Pt–Au cathode catalysts for oxygen reduction reaction, Journal of Colloid and Interface Science, 336 (2009) 654-657.

[53] Y. Ma, H. Zhang, H. Zhong, T. Xu, H. Jin, X. Geng, High active PtAu/C catalyst with core–shell structure for oxygen reduction reaction, Catalysis

Communications, 11 (2010) 434-437.

[54] B. Brown, S.D. Wolter, B.R. Stoner, J.T. Glass, Alloying Effects of Cosputtered Gold-Platinum Thin Films on the Oxygen Reduction Reaction in Acidic Electrolyte, Journal of the Electrochemical Society, 155 (2008) B852-B859.

[55] E. Irissou, F. Laplante, S. Garbarino, M. Chaker, D. Guay, Structural and Electrochemical Characterization of Metastable PtAu Bulk and Surface Alloys Prepared by Crossed-Beam Pulsed Laser Deposition, The Journal of Physical Chemistry C, 114 (2010) 2192-2199.

[56] B.N. Wanjala, J. Luo, B. Fang, D. Mott, C.-J. Zhong, Gold-platinum nanoparticles: alloying and phase segregation, Journal of Material Chemistry, 21 (2011) 4012-4020.

[57] B.N. Wanjala, J. Luo, R. Loukrakpam, B. Fang, D. Mott, P.N. Njoki, M. Engelhard, H.R. Naslund, J.K. Wu, L. Wang, O. Malis, C.-J. Zhong, Nanoscale Alloying, Phase-Segregation, and Core−Shell Evolution of Gold−Platinum Nanoparticles and Their Electrocatalytic Effect on Oxygen Reduction Reaction, Chemistry of Materials, 22 (2010) 4282-4294.

[58] J. Luo, M.M. Maye, V. Petkov, N.N. Kariuki, L. Wang, P. Njoki, D. Mott, Y. Lin, C.-J. Zhong, Phase Properties of Carbon-Supported Gold−Platinum Nanoparticles with Different Bimetallic Compositions, Chemistry of Materials,

17 (2005) 3086-3091.

[59] Y. Xing, Y. Cai, M.B. Vukmirovic, W.P. Zhou, H. Karan, J.X. Wang, R.R. Adzic, Enhancing oxygen reduction reaction activity via Pd-Au alloy sublayer mediation of Pt monolayer electrocatalysts, The Journal of Physical Chemistry Letters, 1 (2010) 3238-3242.

[60] M. Shao, A. Peles, K. Shoemaker, M. Gummalla, P.N. Njoki, J. Luo, C.J. Zhong, Enhanced oxygen reduction activity of platinum monolayer on gold nanoparticles, The Journal of Physical Chemistry Letters, 2 (2011) 67-72.

[61] J.K. Norskov, J. Rossmeisl, A. Logadottir, L. Lindqvist, J.R. Kitchin, T. Bligaard, H. Jonsson, Origin of the overpotential for oxygen reduction at a fuel-cell cathode, The Journal of Physical Chemistry B, 108 (2004) 17886-17892.

[62] J. Greeley, M. Mavrikakis, Near-surface alloys for hydrogen fuel cell applications, Catalysis Today, 111 (2006) 52-58.

[63] K.J.J. Mayrhofer, V. Juhart, K. Hartl, M. Hanzlik, M. Arenz, Adsorbate-Induced Surface Segregation for Core–Shell Nanocatalysts, Angewandte Chemie International Edition, 48 (2009) 3529-3531.

[64] J. Greeley, M. Mavrikakis, Alloy catalysts designed from first principles, Nature Materials, 3 (2004) 810-815.

[65] H.L. Skriver, N.M. Rosengaard, Surface energy and work function of elemental metals, Physical Review B, 46 (1992) 7157-7168.

[66] V.K. Kumikov, K.B. Khokonov, On the measurement of surface free energy and surface tension of solid metals, Journal of Applied Physics, 54 (1983) 1346-1350.

[67] E. Rach, J. Heitbaum, Electrochemically induced surface modifications of Pt-Au alloy, Electrochimica Acta, 32 (1987) 1173-1180.

[68] S.E. Hörnström, L. Johansson, A. Flodström, R. Nyholm, J. Schmidt-May, Surface and bulk core level binding energy shifts in Pt Au alloys, Surface Science, 160 (1985) 561-570.

[69] M. Yin, Y. Huang, L. Liang, J. Liao, C. Liu, W. Xing, Inhibiting CO formation by adjusting surface composition in PtAu alloys for methanol electrooxidation, Chemical Communications, 47 (2011).

[70] K.-W. Wang, S.-R. Chung, C.-W. Liu, Surface Segregation of Pd_xNi_{100-x} Alloy Nanoparticles, The Journal of Physical Chemistry C, 112 (2008) 10242-10246.

[71] J.J. Yeh, I. Lindau, Atomic subshell photoionization cross sections and asymmetry parameters: $1 \leq Z \leq 103$, Atomic Data and Nuclear Data Tables, 32 (1985) 1-155.

[72] W.M.R. C. D. Wagner, L. E. Davis, J. F. Moulder, G. E. Muilnenberg, Handbook of x-ray photoelectron spectroscopy : a reference book of standard data for use in x-ray photoelectron spectroscopy, Physical Electronics Division, Perkin-Elmer Corp., Eden Prairie, 1979.

[73] U.A. Paulus, T.J. Schmidt, H.A. Gasteiger, R.J. Behm, Oxygen reduction on a high-surface area Pt/Vulcan carbon catalyst: a thin-film rotating ring-disk electrode study, Journal of Electroanalytical Chemistry, 495 (2001) 134-145.

[74] J. Zhang, K. Sasaki, E. Sutter, R.R. Adzic, Stabilization of platinum oxygen-reduction electrocatalysts using gold clusters, Science, 315 (2007) 220-222.

[75] A.J. Bard, L.R. Faulkner, Electrochemical methods : fundamentals and applications, 2nd ed., John Wiley & Sons, Inc., New York, 2001.

[76] Y.H. Fang, Z.P. Liu, Mechanism of oxygen electro-reduction on Au-modified Pt: Minimizing O coverage and pt site exposure toward highly stable and active cathode, The Journal of Physical Chemistry C, 115 (2011) 17508-17515.

[77] Z. Peng, H. Yang, Designer platinum nanoparticles: Control of shape, composition in alloy, nanostructure and electrocatalytic property, Nano Today, 4 (2009) 143-164.

[78] V. Climent, N. García-Araez, E. Herrero, J. Feliu, Potential of zero total charge of platinum single crystals: A local approach to stepped surfaces vicinal to Pt(111), Russian Journal of Electrochemistry, 42 (2006) 1145-1160.

[79] V. Climent, G.A. Attard, J.M. Feliu, Potential of zero charge of platinum stepped surfaces: a combined approach of CO charge displacement and N2O reduction, Journal of Electroanalytical Chemistry, 532 (2002) 67-74.

[80] R. Gómez, V. Climent, J.M. Feliu, M.J. Weaver, Dependence of the Potential

of Zero Charge of Stepped Platinum (111) Electrodes on the Oriented Step-Edge Density: Electrochemical Implications and Comparison with Work Function Behavior, The Journal of Physical Chemistry B, 104 (1999) 597-605.

[81] G.A. Attard, O. Hazzazi, P.B. Wells, V.c. Climent, E. Herrero, J.M. Feliu, On the global and local values of the potential of zero total charge at well-defined platinum surfaces: stepped and adatom modified surfaces, Journal of Electroanalytical Chemistry, 568 (2004) 329-342.

[82] C. Angel, Measurement of the surface charge density of CO-saturated Pt(111) electrodes as a function of potential: the potential of zero charge of Pt(111), Surface Science, 572 (2004) 11-22.

[83] B. Alvarez, V. Climent, A. Rodes, J.M. Feliu, Potential of zero total charge of palladium modified Pt(111) electrodes in perchloric acid solutions, Physical Chemistry Chemical Physics, 3 (2001) 3269-3276.

[84] U.W. Hamm, D. Kramer, R.S. Zhai, D.M. Kolb, The pzc of Au(111) and Pt(111) in a perchloric acid solution: an ex situ approach to the immersion technique, Journal of Electroanalytical Chemistry, 414 (1996) 85-89.

[85] T. Sergio, Work function, electronegativity, and electrochemical behaviour of metals: II. Potentials of zero charge and “electrochemical” work functions, Journal of Electroanalytical Chemistry and Interfacial Electrochemistry, 33 (1971) 351-378.

[86] M.J. Weaver, Potentials of Zero Charge for Platinum(111)−Aqueous Interfaces: A Combined Assessment from In-Situ and Ultrahigh-Vacuum Measurements, Langmuir, 14 (1998) 3932-3936.

[87] K.J.J. Mayrhofer, D. Strmcnik, B.B. Blizanac, V. Stamenkovic, M. Arenz, N.M. Markovic, Measurement of oxygen reduction activities via the rotating disc electrode method: From Pt model surfaces to carbon-supported high surface area catalysts, Electrochimica Acta, 53 (2008) 3181-3188.

[88] M.Ø. Pedersen, S. Helveg, A. Ruban, I. Stensgaard, E. Lægsgaard, J.K. Nørskov, F. Besenbacher, How a gold substrate can increase the reactivity of a Pt overlayer, Surface Science, 426 (1999) 395-409.

[89] J. Zhang, Z. Xie, J. Zhang, Y. Tang, C. Song, T. Navessin, Z. Shi, D. Song, H. Wang, D.P. Wilkinson, Z.-S. Liu, S. Holdcroft, High temperature PEM fuel cells, Journal of Power Sources, 160 (2006) 872-891.

[90] J.K. Lee, J. Kerres, Synthesis and characterization of sulfonated poly(arylene thioether)s and their blends with polybenzimidazole for proton exchange membranes, Journal of Membrane Science, 294 (2007) 75-83.

[91] D. Strmcnik, M. Escudero-Escribano, K. Kodama, R. StamenkovicVojislav, A. Cuesta, N.M. Marković, Enhanced electrocatalysis of the oxygen reduction reaction based on patterning of platinum surfaces with cyanide, Nature Chemistry, 2 (2010) 880-885.

[92] M. Mamlouk, K. Scott, An investigation of Pt alloy oxygen reduction catalysts in phosphoric acid doped PBI fuel cells, Journal of Power Sources, 196 (2011) 1084-1089.

[93] K.-S. Lee, S.J. Yoo, D. Ahn, S.-K. Kim, S.J. Hwang, Y.-E. Sung, H.-J. Kim, E. Cho, D. Henkensmeier, T.-H. Lim, J.H. Jang, Phosphate adsorption and its effect on oxygen reduction reaction for PtxCoy alloy and Aucore–Ptshell electrocatalysts, Electrochimica Acta, 56 (2011) 8802-8810.

[94] D. Cao, A. Wieckowski, J. Inukai, N. Alonso-Vante, Oxygen reduction reaction on ruthenium and rhodium nanoparticles modified with selenium and sulfur, Journal of the Electrochemical Society, 153 (2006) A869-A874.

[95] I.V. Malakhov, S.G. Nikitenko, E.R. Savinova, D.I. Kochubey, N. Alonso-Vante, In Situ EXAFS Study To Probe Active Centers of Ru Chalcogenide Electrocatalysts During Oxygen Reduction Reaction, The Journal of Physical Chemistry B, 106 (2002) 1670-1676.

[96] J. Inukai, D. Cao, A. Wieckowski, K.C. Chang, A. Menzel, V. Komanicky, H. You, In-situ synchrotron X-ray spectroscopy of ruthenium nanoparticles modified with selenium for oxygen reduction reaction, in: ECS Transactions, Cancun, 2006, pp. 161-170.

[97] N. Ramaswamy, R.J. Allen, S. Mukerjee, Electrochemical Kinetics and X-ray Absorption Spectroscopic Investigations of Oxygen Reduction on Chalcogen-

Modified Ruthenium Catalysts in Alkaline Media, The Journal of Physical Chemistry C, 115 (2011) 12650-12664.

[98] C. Delacôte, A. Bonakdarpour, C.M. Johnston, P. Zelenay, A. Wieckowski, Aqueous-based synthesis of ruthenium-selenium catalyst for oxygen reduction reaction, Faraday Discussions, 140 (2009) 269-281.

[99] Q. He, X. Yang, W. Chen, S. Mukerjee, B. Koel, S. Chen, Influence of phosphate anion adsorption on the kinetics of oxygen electroreduction on low index Pt(hkl) single crystals, Physical Chemistry Chemical Physics, 12 (2010) 12544-12555.

[100] S. Zuluaga, S. Stolbov, First principles study of oxygen adsorption on Se-modified Ru nanoparticles, Journal of Physics: Condensed Matter, 24 (2012) 345303.

[101] A. Lewera, J. Inukai, W.P. Zhou, D. Cao, H.T. Duong, N. Alonso-Vante, A. Wieckowski, Chalcogenide oxygen reduction reaction catalysis: X-ray photoelectron spectroscopy with Ru, Ru/Se and Ru/S samples emersed from aqueous media, Electrochimica Acta, 52 (2007) 5759-5765.

[102] E. Ticanelli, J.G. Beery, M.T. Paffett, S. Gottesfeld, An electrochemical, ellipsometric, and surface science investigation of the PtRu bulk alloy surface, Journal of Electroanalytical Chemistry and Interfacial Electrochemistry, 258 (1989) 61-77.

[103] F.C. Nart, T. Iwasita, On the adsorption of H2PO−4 and H3PO4 on platinum: an in situ FT-ir study, Electrochimica Acta, 37 (1992) 385-391.

[104] M. Weber, F.C. Nart, I.R. de Moraes, T. Iwasita, Adsorption of Phosphate Species on Pt(111) and Pt(100) As Studied by in Situ FTIR Spectroscopy, The Journal of Physical Chemistry, 100 (1996) 19933-19938.

[105] N.A. Anastasijević, Z.M. Dimitrijević, R.R. Adžić, Oxygen reduction on a ruthenium electrode in acid electrolytes, Electrochimica Acta, 31 (1986) 1125-1130.

[106] M.S. Zei, G. Ertl, Structural changes of a Ru(0001) surface under the influence of electrochemical reactions, Physical Chemistry Chemical Physics, 2 (2000) 3855-3859.

Chapter 4

Conclusion

HOR/ORR activities of surface modified electrocatalysts have been investigated. The surface modifications significantly changed electrochemical properties of catalysts including hydrogen and oxygen adsorption energy.

Pt-sub-monolayer-shell@Pd-core nanoparticles showed a 3.5-fold increase in i_0 with a Pt surface concentration of 4.7%. The $\Delta H^{0\#}$ of HOR suggested that Pt shell growth changed the RDS of HOR at a Pt surface concentration of 1.7%. In Pt_x@Pd/C ($x < 1.7$ %), hydrogen desorption was the RDS. The decrease in $\Delta H^{0\#}$ was attributed to an increase in hydrogen desorption rate due to the faster desorption rate on the Pt shell than that on the Pd surfaces. In $Pt_{1.7\%}$Pd/C ~ $Pt_{5.7\%}$Pd/C, the RDS was expected to be associative adsorption of hydrogen. The ensemble effect and decrease in hydrogen adsorption strength seemed to hinder a further decrease in $\Delta H^{0\#}$.

We investigated the changes in ORR activity during CO induced surface Pt segregation in PtAu nanoparticles. Improved ORR activity on CO treated PtAu nanoparticles originated from enhancement of specific activity (1.12 mA cm_{Pt}^{-2} → 1.74 mA cm_{Pt}^{-2}) as well as increase of ECA_{Pt} (33.0 $cm^2 g_{Pt}^{-1}$ → 38.2 $cm^2 g_{Pt}^{-1}$). The Pt surface enrichment in PtAu-CO, which was determined through the XPS and electrochemical measurements, provided more active sites, ECA_{Pt}, for ORR, while

the Ar treatment led to a 5% decrease in ECA_{Pt} when compared to PtAu-AP. The enhancement of specific activity on the Pt rich surface (PtAu-CO) was attributed to weaker adsorption energy of OH, which was confirmed by the positive shift of the PZTC (12 mV) in the CO treated catalyst

The ORR activity of an unmodified Ru/C catalyst decreased by 26.8% with phosphoric acid addition, while surface coverage on Ru was estimated at 21% using CV. In contrast, with phosphoric acid addition, the Se-modified Ru catalysts ($RuSe_y$/C) had enhanced ORR activity at 17.8% ($RuSe_{0.31}$/C), 43.4% ($RuSe_{0.76}$/C), and 63.8% ($RuSe_{1.56}$/C). From the CV and XAS analyses, electrochemical adsorption on Ru atoms was insignificant, but the oxidation state of Ru atoms decreased. Based on the negative shift of the Se K XANES spectra and the increased Se-O interaction demonstrated by Se K EXAFS, the HPA or PA^- likely interacted primarily with the Se atoms, and as a result, the oxygen binding energy decreased (higher ORR kinetics) from the larger electrostatic repulsion.

.

Abstract in Korean

전기화학 반응은 촉매 표면의 구조에 많은 영향을 받기 때문에, 높은 효율과 낮은 가격을 가지는 연료전지용 전기화학 촉매를 개발하기 위해 표면이 개질된 나노입자의 연구가 활발히 진행되어 왔다. 표면이 개질된 촉매를 얻기 위해 많은 시도들이 있어왔다.

다양한 표면 개질을 통해 얻어진 나노입자 촉매의 수소산화반응과 산소환원반응에 대한 활성에 대한 표면 개질의 영향을 연구하고, 표면 개질의 결과 나타나게 되는 촉매 표면의 이종원소의 영향에 대해 논의 하였다. 촉매의 표면 개질은, 1) 팔라듐 나노입자의 표면을 한 층 이하의 백금으로 개질 하는 방법, 2) 백금-금 합금 촉매를 일산화탄소 또는 아르곤 분위기에서 열처리 하여 합금 촉매 표면의 백금 농도를 조절하는 방법, 3) 셀레늄으로 개질된 루테늄 촉매의 표면에 인산을 선택적으로 흡착시키는 방법의 세가지 방법이 시도되었다.

백금으로 개질된 팔라듐 촉매의 수소산화반응에 대한 활성을 백금의 표면 농도가 0~5.7% 인 범위에서 연구하였다. 전기화학적 분석과 광전자 분광법을 이용한 분석을 통해 백금으로 개질된 팔라듐 입자표면의 산화

된 팔라듐의 양이 감소(-23.4%) 하는 것을 확인하였고, 엑스선흡광분광법을 이용하여 백금의 양이 증가할수록 백금의 산화수가 증가 하는 것을 확인하였다. 백금의 표면 농도가 1.7% 이상일 때 팔라듐 입자 표면의 백금 원자에 의해 수소산화반응의 율속단계가 수소이온의 탈착반응에서 수소 분자의 해리흡착반응으로 변화 하는 것을 회전원판전극을 이용해 분석하였다.

일산화탄소 흡착에 의한 백금-금 합금 표면의 백금 농도 증가가 산소환원반응 활성에 미치는 영향을 연구하기 위해, 백금-금 합금 촉매를 일산화탄소와 아르곤 분위기에서 각각 열처리를 진행하였다. 광전자분광법을 통해 일산화탄소 분위기에서 백금 농도가 증가(66 ± 2% → 74 ± 2%)하는 것을 확인하였다. 이로 인해 산소환원반응에 대한 무게당 활성이 75.6% 증가 하였고 이는 백금의 표면적이 15.8% 늘어 난 것과 표면의 백금-금 비율의 변화로 인해 백금의 산소에 대한 결합에너지가 감소한 것에 기인 하는 것으로 분석 되었다.

인산의 흡착에 의한 셀레늄으로 개질된 루테늄 촉매의 산소환원 반응에 대한 영향을 분석하기 위해 탄소에 담지된 루테늄 촉매와 셀레늄으로 개질된 루테늄 촉매를 비교 하였다. 루테늄 촉매의 경우 인산의 흡착에

의해 산소환원에 대한 활성이 26.8% 감소 하였고 이는 주로 활성점의 감소 (21%) 에 기인 하는 것으로 분석 되었다. 셀레늄으로 개질된 루테늄 촉매의 경우 인산의 흡착에 의해 활성이 63.8% 증가 하였고, 이는 인산이 셀레늄에 선택적으로 흡착하여 루테늄의 산소에 대한 결합 에너지를 약화 시킨 것이 주요한 원인이 될 것으로 분석되었다.

주요어: 고분자전해질연료전지, 전기화학촉매, 표면개질, 수소산화반응, 산소환원반응

학번: 2008-30260

CURRICULUM VITAE

Hee-Young Park

Photo & Electrochemical Energy Laboratory,
School of Chemical and Biological Engineering,
Seoul National University, Seoul 151-744, Republic of Korea

Education

Doctor of Philosophy (March 2008 ~ February2013)

School of Chemical and Biological Engineering, Seoul National University

Advisor: Prof. Yung-Eun Sung

Thesis: Effect of surface modification on the structure and electrochemical properties of electrocatalysts for polymer electrolyte membrane fuel cells

Master of Science (March 2006 ~ February 2008)

School of Chemical and Biological Engineering, Seoul National University

Advisor: Prof. Yung-Eun Sung

Thesis: Enhanced electrocatalytic activity of Pd/WC for hydrogen oxidation reaction in PEMFC

Bachelor of Science (March 2001 ~ August 2005)

School of Chemical and Biological Engineering, Seoul National University

Award and Fellowship

1. National Science and Engineering Graduate Research Scholarship (2008-2009)
   Korea Student Aid Foundation

2. Best Poster Award (November, 4, 2010)
   (**H. -Y Park**, Y. -H. Cho, N. Jung, K. -H. Choi, Y. -H. Chung, T. -Y. Jeon, Y. -E. Sung)
   Korean Electrochemical Society

3. Best Poster Award (November, 17, 2011)
   (**H. -Y Park**, S. J. Yoo, T. -Y. Jeon, Y. -E. Sung)
   Korean Synchrotron Radiation Users Association

List of Publications

International Journal - SCI

Published

1. **H. -Y. Park**, T. -Y. Jeon, J. H. Jang, S. J. Yoo, K. -S. Lee, Y. -H. Cho, K. -H Choi, Y. -H. Cho, N. Jung, Y. -H. Chung, and Y. -E. Sung, "Hydrogen oxidation reaction activity of sub-monolayer Pt-shell/Pd-core nanoparticles", *Journal of The Electrochemical Society*, In press.

2. **H. -Y. Park**, S. J. Yoo, S. -Y. Lee, H. C. Ham, Y. -E. Sung, S. -K. Kim, S. J. Hwang, H. -J. Kim, E. Cho, D. Henkensmeier, S. W. Nam, T. -H. Lim, and J. H. Jang, "Effect of Se modification on $RuSe_y$/C electrocatalyst for oxygen

reduction with phosphoric acid", *Electrochemistry Communications*, In press.

3. **H. -Y. Park**, T. -Y. Jeon, J. H. Jang, S. J. Yoo, K. -H Choi, N. Jung, Y. -H. Chung, M. Ahn, Y. -H. Cho, K. -S. Lee, and Y. -E. Sung, "Enhancement of oxygen reduction reaction on PtAu nanoparticles via CO induced surface Pt enrichment", *Applied Catalysis B: Environmental*, In press

4. Tae-Yeol Jeon , Nicola Pinna , Sung Jong Yoo , Docheon Ahn , Sun Hee Choi , Marc-Georg Willinger , Yong-Hun Cho , Kug-Seung Lee , Hee-Young Park , Seung-Ho Yu and Yung-Eun Sung, "Selective deposition of Pt onto supported metal clusters for fuel cell electrocatalysts", *Nanoscale*, 2012, 4, 6461-6469.

5. K. -S. Lee, Y. -H. Cho, T. -Y. Jeon, S. J. Yoo, **H. -Y. Park**, J. H. Jang, and Y. -E. Sung, "Surface Structures and Electrochemical Activities of PtRu Overlayers on Ir Nanoparticles", *ACS Catalysis*, 2012, 2, 739-735.

6. T. -Y. Jeon, S. J. Yoo, **H. -Y. Park**, Sang-Kyung Kim, S. Lim, D. Peck, D. -H. Jung, and Y. -E. Sung, "Electrocatalytic Effects of Carbon Dissolution in Pd Nanoparticles", *Langmuir*, 2012, 28, 3664-3670.

7. Y. -H. Cho, Y. -H. Cho, J. W. Lim, **H. -Y. Park**, N. Jung; M. Ahn, H. Choi, and Y. -E. Sung, "Performance of membrane electrode assemblies using PdPt alloy as anode catalysts in polymer electrolyte membrane fuel cell", *International Journal of Hydrogen Energy*, 2012, 37, 5884-5890

8. K. -S. Lee, **H. -Y. Park**, Y. -H. Cho, I. -S. Park, S. J. Yoo, and Y. -E. Sung, "Modified polyol synthesis of PtRu/C for high metal loading and effect of post-treatment", *Journal of Power Sources*, 2010, 195, 1031-1037.

9. S. J. Yoo, **H. -Y. Park**, T. -Y. Jeon, I. -S. Park, Y. -H. Cho, and Y. -E. Sung,

"Promotional effect of palladium on the hydrogen oxidation reaction at a PtPd alloy electrode", *Angewandte Chemie - International Edition*, 2008, 47, 9307-9310.

10. I -S. Park, K. -S. Lee, D. -S. Jung, **H. -Y. Park**, and Y. -E. Sung, "Electrocatalytic activity of carbon-supported Pt-Au nanoparticles for methanol electro-oxidation", *Electrochimica Acta*, 2007, 52, 5599-5605.

11. I. -S. Park, K. -S. Lee, J. -H. Choi, **H. -Y. Park**, and Y. -E. Sung, "Surface Structure of Pt-Modified Au Nanoparticles and Electrocatalytic Activity in Formic Acid Electro-Oxidation", *Journal of Physical Chemistry C*, 2007, 111, 19126-19133.

12. I. -S. Park, K. -S. Lee, Y. -H. Cho, **H. -Y. Park**, and Y. -E. Sung, "Methanol electro-oxidation on carbon-supported and Pt-modified Au nanoparticles", *Catalysis Today*, 2008, 132, 127-131.

13. K. -S. Lee, I. -S. Park, **H. -Y. Park**, T. -Y. Jeon, and Y. -E. Sung, "PtRu overlayers on Au nanoparticles for methanol electro-oxidation", *Catalysis Today*, 2009, 146, 20-24.

14. K. -S. Lee, I. -S. Park, **H. -Y. Park**, T. -Y. Jeon, Y. -H. Cho, and Y. -E. Sung, "PtRu-Modified Au Nanoparticles as Electrocatalysts for Direct Methanol Fuel Cells", *Journal of The Electrochemical Society*, 2009, 156, B1150-B1155.

15. K. -S. Lee, I. -S. Park, Y. -H. Cho, D. -S. Jung, N. Jung, **H. -Y. Park**, and Y. -E. Sung, "Electrocatalytic activity and stability of Pt supported on Sb-doped SnO_2 nanoparticles for direct alcohol fuel cells", *Journal of Catalysis*, 2008, 258, 143-152.

16. Y. -H. Cho, H. -S. Park, D. -S. Jung, **H. -Y. Park**, and Y. -E. Sung, "Effect

of platinum amount in carbon supported platinum catalyst on performance of polymer electrolyte membrane fuel cell", *Journal of Power Sources*, 2007, 172, 89-93.

Submitted

1. **H. -Y. Park**, I. -S. Park, B. Choi, K. -S. Lee, T. -Y. Jeon, S. J. Yoo, and Y. -E. Sung, **"**Pd Nanocrystals on WC as a Synergistic Electrocatalyst for Hydrogen Oxidation Reactions", *Physical Chemistry Chemical Physics*, Submitted

Domestic non-SCI

1. K. -S. Lee, **H. -Y. Park**, T. -Y. Jeon, and Y. -E. Sung, "Ethanol Electro-Oxidation and Stability of Pt Supported on Sb-Doped Tin Oxide" *Journal of the Korean Electrochemical Society*, 2008, 11(3), 141-146.
2. K. -H Choi, K. -S. Lee, T. -Y. Jeon, **H. -Y. Park**, N. Jung, Y. -H. Chung, and Y. -E. Sung, "High Alloying Degree of Carbon Supported Pt-Ru Alloy Nanoparticles Applying Anhydrous Ethanol as a Solvent", *Journal of Electrochemical Science and Technology*, 2010, 1(1), 19-24.

Patent/disclosures

1. N. H. Kwon, J. S. lee, B. Roh, Y. -E. Sung, T. -Y. Jeon, **H. -Y. Park**, J. W. Lim, Y. -H. Chung "Synthesis methods of Nano-sized Nickel or Palladium on a Carbon support" Patent number (Korea): **10-1144107-00-00** (2012)

Technical Presentations

International Conferences

1. **H. -Y. Park**, S. J. Yoo, S. Y. Lee, K. -S. Lee, Y. -E. Sung, H. -J. Kim, E. Cho, S. -K. Kim, D. Henkensmeier, T. -H. Lim, and J. H. Jang, 3th Carisma International Conference, Copenhagen, Denmark, September 3-5, 2012, "Effect of Se modification of RuSey/C electrocatalyst on the oxygen reduction activities in the presence of phosphoric acid"

2. **H. -Y. Park**, T. -Y. Jeon, S. J. Yoo, and Y. -E. Sung, American Chemical Society, Anaheim, CA, USA, march 27-31, 2011, "Manipulation of surface concentration of Pt in Pt-Au alloy nanoparticles using post treatment".

3. **H. -Y. Park**, K. -S. Lee, T. -Y. Jeon, and Y. -E. Sung, International Fuel Cell Workshop 2009, Kofu, Japan, August 23-24, 2009, "Platinum modified palladium electrocatalyst for polymer electrolyte membrane fuel cell".

4. **H. -Y. Park**, I. -S. Park, K. -S. Lee, T. -Y. Jeon and Y. -E. Sung, 3rd Asian Conference on Electrochemical Power Sources (ACEPS-3), Korea University, Seoul, Korea, November 10-14, 2008, "Palladium electrocatalyst for hydrogen oxidation reaction in polymer electrolyte membrane fuel cells".

5. **H. -Y. Park**, I. -S. Park, K. –S. Lee, and Y. -E. Sung, 9th Scientific and Technical Conference (KOMEKO 2008), Szczyrk, Poland, March 12-14, 2008, "Tungsten carbide supported palladium electrocatalyst for hydrogen oxidation reaction in polymer electrolyte membrane fuel cell".

6. T. -Y. Jeon, K. -S. Lee, Y. -H. Cho, S. J. Yoo, **H. -Y. Park**, and Y. -E. Sung, International Fuel Cell Workshop 2009, Kofu, Japan, August 23-24, 2009, "Surface properties and methanol oxidation reaction of carbon-supported Pt-Ru nanoparticles".

7. K. -S. Lee, I. -S. Park, **H. -Y. Park**, T. -Y. Jeon, and Y. -E. Sung, International Fuel Cell Workshop 2009, Kofu, Japan, August 23-24,

2009, “PtRu overlayers on carbon-supported Au nanoparticles as anode catalysts for direct methanol fuel cells”.

8. T. -Y. Jeon, Y. -H. Cho, K. -S. Lee, **H. -Y. Park** and Y. -E. Sung, 3rd Asian Conference on Electrochemical Power Sources (ACEPS-3), Korea University, Seoul, Korea, November 10-14, 2008, “Electrocatalytic Activity of Carbon-Sputtered Pt-M (M = Ni, Co) Alloy Nanoparticles for Oxygen Reduction in PEMFCs”.

9. S. J. Yoo, **H. -Y. Park**, T. -Y. Jeon, Y. -H. Cho, and Y. -E. Sung, 3rd Asian Conference on Electrochemical Power Sources (ACEPS-3), Korea University, Seoul, Korea, November 10-14, 2008, “Promotional effect of palladium on hydrogen oxidation reaction catalyzed by platinum-palladium alloy electrocatalyst”.

10. K. -S. Lee, T. -Y. Jeon, **H. -Y. Park** and Y. -E. Sung, 3rd Asian Conference on Electrochemical Power Sources (ACEPS-3), Korea Universty, Seoul, Korea, November 10-14, 2008, “Control of alloying degree in PtRu/C catalyst for direct methanol fuel cells”.

11. K. -S. Lee, T. -Y. Jeon, **H. -Y. Park**, and Y. -E. Sung, 3rd Asian Conference on Electrochemical Power Sources (ACEPS-3), Korea University, Seoul, Korea, November 10-14, 2008, “Improvement in electrochemical stability of Pt and PtRu nanoparticles”.

12. T. -Y. Jeon, K. -S. Lee, Y. -H. Cho, **H. -Y. Park**, I. -S. Park, Y. -E. Sung, 213th ECS Meeting (The Electrochemical Society), Phoenix, AZ, May 18-22, 2008, “ Electrocatalytic Activity of Carbon-Supported Pt-Ni Alloy Nanoparticles for Oxygen Reduction in PEMFCs”.

13. S. J. Yoo, Y. -H. Cho, B. Choi, **H. -Y. Park**, and Y. -E. Sung, Polymer Batteries-Fuel Cells, Roma, Italy, June 11-14 2007, “Enhanced electrocatalytic activity of hydrogen oxidation reaction on bimetallic PtPd electrode”.